Germanium Tin for Use in Semimetal Electronics

Conor O'Donnell

NATIONAL UNIVERSITY OF IRELAND, CORK

Tyndall National Institute

Thesis submitted for the degree of Doctor of Philosophy

May 2021

Head of School/Department : Dr Fatima Gunning

Supervisors: Prof. James C. Greer
Dr Lida Ansari

Research supported by Science Foundation Ireland

Contents

List of Figures

List of Tables

This is to certify that the work I am submitting is my own and has not been submitted for another degree, either at University College Cork or elsewhere. All external references and sources are clearly acknowledged and identified within the contents. I have read and understood the regulations of University College Cork concerning plagiarism and intellectual property.

Conor O'Donnell

For my family

Conferences and Publications

0.1 Conferences

- **Poster - Alloying Sn and Ge to Engineer a Material for use in a Semimetal Nanowire Transistor** Tyndall Student Poster competition 26/08/2015
- **Poster - Bandgap Tuning in SnGe Alloys** Intel Ireland Research Conference 20/10/2015
- **Poster - Bandgap Tuning of SnGe Alloys for Nanoelectronics Applications** Intel Ireland Research Conference 12/10/2016
- **Poster - Bandgap Tuning in Tin Germanium Alloy Thin Films and Nanowires** Tyndall Student Poster competition 29/07/2016
- **Talk - Improving Miscibility in GeSn Alloys** EMRS Spring Meeting 22/05/2017

0.2 Publications

- **A. Sanchez-Soares, C. O'Donnell, and J.C. Greer** Electronic structure tuning via surface modification in semimetallic nanowires

  Physical Review B **94**, 235442 (2016)
- **C. O'Donnell A. Sanchez-Soares, C. A. Broderick and J.C. Greer** Impact of stoichiometry and strain on $Ge_{1-x}Sn_x$ alloys from first principles

  Journal of Physics D: Applied Physics **54**, 245103 (2021)
- **A. Sanchez-Soares, C. O'Donnell, and J. C. Greer** Epitaxial Stabilisation of $Ge_{1-x}Sn_x$ Alloys

  Accepted - Journal of Physics D: Applied Physics
- **A. Sanchez-Soares , C. König, C. O'Donnell, J.-P. Colinge, and J. C. Greer** Book Chapter: Semimetal electronics: Quantum confinement and surface chemistry as design tools

  21st Century Nanoscience

Abstract

As electronic devices shrink to sub 5 nm dimensions, issues such as dopant variability as well as quantum confinement begin to hamper traditional metal oxide silicon field effect transistor (MOSFET) designs. A proposed alternative design, the confinement modulated gap transistor (CMGT), employs semimetals to overcome these hurdles. By taking advantage of the quantum confinement effect inducing a band gap in confined semimetals, a thick-thin-thick configuration can be used to create a set of monomaterial back-to-back Schottky barriers, which can then be gated. $Ge_{1-x}Sn_x$, a material which has garnered much interest in the photonics community for its indirect to direct band gap transition with rising Sn content, has been shown to become semimetallic as Sn content is further increased. The aim of this thesis is the investigation of $Ge_{1-x}Sn_x$ alloys in terms of their miscibility as well as their electronic structure, to assess which compositions and strains would be of use in the fabrication of semimetal-based devices. We employ LDA DFT to calculate the alloy structural properties and meta-GGA to calculate band structures.

First the miscibility and structural properties of the alloy are studied. The evolution of the equilibrium lattice constant, the elastic constants, and the bond lengths are predicted across the full alloy composition range. Through use of the cluster expansion formalism and Monte Carlo simulations, an equilibrium phase diagram of the solid phase is generated. The formation energies of these alloys are also investigated and decomposed into their constituent components, and this is then repeated for biaxially strained bulk cells, which are allowed to relax perpendicular to the strain direction. We consider three virtual substrates: Ge, ZnTe and CdTe. The critical thicknesses of these alloys are also predicted using an elastic continuum model.

The electronic structure of the relaxed alloys is investigated, and the evolution of the band gap found to agree well with previous experimental results. This is then repeated for the same biaxially strained cells previously discussed, to understand how strain affects the band gap, and the semiconducting to semimetallic transition which occurs as Sn is added. The semiconducting to semimetallic transition is then plotted for increasing tensile strain, as well as the critical thickness at the required strain and composition. Deformation potential theory is employed to understand the behaviour of the band gap as strain is added. This is then used to generate a model which predicts the band gap over the composition range for

a large tensile strain range.

Chapter 1

Introduction

Integrated circuits (ICs) are the cornerstone of modern electronic engineering. They have penetrated virtually every industry, as well as increased the quality of life. They can be found in devices, including massive industrial machines, medical modules like pacemakers, communications devices such as smart phones, and in computing from laptops to cloud resources. Analogue ICs are also used for reading and processing signals from sensors, and for communication applications. Digital ICs perform mathematical operations through use of Boolean logic gates, which are implemented using transistors, such as the field effect transistor (FET). FETs are three terminal devices which consist of a source, a drain, and a channel with a gate. The gate modulates the flow of current through the channel (L) from the source to drain. Figure 1.1 depicts a cross section of a metal oxide silicon field effect transistor (MOSFET).

Reducing the size of transistors leads to many benefits. Smaller transistors are desirable as they draw less power, and as channel length is smaller, the gate has more control in finFET and gate-all-around (GAA) architectures and less voltage is needed to switch the device [2]. Smaller transistor sizes also allow for incorporation of more transistors onto a single die, leading to increases in processing power for electronic devices such as laptop and desktop computers.

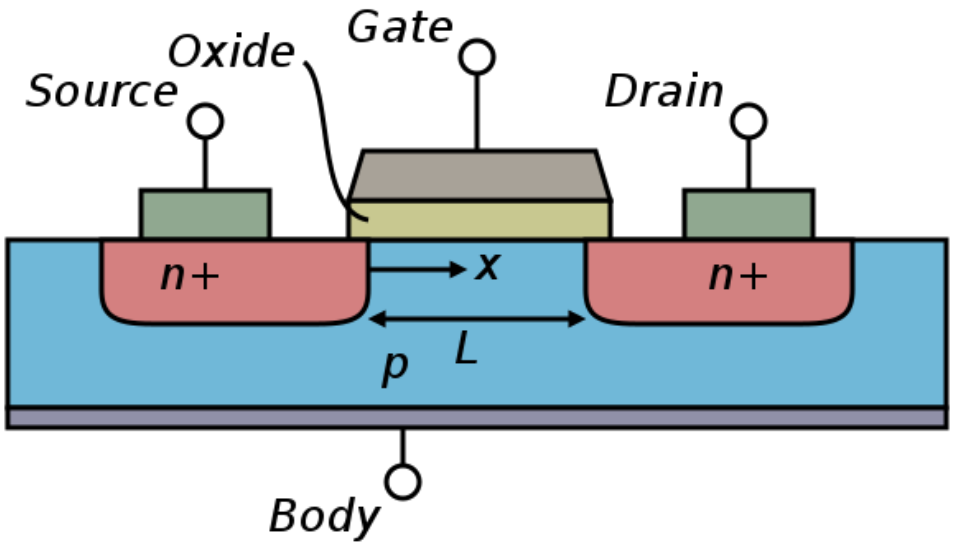

Figure 1.1: Cross section of an n-type MOSFET. Reproduced from [1].

However, issues with doping, as well as quantum confinement, have been shown to cause issues in traditional device designs as they reach sub 5 nm dimensions. As these devices are scaled down, only tens of dopant atoms, and possibly fewer, can influence transistor properties [2]. Keeping the number of dopants consistent between devices becomes extremely challenging, leading to undesired variability in device characteristics. As critical dimensions are further reduced, junctions between n-type and p-type regions present a problem. Typical transistor designs make use of n-type and p-type doped regions and the junctions formed between them. However, at these small length scales, dopant diffusion between different regions becomes a key issue in the fabrication of these devices, reducing the abruptness of a junction [2].

Another issue with shrinking transistors is that of quantum confinement. Typically, at sub 10 nm dimensions, band gaps of semiconductors increase due to quantum confinement. The quantum confinement effect is the increase in the band gap of a material as the cross-sectional dimensions become comparable to the de Broglie wavelength of an electron [3]. The change in energy (ΔE_n) of a

band due to confinement can be estimated from:

$$\Delta E_n = \frac{\hbar^2 k^2}{2m^*}\,, \tag{1.1}$$

where $\hbar$ is the reduced Plank's constant, and m^* is the effective mass of the band from the parabolic band approximation, and k, the wave number, is given as:

$$k = \frac{\pi n}{l}\,. \tag{1.2}$$

where l is the thickness of the confining direction and $n = 1, 2, 3...$ [2]. As l is reduced, the valence band decreases in energy and the conduction band increases in energy, leading to a wider band gap.

As well as widening band gaps in semiconductors, quantum confinement has been shown to open up band gaps in semimetals. Semimetals are materials with a low or vanishing density of states at the Fermi level. Semimetals fall into two classes, those with a "zero" band gap and those with a "negative" band gap. A "zero" band gap semimetal has a conduction and a valence band which touch but do not cross, whereas a "negative" band gap semimetal's conduction band is lower in energy than its valence band at a given point in k space, but the two do not overlap. These two cases are both represented in fig. 1.2. Examples of elemental semimetals include bismuth (Bi), α-tin (α-Sn), arsenic, antimony, and graphene. Semimetallic properties can also be brought about via alloying, for example in Bi_2Te_3–Sb, BiSb, and $Ge_{1-x}Sn_x$. The semimetallic nature of the $Ge_{1-x}Sn_x$ alloy above the transition composition allows for potential applications in electronic devices, as will be discussed later in this chapter.

Band gaps brought about by the quantum confinement effect in semimetals have been previously demonstrated in simulations of bismuth [4] and α-Sn [5] nanowires. This has also been demonstrated experimentally for bismuth [6].

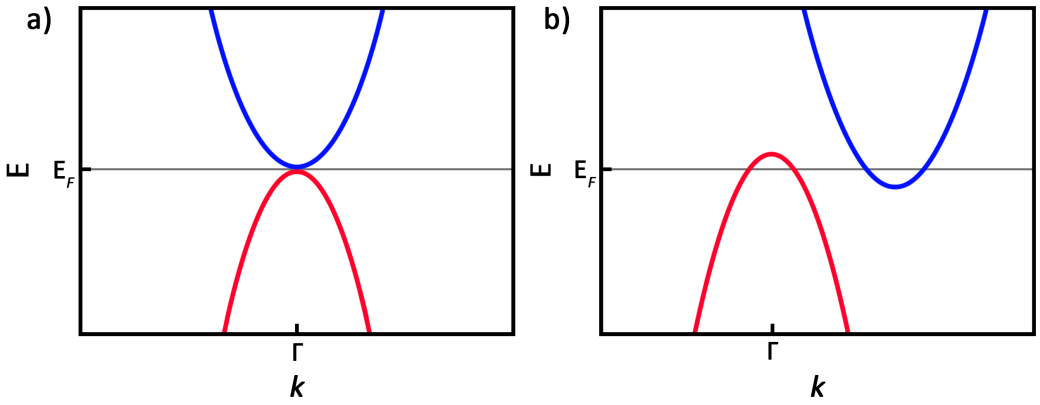

Figure 1.2: Representation of a semimetallic band structure where (a) the conduction and valence bands meet but do not cross, and (b) where the conduction band is lower than the valence band but does not cross it.

Ansari et al. [5] have theoretically demonstrated the increase of the band gap of α-Sn as nanowire diameter decreases. This study also demonstrates the variation in band gap with nanowire orientation. At such small diameters surface area is increased, meaning the impact of the different surface chemistries associated with each orientation plays a heightened role in the determination of the band gap [7–9].

The change from semimetallic to semiconducting electronic structures as a function of thickness opens up new avenues for device design. In 2008 Li et al. [10] proposed using nano-patterned graphene nanoribbons as the channel material in a FET. By confining the graphene nanoribbons, a band gap is formed as a result of quantum confinement, removing the need for doping. This also uses quantum confinement as an aspect of the design, instead of it interfering by widening the band gap of a bulk semiconductor. A dopant free monomaterial device proposed by Ansari et al. [5], the confinement modulated gap transistor (CMGT), makes similar use of quantum confinement. This is done by inducing Schottky barriers between thin and thick portions of a semimetallic wire comprised of α-Sn. A Schottky barrier is the potential barrier created at a metal-semiconductor inter-

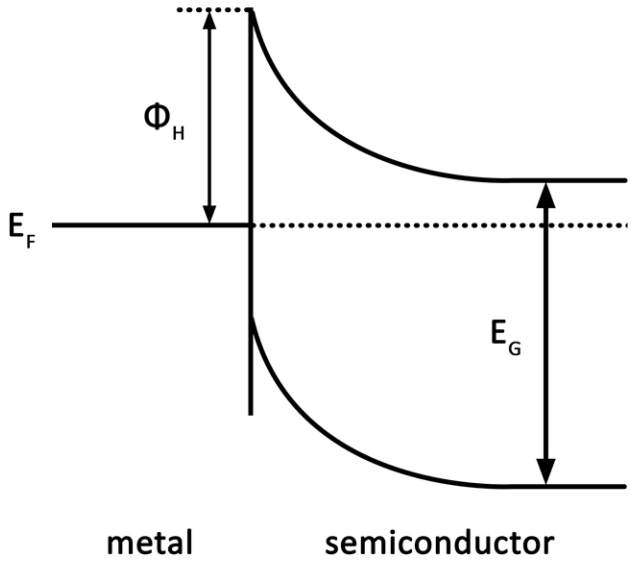

Figure 1.3: Band profile of a Schottky barrier, where Φ_{H} is given as the barrier height, E_{G} is the energy gap in the semiconductor, and E_{F} is the Fermi level.

face leading to diode (or rectifying) behaviour. This is depicted in fig. 1.3. By patterning the Sn nanowire, a thick-thin-thick structure can be arranged which leads to a semimetal-semiconductor-semimetal band profile with the thin section having a quantum confinement induced semiconducting behaviour, as shown in fig. 1.4.

This band alignment, between the thick and thin regions creates a pair of back-to-back Schottky barriers. When gated, as in the CMGT, this acts as a Schottky barrier transistor [11], with the gate allowing current to flow in the ON state through capacitive coupling between gate and the channel. An atomic illustration of such a device is depicted in fig. 1.5.

The concept for a CMGT nanowire transistor was demonstrated using density functional theory (DFT) [12] in conjunction with a non equilibrium Green's

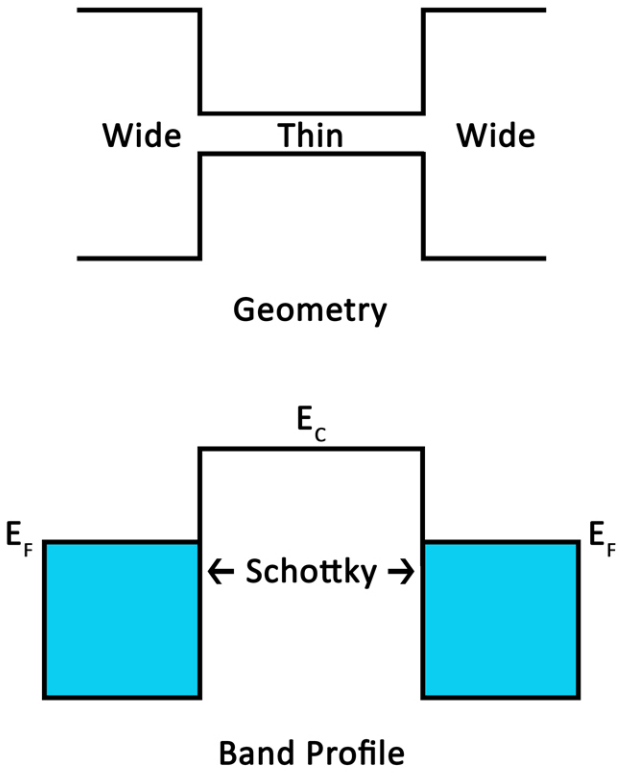

Figure 1.4: Diagram of how a thick-thin-thick configuration of nanowires can produce a Schottky barrier transistor.

function (NEGF) charge transport scheme [13]. Transistor-like behaviour was demonstrated, with emphasis on the subthreshold slope, a measure of how easy it is to switch the device between its ON and OFF states. The theoretical ideal subthreshold slope is approximately 60mV/dec at room temperature [14], and for an average state-of-the-art MOSFET it is approximately 70 mV/dec. The α-Sn CMGT is predicted to exhibit a subthreshold slope of ≈73 mV/dec at a thickness of 3 nm in a GAA architecture.

An alternative method has also been shown to induce the desired band profile in semimetals. At a crystal surface, there are dangling bonds which must be terminated. By abruptly changing the terminating atomic species along the length of the wire, segments of wire with varying bandgaps can be created [8, 15]. When suitable terminations are chosen, this can also lead to a semimetal-semiconductor

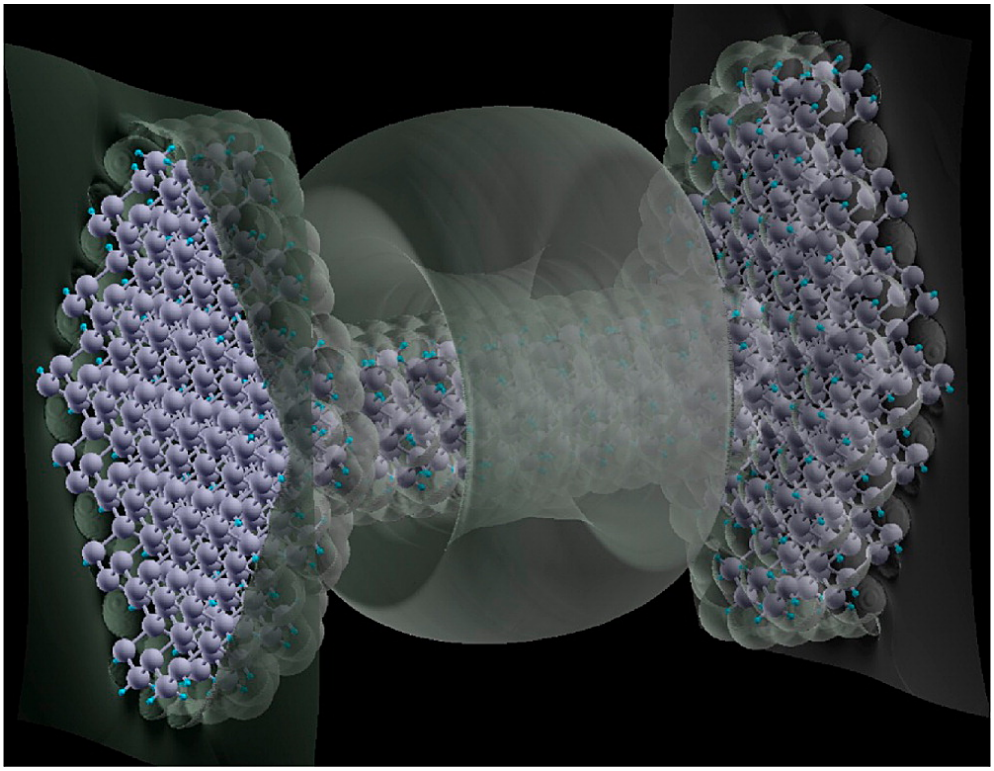

Figure 1.5: Atomic illustration of an α-Sn CMGT. Reprinted (adapted) with permission from Ref. [5]. Copyright 2021 American Chemical Society.

interface and the formation of Schottky barriers. This is depicted in fig. 1.6.

This concept has also been simulated in DFT and has been shown to allow for the creation of a semimetal based rectifier, where it was reported that fluorine terminated <110> oriented Sn nanowires with a diameter of 1.5 nm were predicted to be approximately semimetallic, with a band gap of 30 meV. The hydrogen terminated wires of the same size and orientation were demonstrated to have a 680 meV bandgap [16]. The simulated diode was shown to have a low reverse current, with the diode exhibiting high current for positive voltages above 0.6 V. A representation of such a device is depicted in fig. 1.7(a), with fig. 1.7(b) showing the local density of states (LDOS) of the device.

Small amounts of Sn have previously been used as stressors in germanium (Ge) to add compressive strain to regions of electronic devices [17, 18]. In recent years $Ge_{1-x}Sn_x$ alloys have also garnered much interest in the photonics community as

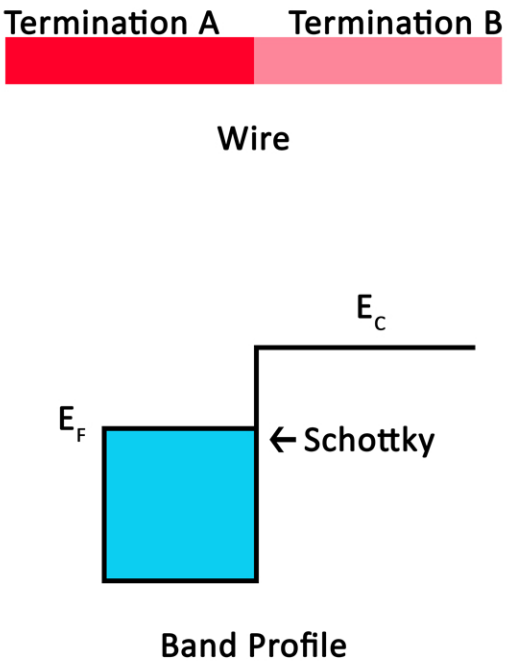

Figure 1.6: Band profile of a Schottky barrier induced by an abrupt change in surface termination along the length of a semimetallic nanowire, where E_C is the energy of the conduction band in the semiconductor and E_F is the Fermi level.

a silicon compatible group-IV direct band gap material allowing for the creation of a silicon compatible laser [19–26]. Experiments have demonstrated lasing at temperatures up to 273 K [27]. This is made possible due to the indirect to direct electronic band gap transition that is shown to occur in both theoretical and experimental measurements between alloy compositions in the range of $0.065 \lesssim x \lesssim 0.11$ [28–32]. As Sn is added to Ge, the Γ_7^- state of Ge, depicted in fig. 1.8(a), lowers in energy at a higher rate than the L^+ state. As the Sn content increases to between $0.2 \lesssim x \lesssim 0.4$, it has also been predicted that a semiconducting to semimetallic transition occurs, with the material remaining semimetallic as the composition increases up to x=1 [28, 33, 34].

$Ge_{1-x}Sn_x$ promises significant advantages over α-Sn based semimetal device de-

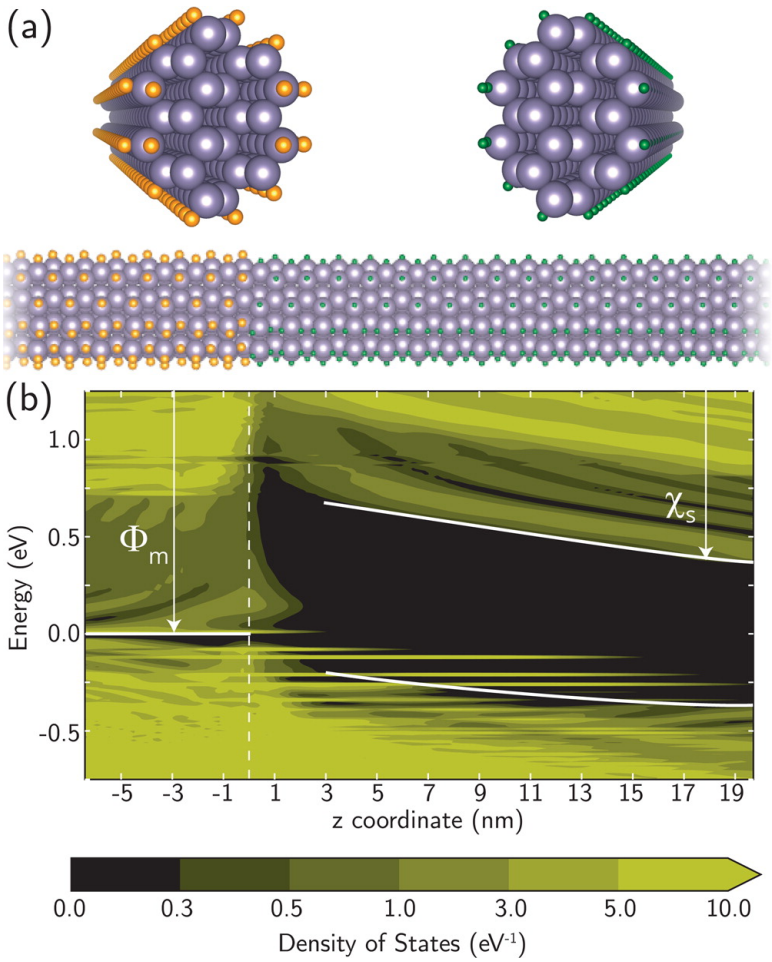

Figure 1.7: (a) Visualization of the junction between the fluorine and hydrogen terminated segments of the α-Sn nanowire (b) Contour plot of the predicted LDOS of the diode. Reprinted (adapted) with permission from Ref. [16]. Copyright 2021 American Chemical Society.

signs. The alloy nature of the material allows for an extra parameter, composition, to be selected in order to achieve suitable band gaps at varying thicknesses. However, $Ge_{1-x}Sn_x$ has been shown to have its own issues which need to be understood and overcome. The elemental constituents of $Ge_{1-x}Sn_x$ exhibit a large difference in ionic radii (≈15%), which results in a low solid solubility of Sn in Ge (≈ 1%) [38]. However, non equilibrium growth techniques, such as molecular beam epitaxy (MBE) and chemical vapour deposition (CVD), have been employed to overcome this limit and allow growth of alloy films epitaxially [39–45]. Lattice matching in particular has shown great promise in increasing the Sn composition of alloys. Utilizing MBE, realization of thin films with thicknesses

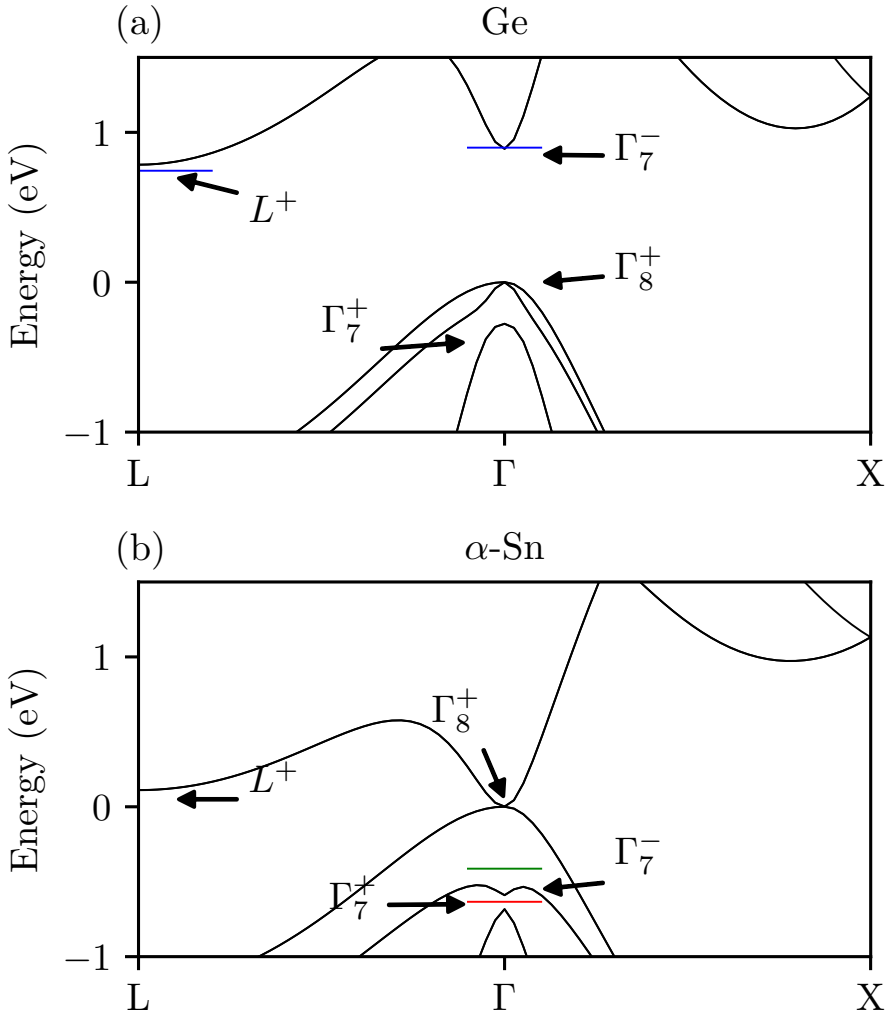

Figure 1.8: Band structure of (a) Ge and (b) α-Sn. Experimental results are indicated with blue [35], green [36] and red [37] bars.

up to 300 nm, compositions up to x=0.5, and lattice matched to GaSb has been achieved [39]. However, it is acknowledged in Ref. [39] that under "practical MBE growth conditions" it would be difficult to reach even 100 nm due to the impact of compositional fluctuations on the critical thickness. The choice of substrate is known to be important, as a Ge substrate severely limits the thickness as well as the achievable alloy composition, allowing growth up to a thickness of just 3 nm for a film with an alloy composition of x=0.46. At this thickness, strain energy prohibits continued growth [46]. A central aim of this thesis is to theoretically investigate the most appropriate conditions, in terms of strain and composition,

to produce $Ge_{1-x}Sn_x$ alloys which are suitable for use in the creation of semimetal based devices.

To date, $Ge_{1-x}Sn_x$ has primarily been investigated in the low composition ranges at which the indirect-to-direct band gap transition occurs, in order to take advantage of its lasing properties. The focus of this thesis is to provide insight and motivation to explore $Ge_{1-x}Sn_x$ alloys across a broad range of compositions and substrates. This will be done through the application of first principles calculations, using DFT in order to gain an understanding of the alloy's electronic structures at various compositions and strains. As well as this, miscibility models, such as the Bragg-Williams model and the cluster expansion formalism, will be introduced and employed to assess the miscibility of $Ge_{1-x}Sn_x$ alloys, with analysis of the formation energies as calculated within DFT. Through a combination of analysing the band gaps and miscibility as a function of strain, the ideal strains and compositions for creating bulk semimetallic $Ge_{1-x}Sn_x$ will be predicted. The identification of these material parameters provides the details necessary for growth of thick semimetallic structures and thin semiconducting structures, such as films or wires, for use in semimetallic device designs.

The remainder of this thesis is laid out as follows:

Chapter 2 contains an overview of the theoretical methods employed in the simulations in later chapters. Density functional theory, the *ab initio* method which forms the basis of many of the calculations in this work, is described as well as the theory behind the miscibility and band gap models that are employed. The details of the calculations themselves are contained in the chapters describing the results.

Chapter 3 discusses elemental Ge and α-Sn. This chapter serves to analyse the material properties of the two alloy constituents, as well as provide a benchmark for later alloy band gap calculations.

Chapter 4 focuses on the miscibility and stability of the $Ge_{1-x}Sn_x$ alloy. Epitaxial strain is considered as a means of boosting miscibility, and this is investigated and compared with the decreased critical thickness which is caused by strain. This is done through calculations on different substrates inducing epitaxial strain on the alloy which are then compared to relaxed structures.

Chapter 5 contains calculations of the electronic structure of $Ge_{1-x}Sn_x$ alloys over the full composition range, $0 \leqslant x \leqslant 1$. The indirect/direct nature of the band gap is discussed, as well as how epitaxial strain affects the band gap in order to ascertain which compositions and strains allow for suitable thicknesses to be reached so that both thin, semiconducting and thicker, semimetallic regions can be fabricated together.

Chapter 6 provides a conclusion to the thesis as well as an outlook to future avenues of research which may be undertaken on the subject.

References

[1] "https://commons.wikimedia.org/wiki/File:Lateral_mosfet.svg accessed 30/06/20."

[2] J. P. Colinge and J. C. Greer, *Nanowire Transistors: Physics of Devices and Materials in One Dimension*. Cambridge: Cambridge University Press, 2016.

[3] N. S. Mohammad. Understanding quantum confinement in nanowires: basics, applications and possible laws. *Journal of Physics: Condensed Matter*, vol. 26, no. 42, p. 423202, 2014.

[4] X. Sun, Z. Zhang, and M. S. Dresselhaus. Theoretical modeling of thermoelectricity in Bi nanowires. *Applied Physics Letters*, vol. 74, no. 26, p. 4005, 1999.

[5] L. Ansari, G. Fagas, J.-P. Colinge, and J. C. Greer. A proposed confinement modulated gap nanowire transistor based on a metal (tin). *Nano Letters*, vol. 12, no. 5, p. 2222, 2012.

[6] F. Gity, L. Ansari, C. König, G. A. Verni, J. D. Holmes, B. Long, M. Lanius, P. Schüffelgen, G. Mussler, D. Grützmacher, and J. Greer. Metal-semimetal Schottky diode relying on quantum confinement. *Microelectronic Engineering*, vol. 195, p. 21, 2018.

[7] M. Nolan, S. O'Callaghan, G. Fagas, J. C. Greer, and T. Frauenheim. Silicon nanowire band gap modification. *Nano Letters*, vol. 7, no. 1, p. 34, 2007.

[8] A. Sanchez-Soares, C. O'Donnell, and J. C. Greer. Electronic structure tuning via surface modification in semimetallic nanowires. *Physical Review B*, vol. 94, no. 23, p. 235442, 2016.

[9] A. Svizhenko, P. W. Leu, and K. Cho. Effect of growth orientation and surface roughness on electron transport in silicon nanowires. *Physical Review B*, vol. 75, no. 12, 2007.

[10] X. Li, X. Wang, L. Zhang, S. Lee, and H. Dai. Chemically derived, ultrasmooth graphene nanoribbon semiconductors. *Science*, vol. 319, no. 5867, p. 1229, 2008.

[11] J. Tucker, C. Wang, and P. S. Carney. Silicon field-effect transistor based on quantum tunneling. *Applied Physics Letters*, vol. 65, no. 5, p. 618, 1994.

[12] R. G. Parr. Density functional theory. *Annual Review of Physical Chemistry*, vol. 34, no. 1, p. 631, 1983.

[13] M. Brandbyge, J.-L. Mozos, P. Ordejón, J. Taylor, and K. Stokbro. Density-functional method for nonequilibrium electron transport. *Physical Review B*, vol. 65, p. 165401, 2002.

[14] K. P. Cheung, On the 60 mv/dec @300 K limit for MOSFET subthreshold swing. in *Proceedings of 2010 International Symposium on VLSI Technology, System and Application*, p. 72, 2010.

[15] A. Sanchez-Soares and J. C. Greer. *Semi-metal rectifying juncton*, WO2017046023A1. US Patent 10 892 32, 2017.

[16] A. Sanchez-Soares and J. C. Greer. A semimetal nanowire rectifier: Balancing quantum confinement and surface electronegativity. *Nano Letters*,

vol. 16, no. 12, p. 7639, 2016.

[17] G. H. Wang, E.-H. Toh, X. Wang, D. H. L. Seng, S. Tripathy, T. Osipowicz, T. K. Chan, K. M. Hoe, S. Balakumar, C. H. Tung, G.-Q. Lo, G. Samudra, and Y.-C. Yeo, Silicon-germanium-tin (SiGeSn) source and drain stressors formed by Sn implant and laser annealing for strained silicon-germanium channel p-MOSFETs. in *2007 IEEE International Electron Devices Meeting*, IEEE, 2007.

[18] G. H. Wang, E.-H. Toh, T. K. Chan, T. Osipowicz, Y.-L. Foo, C. H. Tung, G.-Q. Lo, G. Samudra, and Y.-C. Yeo, Realization of silicon-germanium-tin (SiGeSn) source/drain stressors by Sn implant and solid phase epitaxy for strain engineering in SiGe channel p-MOSFETs. in *2008 International Symposium on VLSI Technology, Systems and Applications (VLSI-TSA)*, IEEE, 2008.

[19] S. Wirths, R. Geiger, N. von den Driesch, G. Mussler, T. Stoica, S. Mantl, Z. Ikonic, M. Luysberg, S. Chiussi, J. M. Hartmann, H. Sigg, J. Faist, D. Buca, and D. Grutzmacher. Lasing in direct-bandgap GeSn alloy grown on Si. *Nature Photonics*, vol. 9, no. 2, p. 88, 2015.

[20] E. Kasper, M. Kittler, M. Oehme, and T. Arguirov. Germanium tin: silicon photonics toward the mid-infrared. *Photonics Research*, vol. 1, no. 2, p. 69, 2013.

[21] N. Von den Driesch, D. Stange, S. Wirths, *et al.* Direct bandgap group IV epitaxy on Si for laser applications. *Chemistry of Materials*, vol. 27, no. 13, p. 4693, 2015.

[22] K. P. Homewood and M. A. Lourenço. The rise of the GeSn laser. *Nature Photonics*, vol. 9, no. 2, p. 78, 2015.

[23] S. Al-Kabi, S. A. Ghetmiri, J. Margetis, T. Pham, Y. Zhou, W. Dou, B. Col-

lier, R. Quinde, W. Du, A. Mosleh, *et al.* An optically pumped 2.5 μm GeSn laser on Si operating at 110 K. *Applied Physics Letters*, vol. 109, no. 17, p. 171105, 2016.

[24] V. Reboud, A. Gassenq, N. Pauc, J. Aubin, L. Milord, Q. Thai, M. Bertrand, K. Guilloy, D. Rouchon, J. Rothman, *et al.* Optically pumped GeSn microdisks with 16% Sn lasing at 3.1 μm up to 180 K. *Applied Physics Letters*, vol. 111, no. 9, p. 092101, 2017.

[25] D. Rainko, Z. Ikonic, A. Elbaz, N. von den Driesch, D. Stange, E. Herth, P. Boucaud, M. E. Kurdi, D. Grützmacher, and D. Buca. Impact of tensile strain on low Sn content GeSn lasing. *Scientific Reports*, vol. 9, no. 1, p. 259, 2019.

[26] A. Elbaz, D. Buca, N. von den Driesch, K. Pantzas, G. Patriarche, N. Zerounian, E. Herth, X. Checoury, S. Sauvage, I. Sagnes, A. Foti, R. Ossikovski, J.-M. Hartmann, F. Boeuf, Z. Ikonic, P. Boucaud, D. Grützmacher, and M. E. Kurdi. Ultra-low-threshold continuous-wave and pulsed lasing in tensile-strained GeSn alloys. *Nature Photonics*, vol. 14, no. 6, p. 375, 2020.

[27] J. Chrétien, N. Pauc, F. A. Pilon, M. Bertrand, Q.-M. Thai, L. Casiez, N. Bernier, H. Dansas, P. Gergaud, E. Delamadeleine, R. Khazaka, H. Sigg, J. Faist, A. Chelnokov, V. Reboud, J.-M. Hartmann, and V. Calvo. GeSn lasers covering a wide wavelength range thanks to uniaxial tensile strain. *ACS Photonics*, vol. 6, no. 10, p. 2462, 2019.

[28] M. P. Polak, P. Scharoch, and R. Kudrawiec. The electronic band structure of $Ge_{1-x}Sn_x$ in the full composition range: indirect, direct, and inverted gaps regimes, band offsets, and the Burstein–Moss effect. *Journal of Physics D: Applied Physics*, vol. 50, no. 19, p. 195103, 2017.

[29] S. Gupta, B. Magyari-Köpe, Y. Nishi, and K. C. Saraswat. Achieving direct

band gap in germanium through integration of Sn alloying and external strain. *Journal of Applied Physics*, vol. 113, no. 7, p. 073707, 2013.

[30] H. P. L. de Guevara, A. G. Rodrıǵuez, H. Navarro-Contreras, and M. A. Vidal. Determination of the optical energy gap of $Ge_{1-x}Sn_x$ alloys with 0<x<0.14. *Applied Physics Letters*, vol. 84, no. 22, p. 4532, 2004.

[31] J. Kouvetakis, J. Menendez, and A. Chizmeshya. Tin-based group IV semiconductors: New platforms for opto- and microelectronics on silicon. *Annual Review of Materials Research*, vol. 36, no. 1, p. 497, 2006.

[32] G. He and H. A. Atwater. Interband transitions in Sn_xGe_{1-x} alloys. *Physical Review Letters*, vol. 79, p. 1937, 1997.

[33] P. Moontragoon, Z. Ikonić, and P. Harrison. Band structure calculations of Si–Ge–Sn alloys: Achieving direct band gap materials. *Semiconductor Science and Technology*, vol. 22, no. 7, p. 742, 2007.

[34] D. W. Jenkins and J. D. Dow. Electronic properties of metastable Ge_xSn_{1-x} alloys. *Physical Review B*, vol. 36, no. 15, p. 7994, 1987.

[35] S. Zwerdling, B. Lax, L. M. Roth, and K. J. Button. Exciton and magnetoabsorption of the direct and indirect transitions in germanium. *Physical Review*, vol. 114, no. 1, p. 80, 1959.

[36] S. Groves, C. Pidgeon, A. Ewald, and R. Wagner. Interband magnetoreflection of α-Sn. *Journal of Physics and Chemistry of Solids*, vol. 31, no. 9, p. 2031, 1970.

[37] B. L. Booth and A. W. Ewald. Nonparabolicity of the gray-tin $\Gamma_8{}^+$ conduction band. *Physical Review*, vol. 168, p. 796, 1968.

[38] R. W. Olesinski and G. J. Abbaschian. The Ge-Sn (germanium-tin) system. *Bulletin of Alloy Phase Diagrams*, vol. 5, no. 3, p. 265, 1984.

[39] J. Piao, R. Beresford, T. Licata, W. Wang, and H. Homma. Molecular-beam epitaxial growth of metastable Ge_{1-x} Sn_x alloys. *Journal of Vacuum Science & Technology B: Microelectronics Processing and Phenomena*, vol. 8, no. 2, p. 221, 1990.

[40] F. Gencarelli, B. Vincent, J. Demeulemeester, A. Vantomme, A. Moussa, A. Franquet, A. Kumar, H. Bender, J. Meersschaut, W. Vandervorst, R. Loo, M. Caymax, K. Temst, and M. Heyns. Crystalline properties and strain relaxation mechanism of CVD grown GeSn. *ECS Journal of Solid State Science and Technology*, vol. 50, no. 9, p. 875, 2013.

[41] S. Wirths, D. Buca, and S. Mantl. Si–Ge–Sn alloys: From growth to applications. *Progress in Crystal Growth and Characterization of Materials*, vol. 62, no. 1, p. 1, 2016.

[42] W. Dou, M. Benamara, A. Mosleh, J. Margetis, P. Grant, Y. Zhou, S. Al-Kabi, W. Du, J. Tolle, B. Li, *et al.* Investigation of GeSn strain relaxation and spontaneous composition gradient for low-defect and high-Sn alloy growth. *Scientific Reports*, vol. 8, no. 1, p. 5640, 2018.

[43] L. Wei, Y. Miao, R. Pan, W. wei Zhang, C. Li, H. Lu, and Y.-F. Chen. Highly strained $Ge_{1-x}Sn_x$ alloy films with high Sn compositions grown by MBE. *Journal of Crystal Growth*, vol. 557, p. 125996, 2021.

[44] I. Dascalescu, N. C. Zoita, A. Slav, E. Matei, S. Iftimie, F. Comanescu, A.-M. Lepadatu, C. Palade, S. Lazanu, D. Buca, V. S. Teodorescu, M. L. Ciurea, M. Braic, and T. Stoica. Epitaxial GeSn obtained by high power impulse magnetron sputtering and the heterojunction with embedded GeSn nanocrystals for shortwave infrared detection. *ACS Applied Materials & Interfaces*, vol. 12, no. 30, p. 33879, 2020.

[45] Y.-C. Tai, P.-L. Yeh, S. An, H.-H. Cheng, M. Kim, and G.-E. Chang.

Strain-free GeSn nanomembranes enabled by transfer-printing techniques for advanced optoelectronic applications. *Nanotechnology*, vol. 31, no. 44, p. 445301, 2020.

[46] A. Suzuki, O. Nakatsuka, S. Shibayama, M. Sakashita, W. Takeuchi, M. Kurosawa, and S. Zaima. Growth of ultrahigh-Sn-content $Ge_{1-x}Sn_x$ epitaxial layer and its impact on controlling Schottky barrier height of metal/Ge contact. *Japanese Journal of Applied Physics*, vol. 55, no. 4S, p. 04EB12, 2016.

Chapter 2

Methodology

2.1 Introduction

A brief summary of the key methods utilised in subsequent chapters to analyse the miscibility and electronic structures of the $Ge_{1-x}Sn_x$ systems is provided in this chapter. Emphasis is placed on the underlying theory behind the methods and how they will be utilized in subsequent chapters to investigate $Ge_{1-x}Sn_x$ alloys.

Density functional theory (DFT) is described first, because it is employed as the basis for simulations of periodic $Ge_{1-x}Sn_x$ simulation cells. DFT is chosen to calculate structural and elastic properties, as it has previously been shown to produce accurate results when compared to experimental results [1–4]. DFT is also used to estimate band gaps.

Special quasirandom structures (SQSs) are then discussed, as they provide a means to accurately represent the random nature of alloys at cell sizes that allow for achievable computational times. As DFT implementations used to calculate the elastic properties and electronic structure of solids and thin films make use of continuous boundary conditions, we employ SQSs as a way of imposing

quasirandomness with a relatively small supercell (a cell of a crystal with larger volume than the primitive cell, in this case considered to be the primitive cell of a diamond latice). This allows for calculation of electronic band structures and also provides a means for obtaining key parameters, such as binding energies and elastic constants. Elastic constants that are calculated employing SQSs show an average error on the order of 1% when compared to those calculated with much larger statistically generated random cells [5]. These parameters are then used in models to analyse the miscibility and stability of $Ge_{1-x}Sn_x$ structures.

Two miscibility models are described in this chapter, the first of which is the Bragg-Williams (BW) model [6–8]. This is a simple model which makes use of nearest neighbour binding energies to calculate the formation energy of random alloys. We employ this model as a first pass, as it is very computationally efficient, requiring no more than a handful of first principles calculations to extract the necessary data. The Bragg-Williams model has, however, been shown to predict inaccurate phase diagrams compared to more rigorous models, such as the cluster expansion model (CE) [9]. The CE is the second model employed to calculate alloy miscibility, as this has been shown to accurately predict formation energies of different lattice types (fcc, bcc and hcp) compared to SQS calculations [10].

The methods employed for estimating vibrational and electronic contributions to the free energy are discussed. These properties can also be described with a cluster expansion, and combined with the cluster expansion of the internal energy to produce a temperature dependent model. This can then be coupled with Monte Carlo techniques, allowing for the generation of phase diagrams which compare favourably to previous methods for a number of materials, including SiGe [11].

As well as varying alloy composition, the effects of strain on the alloy are also investigated. By straining the supercells biaxially and letting the direction normal to the strain field relax, a film grown on a substrate is simulated. This

section discusses the models used to analyse the suitability of achievable strain magnitudes for use in devices. The critical thickness model calculates the thickness at which dislocations are energetically favourable in a film, by comparing the energy of the film with and without dislocations. We find in later chapters that this model shows agreement with calculations on the SQSs. Another strain model employed is deformation potential theory (DPT), which allows analysis of the effects of strain on band structures by utilizing deformation potentials and elastic constants.

2.2 Density functional theory

Density functional theory (DFT) is utilized to analyse the structural properties of $Ge_{1-x}Sn_x$. DFT, employing the local density approximation (LDA), is widely used for calculating the elastic and lattice constants of materials, and has been shown to reproduce those of germanium and α-tin accurately [1,12], which will be demonstrated in subsequent chapters. It is therefore employed for the structural relaxations of all the simulation cells in this work. DFT is also used to calculate the energetics required for the miscibility models which are described in later sections. DFT is routinely used in the calculation of phase diagrams using CE methods [11,13,14], and typically exhibits an accuracy on the order of 10 meV per atom in total energy calculations across different phases [13]. This translates to an accuracy of ≈100K in the prediction of transition temperatures, however this will be shown to be sufficient to correctly identify phase orderings and analyse possible trends in the phase diagrams.

2.2.1 The Schrödinger equation

The aim of *ab initio* calculations of electronic structure is solution of the time-independent, non-relativistic Schrödinger equation [15]:

$$\hat{\mathrm{H}}\Psi = E\Psi, \tag{2.1}$$

where $\hat{\mathrm{H}}$ is the Hamiltonian, Ψ is the wavefunction, and E is the energy of the system.

The Hamiltonian for a system of electrons and nuclei in atomic units ($\hbar = m_e = e = 1$) is given as [16]:

$$\hat{\mathrm{H}} = -\frac{1}{2}\sum_{i=1}^{N_e}\nabla_i^2 - \sum_{a}^{N_n}\frac{1}{2m_a}\nabla_a^2 + \frac{1}{2}\sum_{i\neq j}^{N_e}\frac{1}{\mid r_i - r_j \mid} - \sum_{i,a}^{N_e,N_n}\frac{Z_a}{\mid r_i - R_a \mid} + \frac{1}{2}\sum_{a\neq b}^{N_n}\frac{Z_a Z_b}{\mid R_a - R_b \mid}, \tag{2.2}$$

where N_e and N_n are the number of electrons and nuclei, respectively; ∇_i^2 and ∇_a^2 are Laplacian operators taken with respect to the coordinates of the ith electron and ath nucleus, respectively; Z_a is the charge on nucleus a; and r_i and R_a are the coordinates of the electron i and nucleus a, respectively.

The first term on the right hand side of eq. (2.2) corresponds to the kinetic energy of the electrons (T_e), and the second term to the kinetic energy of the nuclei (T_n). The third term is the interaction between electrons (V_{ee}), while the fourth term is the interaction between electrons and nuclei (V_{en}), and the last term is the interaction between nuclei (V_{nn}). This Hamiltonian can be rewritten as:

$$\hat{\mathrm{H}} = T_e + T_n + V_{ee} + V_{en} + V_{nn}. \tag{2.3}$$

However, this is difficult to solve explicitly for anything but simple systems, as the large number of particle interactions becomes mathematically complex and computationally intractable. Thus, approximations must be made in order to

simplify the problem and to enable more complex systems to be studied.

2.2.2 The Born-Oppenheimer approximation

The first such approximation is the Born-Oppenheimer approximation [17]. This is the decoupling of the motion of the electrons and the nuclei, made possible due to the mass of a nucleon far exceeding that of an electron. Therefore, electrons react, in relative terms, instantaneously to changes in the positions of the nuclei.

This allows the term in eq. (2.2) dependent on $\frac{1}{m_a}$ to be ignored, as well as the nuclear-nuclear interactions, as these are fixed for a given set of atomic coordinates. As the Coulomb interaction between nuclei is a constant scalar term for fixed nuclei, it can be ignored for calculations of electronic energies but must be included for calculations of total energies.

The electronic Hamiltonian is then given as:

$$\hat{\mathrm{H}}_{elec} = T_e + V_{ee} + V_{en}, \tag{2.4}$$

where V_{en} is also known as the external potential (V_{ext}), as it is external to the problem considering only the electrons. This leads to the many-electron time-independent Schrödinger equation:

$$\hat{\mathrm{H}}\Psi = [T_e + V_{ee} + V_{ext}]\Psi. \tag{2.5}$$

The total energy of the system (E_{tot}), at a fixed position of nuclei, or geometry, is then given as the sum of the energy of the electrons (E_{elec}) and the nucleus-nucleus repulsion term (V_{nn}):

$$\mathrm{E}_{tot} = \mathrm{E}_{elec} + V_{nn}. \tag{2.6}$$

2.2.3 The Hohenberg-Kohn theorems

At the heart of density functional theory there are two theorems which were put forward by Hohenberg and Kohn in 1964 [18]:

- The first theorem states that, up to an additive constant, the electron density $\rho(r)$ is a unique functional of the external potential V_{ext}. All properties of the system are determined by the external potential.
- The second theorem states that the total energy can be defined as a functional (F) in terms of the density for any V_{ext}. It follows that the density that minimizes the total energy is the ground state density for a given V_{ext}.

Since the ground state energy is a functional of the ground state electron density, so too are the individual components. As such, it follows that:

$$E_0[\rho] = T[\rho] + V_{ext}[\rho] + V_{ee}[\rho]. \tag{2.7}$$

Terms which are universal ($T[\rho]$ and $V_{ee}[\rho]$), and those which are system dependent ($V_{ext}[\rho]$), can then be separated out. The system independent quantities are then merged into F_{HK}, the Hohenberg-Kohn functional:

$$F_{HK} = V_{ee}[\rho(r)] + T[\rho(r)], \tag{2.8}$$

with $E_{ext}[\rho(r)] = \int \rho(r) V_{ext} dr$ we arrive at:

$$E[\rho] = F_{HK}[\rho(r)] + \int \rho(r) V_{ext} dr. \tag{2.9}$$

F_{HK} is universal, and were it known explicitly, the total energy as a functional of the electronic density can be solved, with the ground state energy and electron density obtained by minimizing $E[\rho]$ with respect to the charge density. However,

the explicit form for the universal function of the electron density $F_{HK}[\rho(r)]$ is not known, and as such approximations must be made.

2.2.4 Kohn-Sham DFT

The *Ansatz* of Kohn and Sham is to replace the original many-electron system with a reference system of non-interacting electrons [19]. This allows for a decomposition of eq. (2.8) as:

$$F_{HK}[\rho(r)] = T_{KS}[\rho(r)] + E_{Hartree}[\rho(r)] + E_{xc}[\rho(r)]. \tag{2.10}$$

where $T_{KS}[\rho(r)]$ is the independent kinetic energy of a system of fictitious particles described by wavefunctions $\phi_i(x)$ and is given as:

$$T_{KS}[\rho(r)] = -\frac{1}{2}\sum_i \langle\phi_i|\nabla^2|\phi_i\rangle, \tag{2.11}$$

and $E_{Hartree}[\rho]$ is the Hartree energy (the electrostatic electron-electron interaction) is given as:

$$E_{Hartree}[\rho] = \frac{1}{2}\int \mathrm{d}^3r\mathrm{d}^3r' \frac{\rho(r)\rho(r')}{|r-r'|}. \tag{2.12}$$

$E_{xc}[\rho(r)]$, the exchange correlation energy, consists of the many body terms, which cannot be exactly obtained and is the difference of the kinetic energy and the electron-electron interaction terms between the true system and the fictitious non-interacting system, proposed by Kohn and Sham:

$$E_{xc}[\rho] = \langle\hat{T}\rangle - T_{KS}[\rho(r)] + \langle\hat{V}_{ee}\rangle - E_{Hartree}[\rho]. \tag{2.13}$$

If the exact exchange correlation (XC) energy were known, the exact ground state

energy and density of the system could be obtained from the KS equations, and the electron density would determine the total energy from the time independent Schrödinger equation for a many body system would be solvable.

The variational principle, with respect to the fictitious single-particle orbitals, applied to eq. (2.10) yields the Kohn-Sham(KS) equations:

$$\hat{\mathrm{H}}_{KS}|\phi_i\rangle = \epsilon_i|\phi_i\rangle, \tag{2.14}$$

$$\hat{\mathrm{H}}_{KS} = -\frac{1}{2}\nabla^2 + \hat{V}_{KS}, \tag{2.15}$$

$$\begin{aligned}\hat{V}_{KS} &= \hat{V}_{ext} + \frac{\delta E_{Hartree}}{\delta\rho(r)} + \frac{\delta E_{XC}}{\delta\rho(r)} \\ &= \hat{V}_{ext} + \hat{V}_{Hartree} + \hat{V}_{XC}.\end{aligned} \tag{2.16}$$

The KS equations take the form of independent particle, Schrödinger like equations. The ground state density is given as a function of the KS orbitals(ϕ_i):

$$\rho(r) = \sum_i^N |\phi_i(r)|^2, \tag{2.17}$$

where N is the number of occupied states. This method is limited only by the accuracy of the approximation to the XC functional.

2.2.5 Approximations to the exchange correlation energy

The earliest and simplest approximation to the XC functional is the local density approximation (LDA). First put forward by Kohn and Sham in their original DFT paper [19], the LDA involves calculating the exchange and correlation of a

uniform electron gas. The exchange correlation energy is given as:

$$E_{XC}^{LDA}[\rho] = \int \rho(r)\epsilon_{XC}[\rho(r)]dr, \tag{2.18}$$

where ϵ_{XC} is the exchange-correlation energy per particle for the uniform electron gas of density ρ. Therefore, the XC energy in this approximation is a function of only the charge density. Throughout this thesis, the LDA is employed when using DFT to calculate elastic and structural properties. A number of approximations to the XC functional have previously been compared for the accuracy of which they reproduce the elastic properties of materials, including the group IV materials [1]. In this study, the LDA has been shown to provide greater accuracy than the generalized gradient approximation (GGA) at reproducing experimental values for elastic constants. The LDA is also shown to have comparable accuracy to the much more computationally demanding hybrid functionals for group IV materials, such as C, Si, and Ge, for the elastic constants.

The electronic band structures of materials can also be calculated using the Kohn-Sham approximation eigenvalues as single electron energies. Though DFT, using the Kohn-Sham eigenvalues, is well known to underestimate band gaps [20], the modified Becke-Johnson (mBJ) meta-GGA functional has been shown to produce these accurately compared to experimental results [21], and as such is used in our electronic structure calculations. Though meta-GGA calculations do require the fitting of a "c-parameter" to experimental data if it cannot be found self consistently.

Whereas LDA approximations include the local density, and generalized gradient approximations (GGA) include the gradient of the density, meta-GGA functionals, such as mBJ meta-GGA, also include the kinetic-energy density (T) in the XC functional. mBJ meta-GGA has been previously shown to accurately reproduce band gaps for a variety of materials, including the group IV materials, C, Si,

and Ge, and shows a comparable accuracy to hybrid functionals and even *GW* calculations [21]. Due to the derivative discontinuity in the exchange correlation when approximated by the LDA, DFT with LDA is known to underestimate bandgaps [20]. As such, mBJ meta-GGA is employed, as put forward by Tran and Blaha, in almost all of the calculations of electronic band structures in this work [21].

The correlation potential employed in the mBJ approximation is the LDA correlation. The exchange potential is given as:

$$v_x^{mBJ}(r) = cv_x^{BR}(r) + (3c-2)\frac{1}{\pi}\sqrt{\frac{5}{12}}\sqrt{\frac{2T(r)}{\rho(r)}}, \tag{2.19}$$

where $T(r) = 1/2\sum_{i=1}^{N}|\nabla\psi_i(r)|^2$ is the kinetic energy density, and $\phi_i(r)$ is the i'th Kohn-Sham orbital. v_x^{BR} is the Becke-Roussel exchange potential. This is an approximation of the potential generated by the exact exchange hole, known as the Slater potential [22, 23].

c in eq. (2.19) can be solved for during the self-consistency cycles required to solve the Kohn-Sham equations, based on the following equation:

$$c = \alpha + \beta\left[\frac{1}{\Omega}\int_{\Omega}\frac{|\nabla\rho(r)|}{\rho(r)}dr\right]^{\frac{1}{2}}, \tag{2.20}$$

where Ω is the volume of the cell, $\alpha = -0.012$, and $\beta = 1.023$ Bohr$^{\frac{1}{2}}$. α and β were obtained from fitting to experimental band gaps of a variety of semiconductors and insulators. The c-parameter can also be obtained through fitting to experimental data, as is the approach taken in this work. This approach is chosen as it provides accurate band structures for the alloy components, as demonstrated in later chapters.

2.3 Special quasirandom structures

A recent theoretical study has suggested that short range ordering (SRO) may be present within the $Ge_{1-x}Sn_x$ alloy [24], such that there is an energetic penalty associated with the formation of Sn-Sn nearest-neighbour bonds, with this SRO then acting to increase the band gap at fixed Sn composition x by up to 0.1 eV at Sn compositions relevant to the semiconducting to semimetallic transition. However, it is of note that the Monte Carlo simulations that displayed this SRO were conducted at temperature T = 300 K, approximately 350 K lower than the temperature range in which $Ge_{1-x}Sn_x$ alloys are grown. As temperature is increased, the aforementioned energetic penalty driving the emergence of SRO in these Monte Carlo simulations is likely to be suppressed. The penality is raised to the power n^{-1} when the simulation temperature is raised by a factor of n. Therefore, at temperatures relevant to $Ge_{1-x}Sn_x$ alloy growth SRO will be strongly suppressed, with minimal deviation from statistically random alloy disorder expected. As such, in this thesis, the distribution of Ge and Sn atoms in the $Ge_{1-x}Sn_x$ alloy is taken to be fully random. Random, in this case, meaning that for the binary $Ge_{1-x}Sn_x$ alloy, each lattice site has a probability $1-x$ of being occupied by a Ge atom, and a probability x of being occupied by a Sn atom, with the probabilities being independent of any crystal site. This approach is commonly employed in theoretical calculations for $Ge_{1-x}Sn_x$ alloys which have demonstrated good, quantitative agreement with experimental measurements. [12, 25–29].

Density functional theory for the description of infinite or semi-infinite materials makes use of periodic boundary conditions in order to model crystalline materials. However, capturing properties of a truly random alloy would require an extremely large supercell to ensure the site correlation functions are converged. Calculations on simulation supercells large enough to reproduce the correlation functions for a

random alloy are computationally intractable in DFT, particularly if these are to be used in conjunction with Monte Carlo techniques. This is due to the extremely large simulation cell required to represent a random alloy.

To overcome this limitation, special quasirandom structures (SQSs) have been developed [30]. These structures provide a way of mimicking a true random alloy with a much smaller simulation cell by replicating lower order multisite correlation functions of an ideal random alloy. This greatly reduces the computation resources required to obtain alloy properties while also producing reliable results. It has previously been shown that an SQS as small as 32 atoms can accurately represent the elastic constants of face-centred cubic (FCC) aluminium titanium (AlTi) alloys, with an average error of 1% when compared to those obtained from averages over ten DFT calculations for randomly generated 4000 atom cells across the full alloy composition range [5].

The correlation functions of a cell are obtained by assigning a value of -1 and +1 to each lattice site, dependent on which of the alloy components occupies a site, analogous to an Ising spin model. A two dimensional (2D) representation of this is depicted in fig. 2.1.

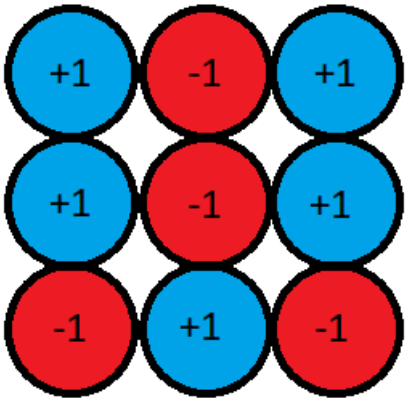

Figure 2.1: Representation of a 2D Ising lattice, with spin up and spin down sites. The correlation functions for the random alloy are analogous to the spin correlations.

For a given cluster at location l (l also including orientation), with configuration σ, the multiplication of the Ising "spin" variables of the lattice sites in this cluster is denoted as $\Pi_c(\sigma, l)$. The cluster outlined in fig. 2.2 is an example of a triplet cluster. Through multiplication of values assigned to each atom within the cluster, it is shown to have $\Pi_c(\sigma, l)$ = -1.

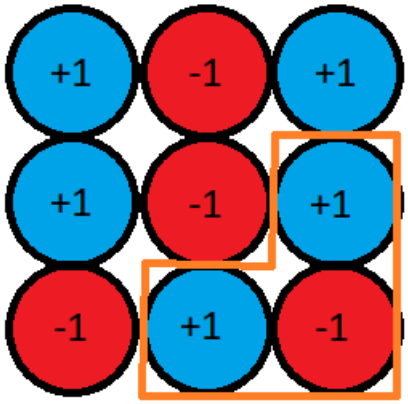

Figure 2.2: Representation of a 2D Ising lattice, with a triplet cluster outlined.

An average is taken of $\Pi_c(\sigma, l)$ over all values of l to provide the correlation function for a specific cluster type.

Using Monte Carlo techniques many quasi-random lattice configurations may be compared to the ideal random correlation functions. These are derived from the fact that in a *truly* random alloy the probabilities of site occupancies are independent, but correlations between lattice sites will arise related to the alloy composition when averaged over a large number of configurations. As such, the probability of a site having a "spin" of +1 is x and having a "spin" of -1 is $1 - x$. A site in a random configuration has an average "spin" value given as $(1)(x) + (-1)(1 - x)$, which is the sum of "spin" values multiplied by their respective probabilities. This simplifies to $2x - 1$. For a cluster with k vertices (lattice sites) and a range (maximum distance between two atoms) of m, the random correlation function is given as:

$$\bar{\Pi}_{k,m} = (2x - 1)^k. \tag{2.21}$$

Once a desired level of accuracy is reached between the calculated and ideal correlation functions, the cell can then be utilized in DFT calculations for both electronic and structural properties of a random alloy [31].

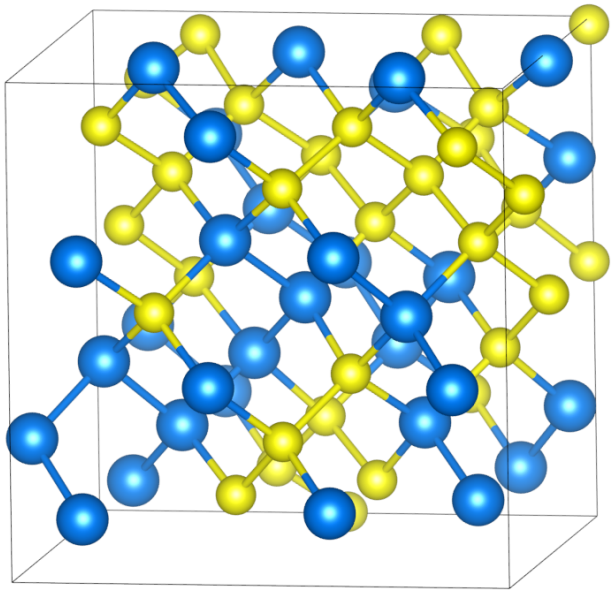

Figure 2.3: An example of an x=0.5, 64 atom $Ge_{1-x}Sn_x$ SQS, with yellow atoms representing Ge and blue atoms representing Sn, or vice versa if radii are ignored.

SQSs are used to represent alloys in all of the DFT calculations presented in this work. A representation of one such SQS, a x=0.5, 64 atom structure is depicted in fig. 2.3.

2.4 Binary alloy miscibility

To analyse the miscibility of a system, the key quantity to be determined is the free energy. In particular, the Helmoholtz free energy (F) is of interest [32]; that is, the available work in a system at constant pressure and volume. This is given

by:

$$F = E - TS, \tag{2.22}$$

where E is the internal energy of the system, T is the temperature, and S is the total system entropy.

If two alloy configurations at constant composition and temperature are compared, the configuration with lower F is more stable. To calculate the miscibility of a system over a composition range, an intractable number of first principles calculations are required to determine the needed energies. The following sections will describe how to approximate E using efficient computational methods, as well as the other contributions to the free energy of binary alloy systems.

2.4.1 The Bragg-Williams miscibility model

The Bragg-Williams model [6–8] is a simple model that can be applied to estimate the free energy of an alloy system. It predicts the mean field average of internal energy (E_i) and then takes into consideration only the configurational entropy (S_c) to calculate the free energy of a random alloy. The shape of the free enery curve with respect to composition indicates the miscibility of alloy. A concave free energy curve denotes the ability for the two alloy components to form a solid solution. Convex portions of the curve indicate miscibility gaps.

E_i is determined by the binding energy within the system. If V_{ij} is the binding energy between atoms of type i and j, then:

$$E_i = N_{\mathrm{GeGe}}V_{\mathrm{GeGe}} + N_{\mathrm{SnSn}}V_{\mathrm{SnSn}} + N_{\mathrm{GeSn}}V_{\mathrm{GeSn}}, \tag{2.23}$$

where N_{ij} is the number of nearest neighbour bonds between atoms of type i and

type j. Equation (2.23) can be simplified to:

$$E_i = \frac{Nz}{2}\{(1-\mathrm{x})V_{\mathrm{GeGe}} + \mathrm{x}V_{\mathrm{SnSn}} + 2\mathrm{x}(1-\mathrm{x})V\}, \tag{2.24}$$

where x is the concentration of Sn atoms, z is the number of nearest neighbours of each atom, and N is the total number of atoms. V is the relative binding energy of the system, this is the difference between the energy of a GeSn bond and the average energy of a GeGe bond and a SnSn bond, given as:

$$V = V_{\mathrm{GeSn}} - \frac{1}{2}(V_{\mathrm{GeGe}} + V_{\mathrm{SnSn}}). \tag{2.25}$$

This is a simple indication of the miscibility of the system. Negative V indicates that GeSn bonds are energetically favourable relative to forming SnSn and GeGe bonds. A positive V indicates that segregation is preferred, in order to maximise the number of SnSn and GeGe bonds. This is only strictly true at 0 K, as the entropy contribution to the free energy can overcome a positive relative binding energy and drive the system towards randomness.

Now that an approximation for E in eq. (2.22) has been obtained, the entropy must be estimated. The Bragg-Williams model takes into account only the configurational entropy. The configurational entropy is based solely on the number of possible configurations of the atoms in the lattice. For N total particles there are $N!$ different ways of distributing the atoms over N sites. Configurations which differ only by interchanging one Ge atom with another Ge atom are indistinguishable, and the same holds true for Sn atoms. This leads to the total number of distinguishable configurations to be:

$$\Omega = \frac{N!}{N_{\mathrm{Ge}}!N_{\mathrm{Sn}}!}. \tag{2.26}$$

Assuming that the weighting of each configuration is approximately independent of how the atoms arrange in the system, then the configurational entropy is given as:

$$S_c = kln(\Omega) = k[ln(N!) - ln(N_{\mathrm{Ge}}!) - ln(N_{\mathrm{Sn}}!)]. \tag{2.27}$$

Applying Sterling's approximation $ln(N!) = Nln(N) - N$ to this results in:

$$Sc = k[Nln(N) - N_{\mathrm{Ge}}ln(N_{\mathrm{Ge}}) - N_{\mathrm{Sn}}ln(N_{\mathrm{Sn}})], \tag{2.28}$$

which can be simplified to:

$$S_c = -kN[\mathrm{x}ln(\mathrm{x}) + (1-\mathrm{x})ln(1-\mathrm{x})]. \tag{2.29}$$

Substituting eq. (2.29) and eq. (2.24) into eq. (2.22) allows for a simple method for approximating the free energy.

The Bragg-Williams approximation is valid for analysing the miscibility of a system when nearest neighbour interactions dominate, providing data on how the alloy is expected to behave with a very low computational cost, and requiring just a minimal set of DFT calculations. However, as will be shown in later chapters, the model lacks accuracy when compared to models which extend to beyond nearest neighbours. While nearest neighbour interactions tend to be the largest contribution, longer range couplets and all interactions are ignored in the BW model. Including these interactions increases the accuracy of predicted internal energies, and this can be achieved through the use of a cluster expansion of the system.

2.4.2 The cluster expansion formalism

The cluster expansion (CE) formalism is a standard approach for calculating the internal energy of an alloy configuration in order to obtain the free energy [11]. A cluster expansion allows for a predictive way to calculate the internal energy of a system, taking in to account longer range interactions beyond nearest neighbours as well as clusters containing more than two atoms.

The main principle behind the cluster expansion is that a configuration dependent property of an alloy can be written in terms of the clusters present in each configuration. To do this, the correlation function $\bar{\Pi}_\alpha$ for each cluster type (α) is first calculated. As in the SQS method, a variable is assigned at each atom site. For a binary alloy the variable is either +1 or -1, depending on the atom type occupying the site, similar to the Ising model. The correlation function is again found for a given cluster by multiplying the "spins" of each instance of that cluster, and then averaging over the number of instances of that cluster in a given configuration (σ). The energy per atom of the configuration is then given as:

$$E(\sigma) = \sum_\alpha J_\alpha \hat{\Pi}_\alpha(\sigma), \tag{2.30}$$

where J_α gives the averaged interaction for a cluster type α, also known as effective cluster interactions (ECIs).

Knowing the value of every ECI of a system yields the ability to predict the internal energy for any configuration. However, as the magnitudes of the ECI decrease with cluster range, not every ECI is required. The required ECI can be determined by fitting to a relatively small number of simulation cells of known energy, in this case from DFT calculations. This is known as the structure inversion method, or the Connolly-Williams method [13].

The implementation utilized in this work, the Alloy Theoretic Automated Toolkit

(ATAT) [10, 14], uses a least squares fit to calculate the ECI, while also using a cross validation (CV) score to assess the predictive power of the fit of the cluster expansion to the alloy energies. The CV score is analogous to root mean square error. However, it is adapted to estimate the error for structures not included in the least squares fit. It is given as:

$$CV = \left(\frac{1}{n} \sum_{i=1}^{n} \left(E_i - \hat{E}_{(i)} \right)^2 \right)^{\frac{1}{2}}, \tag{2.31}$$

where n is the number of structures, E_i = the energy of structure i as calculated from DFT, and $\hat{E}_{(i)}$ is the predicted value of the energy of structure i obtained from the least-squares fit to the (n -1) other known energies, excluding structure i.

A module of ATAT, the MIT Ab-initio phase-stability (maps) code [11], can be used to automatically construct a cluster expansion for an alloy. To do this, it first determines which clusters to include. This is done with the intent of lowering the CV score, as well as applying two rules. The first rule is that a cluster can be included only if each of it subclusters has already been included in the CE. If this rule is not followed it leads to a merging of the ECI of that cluster with the subcluster's ECI, leading to inaccuracy in the cluster expansion. The second rule is that for a cluster with m vertices to be included, all clusters with m vertices encompassed in a smaller diameter must also be included. As shorter range interactions are usually of larger magnitude than long range interactions, addition of shorter range clusters has more of an impact on the calculated energies.

The next step in the automatic construction of the cluster expansion is the choice of structures from which to extract the ECIs. Selecting random structures might introduce a bias into the ECI as well as create a variance around the mean ECIs. Bias cannot be determined without knowledge of the energy of a candidate structure, requiring a first principles calculation. As such, the focus is placed on

reducing the variance about the mean when selecting the structures. The CE can also be performed by choosing the structures and ECI manually, however care must be taken that the CV score of the fit is reasonable in order for the CE to produce reliable predictions.

The strength of the cluster expansion is in its ability to predict the energy (or any other configuration dependent property) of a large number of structures at a very low computational cost. With a cluster expansion, the calculation of the energy of a cell is reduced to calculating the correlation functions, which is a comparatively trivial computational operation. As such, a cluster expansion can then be used as a Hamiltonian for a Monte Carlo simulation. This allows for the comparison of free energies between a large number of cell configurations over the full composition range of the alloy, leading to the calculation of free energy versus composition phase diagram to determine the temperature transition between miscibility and immiscibility.

2.4.3 Finite temperature effects in the cluster expansion

As already discussed, configurational entropy has been estimated from Boltzmann's expression for entropy by accounting for all of the possible ways of arranging atoms in a cell given its composition, as described in 2.29. However, this term is not necessary for phase diagram calculations. The Monte-Carlo techniques already account for configurational entropy, as the simulation samples accessible configurations at a given temperature.

Other finite temperature effects are incorporated into the study by estimating free energy contributions arising from vibrational and electronic degrees of freedom. Electronic contributions to the free energy are computed within the one-electron and temperature-independent bands approximations by employing the electronic density of states (DoS) as computed from the Kohn-Sham eigenvalues obtained

from the DFT calculations [33]. Electronic entropy $S_e(T)$ is the entropy associated with an electron's probabilistic occupation of states, and is related to the DoS $g(\epsilon)$ by [34]:

$$S_e(T) = -k_B \int [f_{\mu,T}(\epsilon) ln(f_{\mu,T}(\epsilon)) + (1 - f_{\mu,T}(\epsilon)) ln(1 - f_{\mu,T}(\epsilon))] g(\epsilon) d\epsilon, \quad (2.32)$$

where $f_{\mu,T}(\epsilon)$ is the Fermi-Dirac distribution given by:

$$f_{\mu,T}(\epsilon) = \left(1 + exp\left(\frac{\epsilon - \mu}{k_B T}\right)\right)^{-1}, \quad (2.33)$$

where μ is chemical potential, given as the solution of $\int f_{\mu,T}(\epsilon) g(\epsilon) d\epsilon = n_e$, where n_e is the total number of electrons.

Vibrational contributions, including entropy and zero point energy, are computed using the *bond stiffness versus bond length* approach. This involves estimating the phonon frequencies in the alloy via a nearest-neighbour bond length versus bond stiffness model, where the bond length dependent force constant tensors are obtained by computing reaction forces on crystalline structures perturbed with strain and atomic displacement [35, 36]. This model has previously been shown to give reliable results for gold-palladium (AuPd) alloys, and copper-palladium (CuPd) alloys, compared to models which use full-force constant matrices and all nearest neighbours. This model also accurately produces results for copper-gold (CuAu) systems compared to previous theoretical and experimental work [37]. This has also previously been used to calculate the vibrational contributions to the free energy of palladium-vanadium(PdV) and nickel-aluminium (NiAl) alloys [35], with both materials showing very good agreement with a more rigorous first-nearest-neighbour spring model. The bond stiffness versus bond length model has previously been employed to estimate the vibrational contributions to free energy for variable band gap semiconductor alloys such as indium gallium nitride

(InGaN), aluminium gallium nitride (AlGaN), and aluminium indium nitride AlInN, all systems which exhibit larger lattice mismatch than GeSn [38].

Three crystalline structures are chosen to calculate the stretching and bending terms: i) elemental Ge; ii) elemental Sn; and iii) a fictitious GeSn zinc-blende structure. The maximum distance between perturbed atoms is set as 1.2 nm, allowing for the use of 64 atom supercells. The maximum atomic displacement is limited to 0.02 nm, relative to relaxed geometry, and the perturbations are performed at 10 differing strain values. Figure 2.4 shows the stretching and bending terms for each of the bond types that can be present in $Ge_{1-x}Sn_x$ alloys: Ge-Ge, Ge-Sn, and Sn-Sn. The proximity of the polynomial fit to the calculated values shows the predictive power of the fit in these materials [33].

Once a vibrational DoS of a structure is calculated, the vibrational contributions to the free energy(F_{vib}) can be calculated from [34]:

$$F_{vib} = k_B T \int_0^\infty ln\left(2sinh\left(\frac{hv}{2k_B T}\right)\right) g(v)dv \tag{2.34}$$

where v is the frequency, and $g(v)$ is the phonon density of states.

2.4.4 Monte Carlo method

To calculate phase boundaries, the "phb" code [39,40] from the ATAT package is employed. The cluster expansion reduces the calculation of the internal energy (and vibrational entropy) to a simple linear equation on an Ising like lattice, allowing many alloy configurations to be calculated in a short amount of time and making it an ideal Hamiltonian for Monte Carlo calculations. The phb code makes use of semi-grand canonical ensemble (SGCE) Monte Carlo methods. In the SGCE, the number of atoms is fixed while the composition and energy are allowed to vary, based on an externally imposed temperature and externally imposed

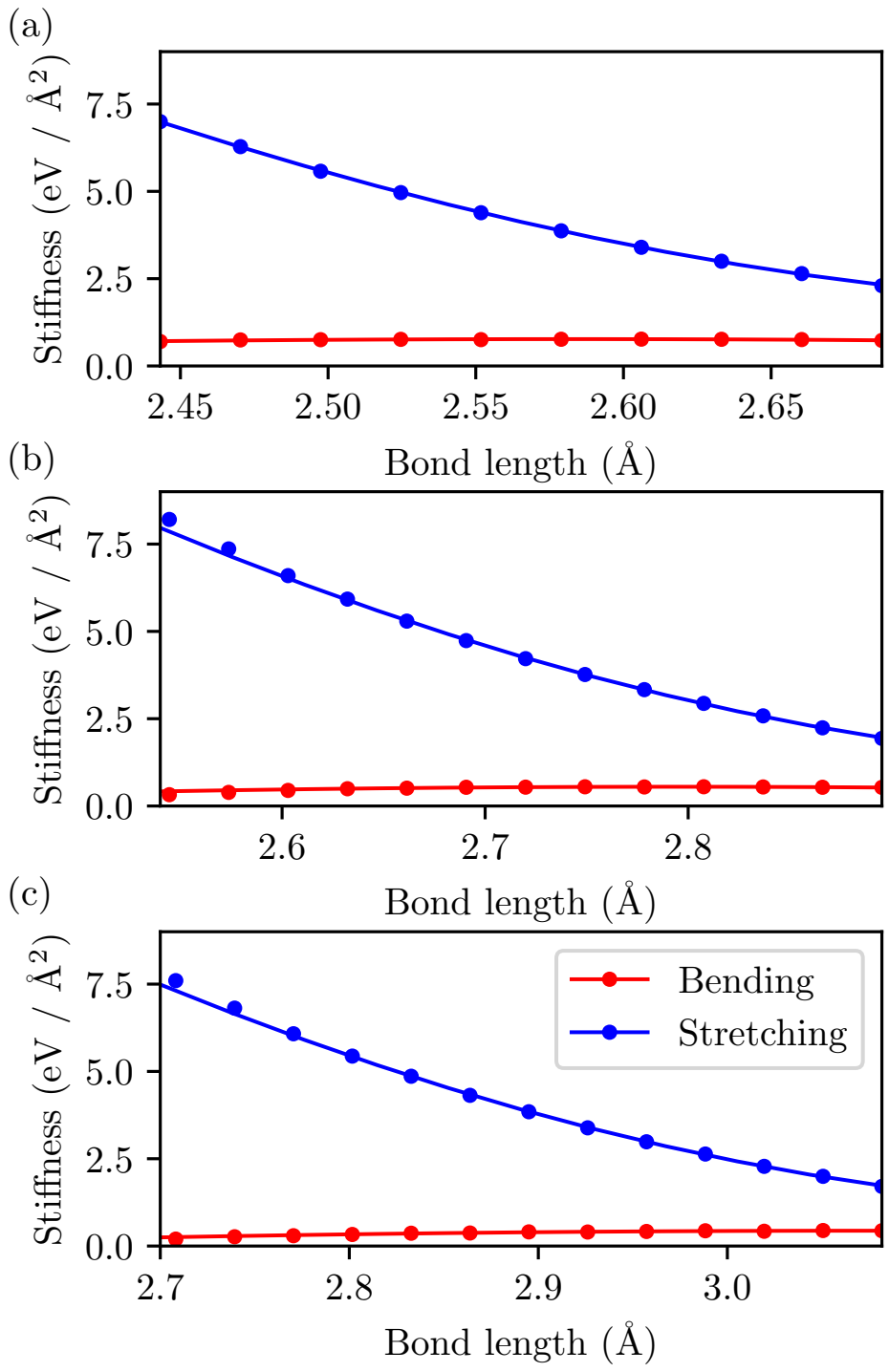

Figure 2.4: Stretching and bending terms of the nearest neighbour spring model as a function of bond length for (a) Ge-Ge, (b) Ge-Sn, and (c) Sn-Sn bonds. Circles show the values calculated with DFT while lines correspond to a three-parameter polynomial fit.

difference in chemical potential between the two atom types ($\mu = \mu_a - \mu_b$). μ is also defined as the rate of change in free energy with respect to change in alloy composition.

In the SGCE the thermodynamic potential is given as:

$$\phi(\beta, \mu) = -\frac{1}{\beta N} ln\left(\sum_i (-\beta N(E_i - \mu \mathrm{x}_i))\right), \tag{2.35}$$

where E_i and x_i are the internal energy and alloy composition of alloy state i, N is the number of atoms, and $\beta = \frac{1}{k_B T}$. The Helmholtz free energy is related to the thermodynamic potential through $\phi = F - \mu \mathrm{x} = E - TS - \mu \mathrm{x}$. A lower ϕ indicates a more stable phase. At an equilibrium point, ϕ is equal for both phases [40, 41].

To determine ϕ, the semi-grand canonical ensemble Monte Carlo method is used. In the semi-grand canonical ensemble the number of atoms is fixed, with the energy and composition allowed to fluctuate based on an externally imposed difference in chemical potential between the two atom types as well as an externally imposed temperature [41]. Equilibration are excluded from measurements to allow for the system to reach convergence for a given set of externally imposed variables. Averaging passes are those following the equilibration passes, over which the thermodynamic quantities in question are averaged. The number of averaging and equilibrium passes are chosen automatically based on the algorithms described in Ref. [41] with a chosen precision. The equilibration process is stopped, and averaging is begun once the targeted average change in the thermodynamic quantity in question has achieved the desired precision. Averaging of the quantity is stopped once the variance about the average of the quantity decreases below a threshold based on the target precision.

Changes in phase are detected by fitting a polynomial to a thermodynamic quantity, such as a short range order parameter. This polynomial is then extrapolated

for the next step in the simulation, with significant deviations between the extrapolated value and the calculated value signalling a phase transition [41]. The order of this polynomial is determined by making use of the CV score described by eq. (2.31).

2.5 Alloy strain

The application of strain to a semiconductor or semimetal is known to alter both the miscibility and the band gap energy. In germanium, tensile strain has been shown to induce an indirect to direct band gap transition at a tensile epitaxial strain range between 1.5% and 1.9% [27, 42, 43]. Thus, the role of strain on the band gap can be a major aid in achieving desirable electronic band structure properties.

However, strain can also hinder the growth of alloy structures. $Ge_{1-x}Sn_x$ films of x=0.46, grown on Ge(100) have previously been reported in the literature, but the large compressive strains limit the thickness of these films to just 3 nm [44]. Lattice matched substrates have been reported to allow growth of alloys with compositions $0.26 < x < 0.99$ and can even stabilize pure α-Sn films with thicknesses in excess of 100 nm and temperatures up to 343 K [45–50] .

This section will describe the models employed to assess the impact of strain on the stability and band structure of the material to investigate its effects on the miscibility energetics and electronic structure calculations. In chapter 3, it is found that epitaxial strain in the plane perpendicular to the $\langle 100 \rangle$ direction decreases the epitaxial softening function of the materials. The epitaxial softening function quantifies the degree that out-of-plane relaxation can stabilise an epitaxially grown thin film. As such, only strain along this plane is considered.

2.5.1 Critical thickness

To measure the impact of epitaxial strain on the growth of the alloys, the critical thicknesses for thin films are calculated. This is the thickness that plastic relaxation via the formation of dislocations and related crystalline defects first becomes energetically favourable, as depicted in fig. 2.5 [51–53].

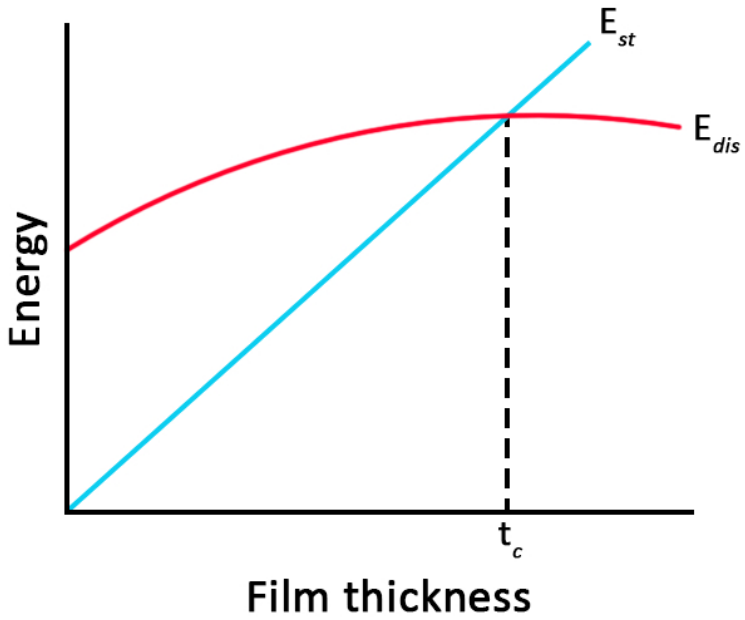

Figure 2.5: Representation of the strain energy in a layer, (E_{st}), and the energy of the layer with a disclocation (E_{dis}) as a function of layer thickness. t_c here is the critical thickness.

E_{st} in fig. 2.5, the areal strain energy density of the film without dislocations, can be obtained from elastic continuum theory. Within elastic continuum theory, the elastic energy per unit volume (U) is given as [54]:

$$\begin{aligned} U = &\frac{1}{2}C_{11}(\epsilon_{xx}^2 + \epsilon_{yy}^2 + \epsilon_{zz}^2) \\ &+ C_{12}(\epsilon_{xx}\epsilon_{yy} + \epsilon_{xx}\epsilon_{zz} + \epsilon_{yy}\epsilon_{zz}) \\ &+ 2C_{44}(\epsilon_{xy}^2 + \epsilon_{yz}^2 + \epsilon_{yz}^2) \end{aligned} \tag{2.36}$$

where ϵ denotes the components of the strain tensor in Voigt notation and C

denotes the elastic constants of the material, which have been obtained from DFT calculations. For the case of biaxial strain, $\epsilon_{xx} = \epsilon_{yy}$, $\epsilon_{zz} = -\frac{2C_{12}}{C_{11}}\epsilon_{xx}$ and $\epsilon_{xy} = \epsilon_{yz} = \epsilon_{yz} = 0$. This reduces eq. (2.36) to:

$$\frac{C_{11}^2 + C_{11}C_{12} - 2C_{12}^2}{C_{11}}\epsilon_{xx}^2, \tag{2.37}$$

where $\mathrm{G} = \frac{1}{2}(C_{11} - C_{12})$ is the shear modulus and $\sigma = \frac{C_{12}}{C_{11}+C_{12}}$ is Poisson's ratio for the layer. By multiplying by the thickness t, this reduces to [51, 55]:

$$E_{st} = 2\mathrm{G}\left(\frac{1+\sigma}{1-\sigma}\right)\epsilon_{xx}^2 t. \tag{2.38}$$

To compute E_{dis} the method put forward by Voisin [52] is chosen, which, for an epitaxially strained layer of a diamond or zinc-blende structure grown on an (100)-oriented substrate, leads to the critical thickness t_c given as:

$$t_c = \frac{a_S}{8\sqrt{2}\pi|\epsilon_{xx}|}\left(\frac{4-\sigma}{1+\sigma}\right)\left(1 + \ln\left(\frac{\sqrt{2}t_c}{a_s}\right)\right), \tag{2.39}$$

where a_S is the substrate lattice constant.

While there exist many approaches [51] to compute t_c, eq. (2.39) has been demonstrated to produce estimates which are in good agreement with experimental measurements for a range of semiconductor materials, including group-IV $\mathrm{Si_xGe_{1-x}}$, III-V $\mathrm{In_xGa_{1-x}As}$ alloys [51, 52], and highly-mismatched III-V alloys containing nitrogen and bismuth [53,56]. An example of such a calculation is shown in fig. 2.6 for GaAs alloyed with Bi to introduce compressive strain and GaAs alloyed with As to introduce tensile strain, both on a GaAs substrate. The critical thickness model will be utilized in this work in a similar manner, to track how the critical thickness changes on a given substrate as alloy composition varies.

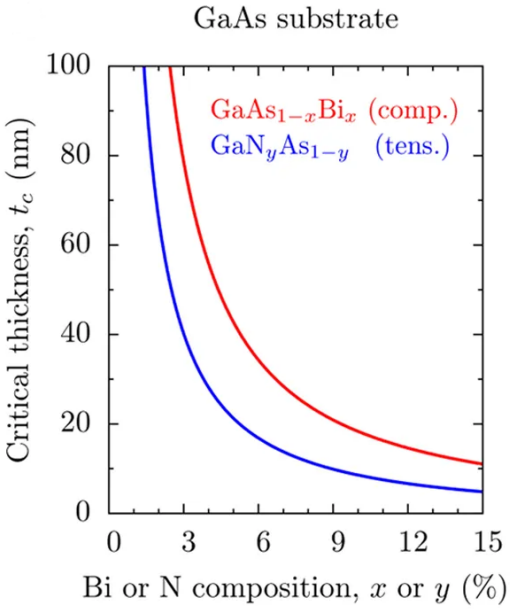

Figure 2.6: Critical thickness of $GaAs_{1-x}Bi_x$ and GaN_yAs_{1-y} as a function of alloy composition, grown on a GaAs substrate. Reproduced from [56].

This method for calculating the critical thickness is shown to give lower values when compared to experimental results. This is due to a metastable region where layers of the material above t_c can be grown, and as such the experimental thickness is dependent on growth rate and temperature [51]. Figure 2.6 shows the calculated critical thicknesses of $GaAs_{1-x}Bi_x$ and GaN_yAs_{1-y} as a function of alloy composition as grown on a GaAs substrate. The strain-thickness limit calculated for these layers on the GaAs substrate [56] was found to be consistent with previously obtained experimental data for $GaAs_{1-x}Bi_x$ [57].

The critical thickness is relevant to this work as it provides a guideline to the maximum thicknesses that can be reached as strain is applied to the alloy. This is an important factor when choosing alloy and strain parameters, as it must be possible for films to be grown to thicknesses above which confinement effects do not cause the opening of a band gap, in order for semimetallic alloy structures to be grown on a chosen substrate.

2.5.2 Deformation potential theory

Deformation potential theory [58–60] makes use of elastic constants and deformation potentials to predict band gap shifts due to epitaxial strain. These shifts are composed of two components: the shift brought about due to the volume change of a cell and the valence band splitting as a result of axial strain.

To calculate the band gap shift due to volume change, first the volume change itself must be obtained from the elastic constants. For a material with an equilibrium lattice constant (a_0) biaxially strained to a difference lattice constant ($a_{\parallel}$), the fractional change in lattice parameter parallel to the surface (ϵ_{xx}) can be given as:

$$\epsilon_{xx} = \frac{a_{\parallel}}{a_0} - 1. \tag{2.40}$$

The fractional change in lattice parameter normal to the surface (ϵ_{zz}) is given as:

$$\epsilon_{zz} = -D \times \epsilon_{xx}, \tag{2.41}$$

where D is dependent on the elastic constants C_{11}, C_{12}, and C_{44}, as well as the orientation of the strain. For biaxial strain in the plane perpendicular to the [100] direction, this is given as:

$$D^{100} = 2\frac{C_{12}}{C_{11}}. \tag{2.42}$$

The band gap energy E_g brought about by the fractional volume change $\frac{\Delta\Omega}{\Omega} = \epsilon_{xx} + \epsilon_{yy} + \epsilon_{zz}$ can then be calculated from:

$$E_g = E_g^0 + a_g\frac{\Delta\Omega}{\Omega}, \tag{2.43}$$

where E_g^0 is the unstrained band gap and a_g is the deformation potential of the

gap.

The second component, the valence band splitting, is caused by the out of plane relaxation and the spin orbit splitting, resulting in the heavy hole (HH), light hole (LH), and spin split off bands shifting relative to each other. The HH and LH bands are marked as Γ_8^+ and the spin split off band is marked as Γ_7^+ on fig. 1.8 in chapter 1. For biaxial strain along the (100) plane, the HH splitting ($\Delta E_{v,2}$), the LH splitting ($\Delta E_{v,1}$), and spin split off splitting ($\Delta E_{v,3}$), relative to the unstrained LH and HH bands in terms of the deformation potentials, can be obtained from diagonalizing the 8 band $\mathbf{k} \cdot \mathbf{p}$ Hamiltonian matrix for k = 0 [61, 62] and are given as:

$$\Delta E_{v,2} = -\frac{1}{2}\delta E_{100}, \tag{2.44}$$

$$\Delta E_{v,1} = -\frac{1}{2}\Delta_0 + \frac{1}{4}\delta E_{100} + \frac{1}{2}\left[\Delta_0^2 + \Delta_0 \delta E_{100} + \frac{9}{4}(\delta E_{100})^2\right]^{\frac{1}{2}}, \tag{2.45}$$

$$\Delta E_{v,3} = -\frac{1}{2}\Delta_0 + \frac{1}{4}\delta E_{100} - \frac{1}{2}\left[\Delta_0^2 + \Delta_0 \delta E_{100} + \frac{9}{4}(\delta E_{100})^2\right]^{\frac{1}{2}}. \tag{2.46}$$

where b is the uniaxial deformation potential, Δ_0 is the spin orbit splitting parameter, and δE_{100} is given as:

$$\delta E_{100} = 2b(\epsilon_{zz} - \epsilon_{xx}). \tag{2.47}$$

The above equations return values of 0, 0 and $-\Delta_0$ for $\Delta E_{v,2}$, $\Delta E_{v,1}$, and $\Delta E_{v,3}$ respectively for a zero strain system. By observing which of these band experiences the greatest upwards shift in energy and combining this with the value obtained from the volume deformation, the effects of epitaxial strain on the band gap can be estimated.

Elastic constant bowing parameters obtained from SQS calculations are employed to produce predictions of how the "indirect" and "direct" band gap would behave

were there no band mixing in the electronic structure. For an alloy, the uniaxial deformation potentials (b) are approximated by linear interpolation. This has been shown to be a good approximation for SiGe alloys [63,64]. a_g for the energy separation of the Γ_7^-- Γ_8^+ derived states is obtained via fitting of the DPT band gap values to those calculated within DFT for strained SQS cells. The fitted value is compared to a_g as calculated from a linear interpolation between the pure α-Sn and Ge value. By analysing the fitted a_g, conclusions can be drawn for the behaviour of the band gap under strain and how it is affected by band hybridization. Deformation potential theory is also used in later chapters to construct a model for the prediction of the band gap of epitaxially strained $Ge_{1-x}Sn_x$ across the full alloy composition range.

References

[1] M. Råsander and M. A. Moram. On the accuracy of commonly used density functional approximations in determining the elastic constants of insulators and semiconductors. *The Journal of Chemical Physics*, vol. 143, no. 14, p. 144104, 2015.

[2] G. Ortiz. Gradient-corrected pseudopotential calculations in semiconductors. *Physical Review B*, vol. 45, no. 19, p. 11328, 1992.

[3] L. He, F. Liu, G. Hautier, M. J. T. Oliveira, M. A. L. Marques, F. D. Vila, J. J. Rehr, G.-M. Rignanese, and A. Zhou. Accuracy of generalized gradient approximation functionals for density-functional perturbation theory calculations. *Physical Review B*, vol. 89, no. 6, p. 064305, 2014.

[4] O. H. Nielsen and R. M. Martin. Stresses in semiconductors: *Ab initio* calculations on Si, Ge, and GaAs. *Physical Review B*, vol. 32, no. 6, p. 3792, 1985.

[5] J. von Pezold, A. Dick, M. Friák, and J. Neugebauer. Generation and performance of special quasirandom structures for studying the elastic properties of random alloys: Application to Al-Ti. *Physical Review B*, vol. 81, no. 9, p. 094203, 2010.

[6] W. L. Bragg and E. J. Williams. The effect of thermal agitation on atomic arrangement in alloys. *Proceedings of the Royal Society A: Mathematical,*

Physical and Engineering Sciences, vol. 145, no. 855, p. 699, 1934.

[7] E. Williams. The effect of thermal agitation on atomic arrangement in alloys. ii. *Proceedings of the Royal Society of London. Series A, Mathematical and Physical Sciences*, vol. 151, no. 874, p. 540, 1935.

[8] E. Williams. The effect of thermal agitation on atomic arrangement in alloys. iii. *Proceedings of the Royal Society of London. Series A, Mathematical and Physical Sciences*, vol. 152, no. 875, p. 231, 1935.

[9] D. de Fontaine, C. Wolverton, M. Asta, and G. Ceder. Prediction of ordered superstructure phase equilibria. *Journal of Phase Equilibria*, vol. 13, no. 4, p. 344, 1992.

[10] G. Ghosh, A. van de Walle, and M. Asta. First-principles calculations of the structural and thermodynamic properties of bcc, fcc and hcp solid solutions in the Al–TM (TM= Ti, Zr and Hf) systems: a comparison of cluster expansion and supercell methods. *Acta Materialia*, vol. 56, no. 13, p. 3202, 2008.

[11] A. van de Walle and G. Ceder. Automating first-principles phase diagram calculations. *Journal of Phase Equilibria*, vol. 23, no. 4, p. 348, 2002.

[12] M. P. Polak, P. Scharoch, and R. Kudrawiec. The electronic band structure of $Ge_{1-x}Sn_x$ in the full composition range: indirect, direct, and inverted gaps regimes, band offsets, and the Burstein–Moss effect. *Journal of Physics D: Applied Physics*, vol. 50, no. 19, p. 195103, 2017.

[13] J. W. D. Connolly and A. R. Williams. Density-functional theory applied to phase transformations in transition-metal alloys. *Physical Review B*, vol. 27, no. 8, p. 5169, 1983.

[14] A. van de Walle and G. Ceder. The effect of lattice vibrations on substitutional alloy thermodynamics. *Reviews of Modern Physics*, vol. 74, no. 1,

p. 11, 2002.

[15] E. Schrödinger. An undulatory theory of the mechanics of atoms and molecules. *Physical Review*, vol. 28, no. 6, p. 1049, 1926.

[16] W. Koch and M. C. Holthausen, *A Chemist's Guide to Density Functional Theory*. Weinheim: Wiley, 2001.

[17] M. Born and R. Oppenheimer. Zur quantentheorie der molekeln. *Annalen der Physik*, vol. 389, no. 20, p. 457, 1927.

[18] P. Hohenberg and W. Kohn. Inhomogeneous electron gas. *Physical Review*, vol. 136, p. B864, 1964.

[19] W. Kohn and L. J. Sham. Self-consistent equations including exchange and correlation effects. *Physical Review*, vol. 140, p. A1133, 1965.

[20] J. P. Perdew, R. G. Parr, M. Levy, and J. L. Balduz. Density-functional theory for fractional particle number: Derivative discontinuities of the energy. *Physical Review Letters*, vol. 49, p. 1691, 1982.

[21] F. Tran and P. Blaha. Accurate band gaps of semiconductors and insulators with a semilocal exchange-correlation potential. *Physical Review Letters*, vol. 102, no. 22, p. 226401, 2009.

[22] A. D. Becke and M. R. Roussel. Exchange holes in inhomogeneous systems: A coordinate-space model. *Physical Review A*, vol. 39, p. 3761, 1989.

[23] F. Tran, P. Blaha, and K. Schwarz. How close are the Slater and Becke–Roussel potentials in solids?. *Journal of Chemical Theory and Computation*, vol. 11, p. 4717, 2015.

[24] B. Cao, S. Chen, X. Jin, J. Liu, and T. Li. Short-range order in GeSn alloy. *ACS Applied Materials & Interfaces*, vol. 12, no. 51, pp. 57245–57253, 2020.

[25] T. D. Eales, I. P. Marko, S. Schulz, *et al.* $Ge_{1-x}Sn_x$ alloys: Consequences of band mixing effects for the evolution of the band gap γ-character with Sn concentration. *Scientific Reports*, vol. 9, no. 1, p. 1, 2019.

[26] E. J. O'Halloran, C. A. Broderick, D. S. P. Tanner, S. Schulz, and E. P. O'Reilly. Comparison of first principles and semi-empirical models of the structural and electronic properties of $Ge_{1-x}Sn_x$ alloys. *Optical and Quantum Electronics*, vol. 51, p. 314, 2019.

[27] S. Gupta, B. Magyari-Köpe, Y. Nishi, and K. C. Saraswat. Achieving direct band gap in germanium through integration of Sn alloying and external strain. *Journal of Applied Physics*, vol. 113, no. 7, p. 073707, 2013.

[28] R. Beeler, R. Roucka, A. V. G. Chizmeshya, J. Kouvetakis, and J. Menéndez. Nonlinear structure-composition relationships in the $Ge_{1-y}Sn_y$/Si(100) (y<0.15) system. *Physical Review B*, vol. 84, p. 035204, 2011.

[29] P. Moontragoon, Z. Ikonić, and P. Harrison. Band structure calculations of Si–Ge–Sn alloys: Achieving direct band gap materials. *Semiconductor Science and Technology*, vol. 22, no. 7, p. 742, 2007.

[30] A. Zunger, S.-H. Wei, L. G. Ferreira, and J. E. Bernard. Special quasirandom structures. *Physical Review Letters*, vol. 65, p. 353, 1990.

[31] A. van de Walle, P. Tiwary, M. De Jong, D. Olmsted, M. Asta, A. Dick, D. Shin, Y. Wang, L.-Q. Chen, and Z.-K. Liu. Efficient stochastic generation of special quasirandom structures. *Calphad*, vol. 42, p. 13, 2013.

[32] N. I. Levine, *Physical Chemistry*. New York: McGraw-Hill, 1995.

[33] A. van de Walle. Multicomponent multisublattice alloys, nonconfigurational entropy and other additions to the alloy theoretic automated toolkit. *Calphad*, vol. 33, p. 266, 2009.

[34] G. Bozzolo, R. D. Noebe, and P. B. Abel, *Applied computational materials modeling: theory, simulation and experiment*. New York: Springer Science & Business Media, 2007.

[35] A. van de Walle and G. Ceder. The effect of lattice vibrations on substitutional alloy thermodynamics. *Reviews of Modern Physics*, vol. 74, p. 11, 2002.

[36] B. Fultz. Vibrational thermodynamics of materials. *Progress in Materials Science*, vol. 55, p. 247, 2010.

[37] E. J. Wu, G. Ceder, and A. van de Walle. Using bond-length-dependent transferable force constants to predict vibrational entropies in Au-Cu, Au-Pd, and Cu-Pd alloys. *Physical Review B*, vol. 67, no. 13, p. 134103, 2003.

[38] B. P. Burton, A. van de Walle, and U. Kattner. First principles phase diagram calculations for the wurtzite-structure systems AlN–GaN, GaN–InN, and AlN–InN. *Journal of Applied Physics*, vol. 100, no. 11, p. 113528, 2006.

[39] A. van de Walle, M. Asta, and G. Ceder. The alloy theoretic automated toolkit: A user guide. *Calphad*, vol. 26, no. 4, p. 539, 2002.

[40] M. Bäker, "Calculating phase diagrams with ATAT." Unpublished, 2019.

[41] A. van de Walle and M. Asta. Self-driven lattice-model Monte Carlo simulations of alloy thermodynamic properties and phase diagrams. *Modelling and Simulation in Materials Science and Engineering*, vol. 10, p. 521, 2002.

[42] M. Virgilio, C. Manganelli, G. Grosso, G. Pizzi, and G. Capellini. Radiative recombination and optical gain spectra in biaxially strained n-type germanium. *Physical Review B*, vol. 87, no. 23, p. 235313, 2013.

[43] M. El Kurdi, G. Fishman, S. Sauvage, and P. Boucaud. Band structure and optical gain of tensile-strained germanium based on a 30 band k· p formalism.

Journal of Applied Physics, vol. 107, no. 1, p. 013710, 2010.

[44] A. Suzuki, O. Nakatsuka, S. Shibayama, M. Sakashita, W. Takeuchi, M. Kurosawa, and S. Zaima. Growth of ultrahigh-Sn-content $Ge_{1-x}Sn_x$ epitaxial layer and its impact on controlling Schottky barrier height of metal/Ge contact. *Japanese Journal of Applied Physics*, vol. 55, no. 4S, p. 04EB12, 2016.

[45] R. Farrow, D. Robertson, G. Williams, A. Cullis, G. Jones, I. Young, and P. Dennis. The growth of metastable, heteroepitaxial films of α-Sn by metal beam epitaxy. *Journal of Crystal Growth*, vol. 54, no. 3, p. 507, 1981.

[46] H. Höchst and I. Hernandez-Calderon. Angular resolved photoemission of InSb (001) and heteroepitaxial films of α-Sn (001). *Surface Science*, vol. 126, no. 1-3, p. 25, 1983.

[47] M. T. Asom, E. A. Fitzgerald, A. R. Kortan, B. Spear, and L. C. Kimerling. Epitaxial growth of metastable SnGe alloys. *Applied Physics Letters*, vol. 55, p. 578, 1989.

[48] P. John, T. Miller, and T.-C. Chiang. Core-level photoemission studies of the α-Sn/InSb (100) heterostructure system. *Physical Review B*, vol. 39, no. 5, p. 3223, 1989.

[49] R. C. Bowman, P. M. Adams, M. A. Engelhart, and H. Höchst. Structural characterization of α-Sn and α-$Sn_{1-x}Ge_x$ alloys grown by molecular beam epitaxy on CdTe and InSb. *Journal of Vacuum Science & Technology A: Vacuum, Surfaces, and Films*, vol. 8, p. 1577, 1990.

[50] J. Piao, R. Beresford, T. Licata, W. Wang, and H. Homma. Molecular-beam epitaxial growth of metastable Ge_{1-x} Sn_x alloys. *Journal of Vacuum Science & Technology B: Microelectronics Processing and Phenomena*, vol. 8, no. 2, p. 221, 1990.

[51] E. P. O'Reilly. Valence band engineering in strained-layer structures. *Semiconductor Science and Technology*, vol. 4, no. 3, p. 121, 1989.

[52] P. Voisin, Heterostructures of lattice mismatched semiconductors: fundamental aspects and device perspectives. in *Quantum Wells and Superlattices in Optoelectronic Devices and Integrated Optics*, vol. 861, p. 88, International Society for Optics and Photonics, 1988.

[53] S. Tomic and E. P. O'Reilly. Optimization of material parameters in 1.3-μm InGaAsN-GaAs lasers. *IEEE Photonics Technology Letters*, vol. 15, no. 1, p. 6, 2003.

[54] L. D. Landau, L. P. Pitaevskii, A. M. Kosevich, and E. Lifshitz, *Theory of Elasticity*. Oxford: Elsevier, 1986.

[55] J. van der Merwe. Structure of epitaxial crystal interfaces. *Surface Science*, vol. 31, p. 198, 1972.

[56] C. A. Broderick, S. Jin, I. P. Marko, *et al.* $GaAs_{1-x}$ Bi_x/GaN_yAs_{1-y} type-II quantum wells: novel strain-balanced heterostructures for GaAs-based near- and mid-infrared photonics. *Scientific reports*, vol. 7, p. 46371, 2017.

[57] R. D. Richards, F. Bastiman, J. S. Roberts, R. Beanland, D. Walker, and J. P. R. David. MBE grown GaAsBi/GaAs multiple quantum well structures: Structural and optical characterization. *Journal of Crystal Growth*, vol. 425, p. 237, 2015.

[58] C. G. Van de Walle. Band lineups and deformation potentials in the model-solid theory. *Physical Review B*, vol. 39, no. 3, p. 1871, 1989.

[59] A. Qteish and R. J. Needs. Improved model-solid-theory calculations for valence-band offsets at semiconductor-semiconductor interfaces. *Physical Review B*, vol. 45, p. 1317, 1992.

[60] M. P. C. M. Krijn. Heterojunction band offsets and effective masses in III-V quaternary alloys. *Semiconductor Science and Technology*, vol. 6, no. 1, p. 27, 1991.

[61] F. H. Pollak and M. Cardona. Piezo-electroreflectance in Ge, GaAs, and Si. *Physical Review*, vol. 172, p. 816, 1968.

[62] S. Tomić, A. G. Sunderland, and I. J. Bush. Parallel multi-band k · p code for electronic structure of zinc blend semiconductor quantum dots. *Journals of Materials Chemistry*, vol. 16, no. 20, p. 1963, 2006.

[63] H. S. Nalwa, *Handbook of Thin Films, Five-Volume Set*, vol. 5. Cambridge: Elsevier, 2001.

[64] E. Kasper and D. J. Paul, *Silicon quantum integrated circuits: silicon-germanium heterostructure devices: basics and realisations.* Heidelberg: Springer Science & Business Media, 2005.

Chapter 3

Elemental germanium and tin crystals

3.1 Introduction

To study the electronic and thermodynamic properties of $Ge_{1-x}Sn_x$ alloys, the constituent components of the alloy must first be analysed. The structural and electronic parameters of the pure crystals are of interest as they give a reference point relative to the behaviour of the alloy systems. An alloy is expected to act somewhat intermediary to the two components, though properties do not always interpolate linearly between the properties of the alloy's elemental constituents. An example of this is when bowing is present for the band gap energy as a function of alloy composition. Germanium (Ge) and tin (Sn) are well studied experimentally, and this allows for a direct comparison to parameters calculated in this work. This allows for a preliminary assessment of the methodologies used in analysing the $Ge_{1-x}Sn_x$ alloy to be considered in later chapters.

Density functional theory (DFT) with the local density approximation (LDA), as presented in chapter 2, is employed to obtain the structural properties and

relaxed atomic coordinates for determination of geometries for the simulation cells. The LDA calculations allow the lattice parameters and elastic constants of the materials to be obtained. The critical thicknesses of the materials are then calculated from these parameters, which give an estimation of the reachable thicknesses of films in the presence of external strain. The modified Becke Johnson (MBJ) meta-GGA functional is implemented for electronic structure calculations using the DFT/LDA relaxed cells, allowing for the extraction of band gaps and effective masses. By applying strain to the simulation cells, the deformation potentials can also be extracted from the band structures.

The band gaps, deformation potentials, and elastic constants are then combined using deformation potential theory (DPT), which allows for a prediction of how the band gaps of the materials will behave under strain. This allows for a comparison to the DFT/LDA results, which can be obtained from simple calculations on the primitive cells. DPT is also utilized in later chapters to investigate the effect of band mixing on the alloy and structures.

Sections of this chapter have been submitted for publication [1] or have been published [2].

3.2 Structural properties

3.2.1 Computational details

DFT, as described in chapter 2, within the usual Kohn-Sham framework is employed in an implementation using norm-conserving pseudopotentials and linear combination of numerical atomic orbitals (NAO) basis sets [3–7] for the determination of simulation cell geometries. For germanium, a s4p4d3f2 basis set is employed, where the notation indicates the number of s,p,d and f type orbitals

centered about atoms of a given species. The pseudopotential includes the four $4s^2$, and $4p^2$ valence electrons. For tin, a s2p3d3f2 basis set is utilized, including the fourteen $4d^{10}$, $5s^2$, and $5p^2$ electrons. Brillouin zone integrations are performed over a grid generated according to the Monkhorst-Pack [8] scheme, maintaining a density of at least 7 k-points/$Å^{-1}$, whilst real-space quantities are discretized on a grid with a corresponding energy cut-off of at least 100 Hartree. The convergences of these parmeters as calculated from the primitive cells of Ge and α-Sn are shown in fig. 3.1. The LDA presented in chapter 2 was employed for the exchange-correlation potential in all geometry optimisation calculations [9]. This method is shown to accurately calculate the structural properties of both germanium and tin, and these are compared to experimental values in the following sections. Including spin-orbit interactions in our simulations was found to have a negligible effect on the geometry for these systems, consistent with the findings of another recent study on these materials [10], and has thus been neglected for structural relaxations. Structural relaxations are performed on all simulated structures until forces acting on atoms are below 5×10^{-2} eV/Å and all stress tensor elements are below 0.1 GPa.

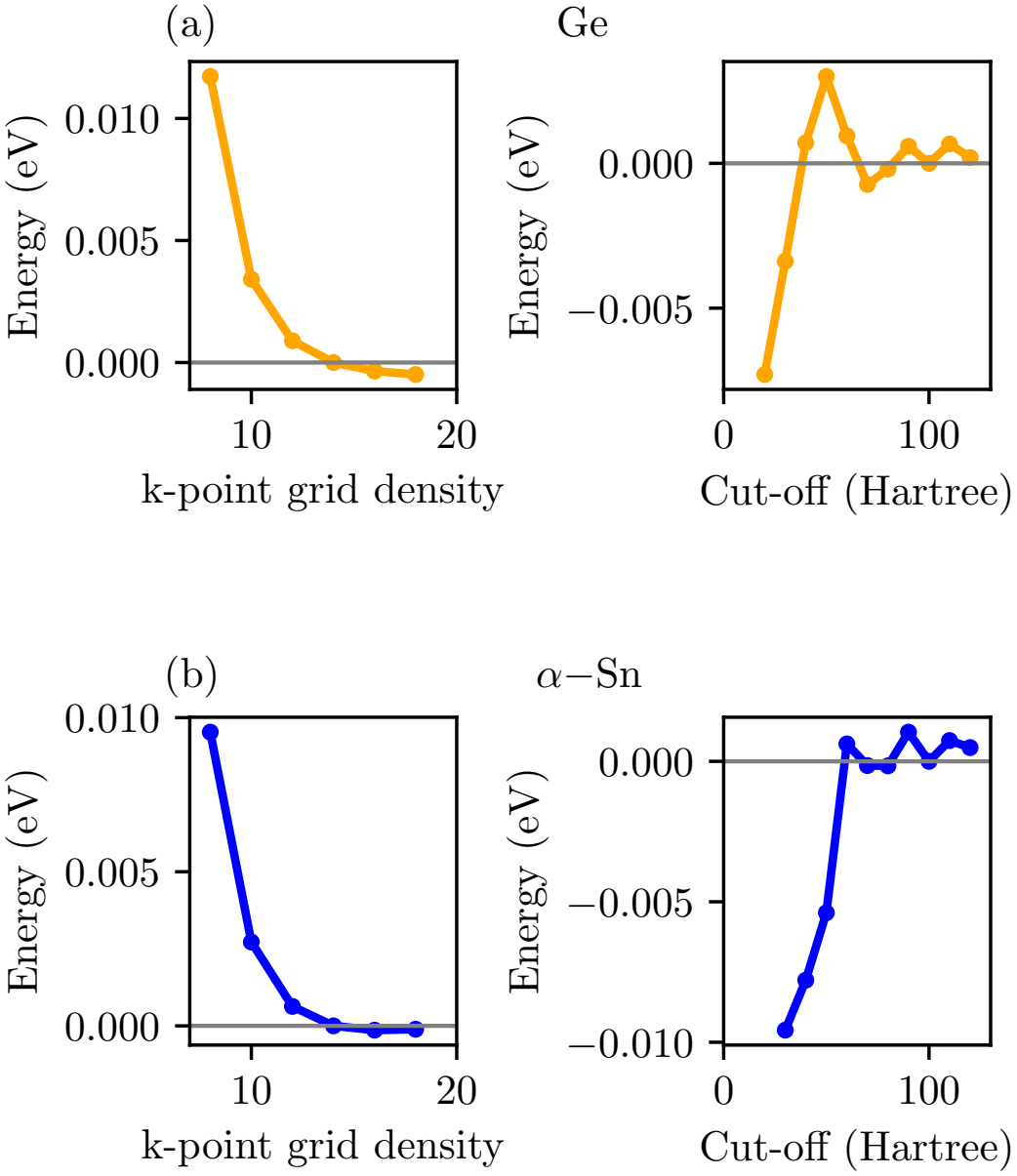

Figure 3.1: Convergences of the k-point grid density and energy cut-off for the primitive cell of (a) germanium and (b)α-tin. The zero of each graph is the converged value that has been employed in the calculations.

3.2.2 Lattice parameters and elastic constants

The lattice constant of a material is a fundamental parameter when analyzing structural and electronic properties. The LDA has been shown to slightly underestimate the lattice parameter of materials relative to other functionals (such as

the generalized gradient approximation), which tend to overestimate lattice parameters [11]. The lattice constants of tin and germanium's diamond structures that have been computed within the LDA approach are shown in table 3.1. These equilibrium lattice parameters show agreement with previous calculations in the literature, as well as agreeing with experimentally reported values to within 1%. The lattice constant is one of the fundamental properties of crystalline materials, and its accurate determination is required for predicting subsequent electronic, mechanical and, thermodynamic properties.

Table 3.1: Calculated equilibrium lattice constants (a_0); c_{11}, c_{12}, and c_{44} elastic constants; and bulk moduli (B_0) of germanium and α-tin, as calculated in the DFT/LDA model, compared to previous theoretical calculations as well as experimental values.

Ge	This work (DFT/LDA)	Theory	Experiment
a_0 (Å)	5.64	5.646 [12]	5.657 [13]
c_{11} (GPa)	122.96	122 [10], 142.5 [14]	128.53 [15], 128.9 [16]
c_{12} (GPa)	49.75	47 [10], 58.5 [14]	48.25 [15], 48.3 [16]
c_{44} (GPa)	60.83	86 [10], 58.7 [14]	66.8 [15],67.1 [16]
B_0 (GPa)	74.15	72 [10], 86.5 [14]	75.8 [17], 75.01 [15]
Sn			
a_0 (GPa)	6.47	6.49 [12]	6.489 [18, 19]
c_{11}(GPa)	68.27	68 [10], 72.53 [14]	
c_{12}(GPa)	36.59	34 [10], 29.73 [14]	
c_{44}(GPa)	28.98	53 [10], 29.9 [14]	
B_0 (GPa)	47.16	45.33 [10], 44 [14]	42.5 – 53.1 [20, 21]

When straining a material, the elastic constants (C_{ij}) paramaterize how a material reacts to an applied strain. These are computed by analyzing the internal stress vectors of two atom unit cells as external strains are applied in the form

of slight deformations to the structures [6]. Results from these calculations are presented in table 3.1. The elastic constants calculated in this work are shown to be in reasonable agreement with both previous theoretical work as well as experimental measurements, as referenced within the table.

The bulk modulus (B_0) of a cubic material is related to the elastic constants by $B_0 = (C_{11} + 2C_{12})/3$. The bulk modulus, also given in table 3.1, as computed for germanium exhibits a deviation of less than 3% with respect to experimentally reported values obtained via ultrasound. The bulk modulus of tin's α phase, is shown to lie within previously reported values obtained by fitting of neutron scattering data. Both of the predicted bulk moduli calculated within this work are consistent with previous theoretical work.

Structural parameters for both alloy components are thus reasonably represented in our LDA approach. This is important as inaccurate elastic constants lead to strain affecting the material in unrealistic ways, introducing error into the structures, and in turn, the electronic structures. Previous theoretical work has shown that the alloy elastic constants are intermediary to those of the alloy components, with some reporting non-negligible bowing [10, 22]. In later chapters the alloy elastic constants are calculated in a similar manner as the elemental components, however special quasirandom structures (SQSs), as discussed in chapter 2, are used in place of two atom primitive cells.

3.2.3 Strain direction

In this work, the effects of strain are modelled by biaxially straining the 64 atom SQS cells and allowing out of plane relaxation. As the simulation cells are periodic in all three directions, the application of this epitaxial strain is likened to a thick strained layer grown on a substrate. The simulation cells are biaxially strained to a *substrate lattice parameter*, and relaxation is allowed away from the

surface. Surface effects are therefore ignored, implying relaxation of a thin film in which the surface/substrate interface energies are small relative to the bulk-like component of the film.

In order to determine along which crystallographic plane to simulate growth we compute the *epitaxial softening function* of both germanium and tin as:

$$q(a_S, \hat{G}) = \frac{\Delta E^{epi}(a_S, \hat{G})}{\Delta E^{bulk}(a_S)}, \tag{3.1}$$

which is the ratio between the increase in energy due to biaxial strain as a result of epitaxial growth along a direction $\hat{G}$ on a substrate with lattice constant a_S, and the increase in energy due to hydrostatically straining to the substrate lattice constant a_S. This dimensionless parameter quantifies the degree of out-of-plane relaxation exhibited by a material that is grown epitaxially; it is desirable to minimize $q(a_S, \hat{G})$ (and thus $\Delta E^{epi}(a_S, \hat{G})$) for a given substrate in order to avoid or reduce dislocations and other strain-induced film/surface defects [23]. Figure 3.2 shows the epitaxial softening functions of germanium and tin as computed with DFT. We exclude data about the equilibrium lattice parameters as in a previous study [23]. This is done as the differences in energy between $\Delta E^{epi}(a_S$ and $\Delta E^{bulk}(a_S)$ are too small, and as such the values for $q(a_S, \hat{G})$ contain a lot of noise. The values for the epitaxial softening functions at zero strain are calculated from harmonic continuum elasticity theory with the formula [23]:

$$q_{harm}, (\hat{G}) = 1 - \frac{B}{C_{11} + \Delta\gamma_{harm}(\hat{G})}, \tag{3.2}$$

where B and C_{11} are as before, respectively, the bulk modulus and the elastic constant. The elastic anisotropy parameter, $\Delta = C_{44} - \frac{1}{2}(C_{11} - C_{12})$. $\gamma_{harm}(\hat{G})$ is a geometric function of the spherical angles formed by $\hat{G}$ and are given for the principle growth directions as $q_{harm}(\langle 100 \rangle) = 0$, $q_{harm}(\langle 110 \rangle) = 1$ and $q_{harm}(\langle 111 \rangle) = \frac{4}{3}$ [24].

The open green circle in the figure are the epitaxial softening functions for the ⟨100⟩ growth directions as calculated from continuum elastic theory (CET) using eq. (2.40), eq. (2.41), eq. (2.42) and eq. (2.36). This is done for only the ⟨100⟩ growth direction as the off diagonal components of the strain tensor are not zero in the ⟨110⟩ and ⟨111⟩ directions. Without knowledge of these the elastic energy cannot be calculated. The CET values obtained for the ⟨100⟩ do show good agreement with the DFT data, particularly at low strains. However, they deviate for high strains, due to anharmonic effects not captured by CET.

The ⟨100⟩ direction is observed to be the *softest* direction for both constituents about their equilibrium lattice constants. This conclusion is retained at all compositions if the alloy epitaxial softening function is estimated as a weighted sum of the elemental softening functions. This suggests that ⟨100⟩-oriented films will tend to minimise internal strain energy, and thus structural defects for epitaxially coherent $Ge_{1-x}Sn_x$ films, and is consistent with at least one experimental analysis [25]. However, it is of note that in this study the strain relaxation values were calculated at different compositions for different film orientations, and as such it is difficult to compare between orientations.

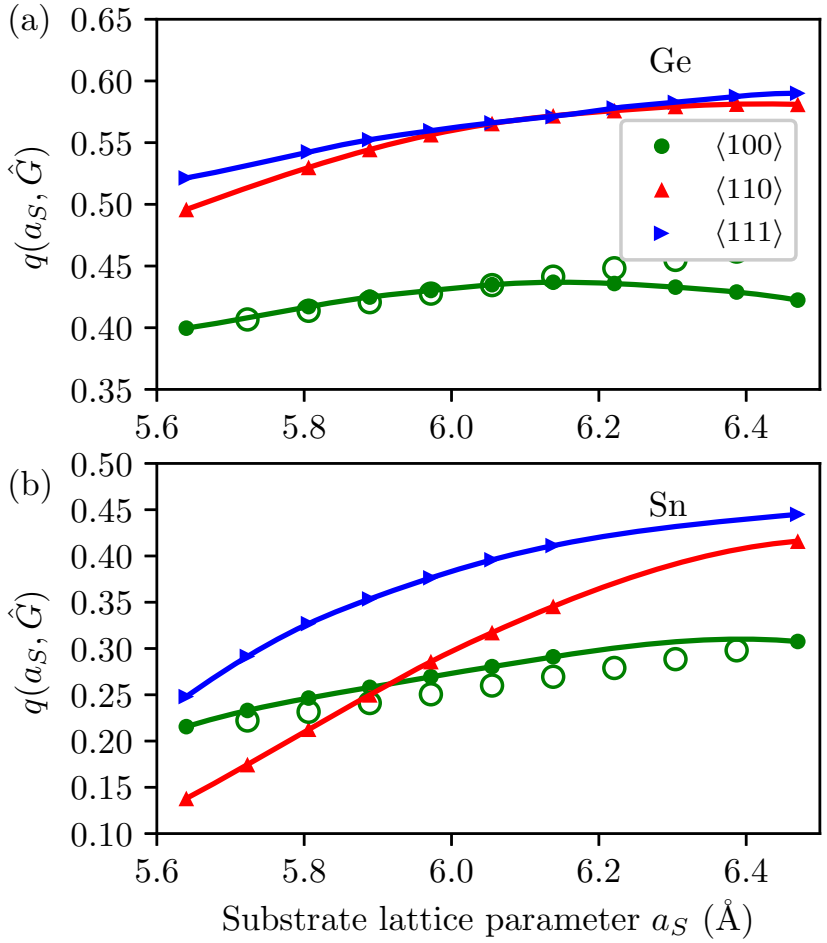

Figure 3.2: Epitaxial softening functions for (a) Ge with an equilibrium lattice constant (a_{lat}) of 5.64 Å, and (b) Sn with an a_{lat} of 6.47 Å, as computed employing DFT simulations. The empty green circles indicate the epitaxial softening functions obtained through CET for the 100 direction.

3.2.4 Strain induced growth limitations

The calculated lattice parameters and elastic constants can be used in a critical thickness model [26] to estimate the thickness limit of a material. The critical thickness of a film is the thickness above which dislocations induced by the applied epitaxial strain are energetically preferred to a crystalline structure [26], as described in section 2.5.1. If strain is to be employed in the fabrication of semimetallic $Ge_{1-x}Sn_x$ alloys, this can be an important factor. If the critical thickness is below the thickness at which quantum confinement begins to take

effect, then a semimetallic structure cannot be fabricated without dislocations present. Films with thicknesses below the critical thickness would have confinement induced band gaps.

The critical thicknesses for Ge and α-Sn are presented in Fig. 3.3, as a function of lattice parameter. When strained, tin allows for slightly larger reachable thicknesses than germanium due to softer elastic constants. This results in a marginally broader peak on the critical thickness graph. Care must be taken when considering what magnitudes of strain to apply, as the achievable thickness reduces drastically as small amounts of strain are added; a 1% strain on these materials leads to a critical thickness of between 23 nm and 27 nm. This does not allow for large magnitudes of strain to be used in the fabrication of semimetallic films, as sufficiently large strains would lower the critical thickness to a point where only structures which have band gaps induced by quantum confinement could be fabricated.

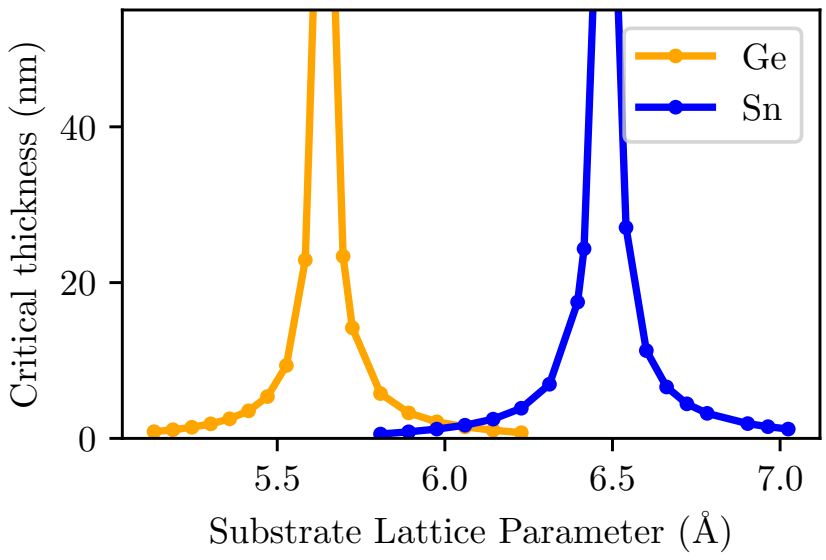

Figure 3.3: Critical thicknesses of Ge (a_0 = 5.64 Å) and α-Sn (a_0 = 6.47 Å) as a function of substrate lattice parameter.

3.3 Electronic properties

In this section the electronic properties of the pure alloy constituents are assessed. Of particular interest are their band gaps, which are calculated within the DFT/mBJ method described in chapter 2 and used in later chapters to calculate alloy band gaps. As well as examining band gaps, parameters such as the deformation potentials and the effective masses are also calculated and compared to experimental and previous theoretical studies. These allow for estimates as to how the band gaps of the materials behave when strain and confinement, respectively, are introduced. The deformation potentials are used within deformation potential theory as a means of estimating the effect of strain on the band gap of Ge and α-Sn. The effective masses provide a way of estimating the shifts of the bands as the material is confined, however this is dependent on the quality of the effective masses extracted from the band structures.

3.3.1 Computational Details

DFT is also used to study the electronic properties of $Ge_{1-x}Sn_x$ alloys. The cells used are those that were relaxed in the previous section, however, mBJ meta-GGA [27] is employed when calculating the electronic structure of the alloys. The same cutoffs and pseudopotentials as used in the LDA calculations for structure determination are applied to these band structure calculations, however spin-orbit interactions are included. The c-parameter for the meta-GGA functional employed in these simulations has been determined to be c_{Ge}=1.1 for Ge, and c_{Sn}=1.225 for α-tin, as the results in the following section indicate that these accurately reproduce the electronic band structure of these materials.

3.3.2 Electronic structures

Figure 3.4 shows the calculated electronic band structure of germanium and α-tin as calculated within the meta-GGA approach. The predicted germanium band structure displays energy separations between the Γ_8^+ state and the L and Γ_7^- states that show good agreement with the indicated experimental results [28]. The calculated α-tin band structure exhibits a Γ_7^- and Γ_8^+ separation, referred to as the *negative gap*, between the values obtained from experiment [29, 30]. The energy differences of both materials show good agreement compared with both previously calculated energy differences, as well as experimental results, presented in table 3.2.

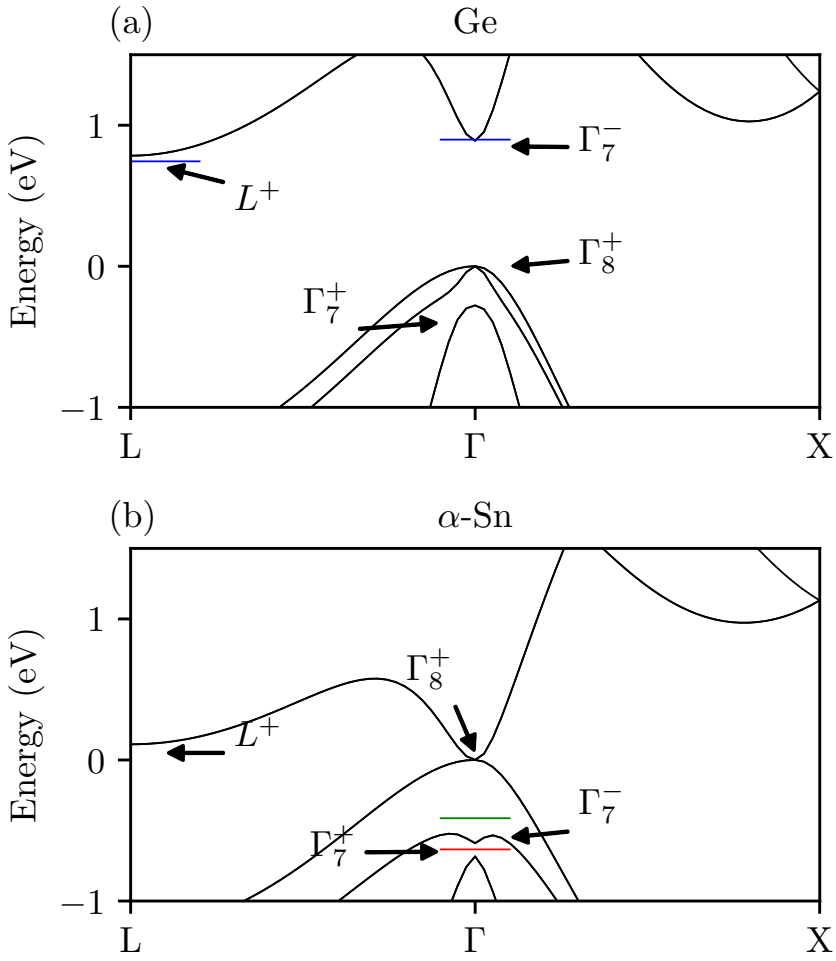

Figure 3.4: Band structures of (a) germanium and (b) α-tin, calculated within the meta-GGA/DFT model. Experimental results are indicated with blue [28], green [29], and red [30] bars.

Table 3.2: Calculated Γ_7^- - Γ_8^+ and L - Γ_{8v} energy differences of Ge and the Γ_7^- - Γ_8^+ energy difference of α-Sn. All values are in units of eV.

Ge	this work	theory	experiment
Γ_7^- - Γ_8^+	0.89	0.879 [31], 0.892 [32]	0.898 [28]
L - Γ_{8v}	0.784	0.71 [31], 0.744 [32]	0.744 [28]
Sn			
Γ_7^- - Γ_8^+	−0.589	−0.39 [31], −0.408 [32]	-0.413 [30], −0.634 [29]
		−0.64 [33]	

3.3.3 Confinement effects on the band gap

As explained in chapter 1, confinement effects allow for an opening of the band gap in semimetallic materials. It is important to understand how the bands shift as a result of confinement in order to understand which bulk alloy compositions are suited for use in semimetallic electronic device designs.

The magnitude of the shift of an energy level can be estimated from the effective mass. By likening the system to a quantum well, the energy of the confined band can be estimated as:

$$E_n = E_0 + \frac{\hbar^2 k^2}{2m^*}, \tag{3.3}$$

where m^* is the effective mass and $k = \frac{\pi n}{l}$, where l is the width of the well, or in this case, the thickness of the structure [34].

The effective masses can be obtained by fitting the band minimum or maximum to a parabola and solving the equation [35]:

$$m* = \hbar^2 \left[\frac{d^2 E}{dk^2} \right]^{-1}. \tag{3.4}$$

The effective masses obtained from the mBJ band structures are presented in table 3.3. While the germanium effective masses show good agreement with previously calculated mBJ effective masses, they are not as accurate as many of the HSE hybrid calculations when compared to experiment. This is to be expected, as mBJ meta-GGA has previously been shown to exhibit as much as 20% error when calculating effective masses on III-V semiconductors [36]. The α-tin effective masses show a large deviation from experiment, which is likely due to the complicated band structure exhibited by the material, displaying a so-called "inverted band structure" caused by the Γ_7^- state being lower in energy than the Γ_8^+ states, causing the light electron (LE) band to change direction of curvature [29, 37, 38]. The complexity of the α-tin band structure indicates that

a simple approximation, such as the one given in eq. (3.3), is not sufficient to predict the shifts of the bands as a result of confinement.

While this model is not sufficient for predicting the band structure of alloy compositions where the Γ_7^- is lower in energy than the Γ_8^+ states, it does help illustrate how the band gap evolves at low thicknesses. This is illustrated in fig. 3.5 for a theoretical material that in bulk has a zero band gap, but has the m*$[\Gamma_{8\mathrm{HH}}^+]$ and m*$[\Gamma_7^+]$ of pure germanium. This shows that as the thickness of the film decreases below 5 nm, the band gap increases rapidly, which has also previously been shown for α-tin nanowires [39].

However, $Ge_{1-x}Sn_x$ alloys are not expected to have these Ge like effective masses over the full composition range, as the addition of Sn changes the band structure. From the four band $\mathbf{k}\cdot\mathbf{p}$ model with zero spin orbit splitting, it can be observed that m*$[\Gamma_7^+]$ varies approximately linearly with band gap [40]. As the addition of Sn reduces the band gap of the alloy, so too will the effective masses be reduced. As such, at narrower band gaps, m*$[\Gamma_7^+]$ will be lower than that of pure Ge, leading to confinement having a magnified effect on these alloys. As such, for zero band gap $Ge_{1-x}Sn_x$ alloys, it would be expected that a band gap would open up at larger thicknesses compared to the example given in fig. 3.5.

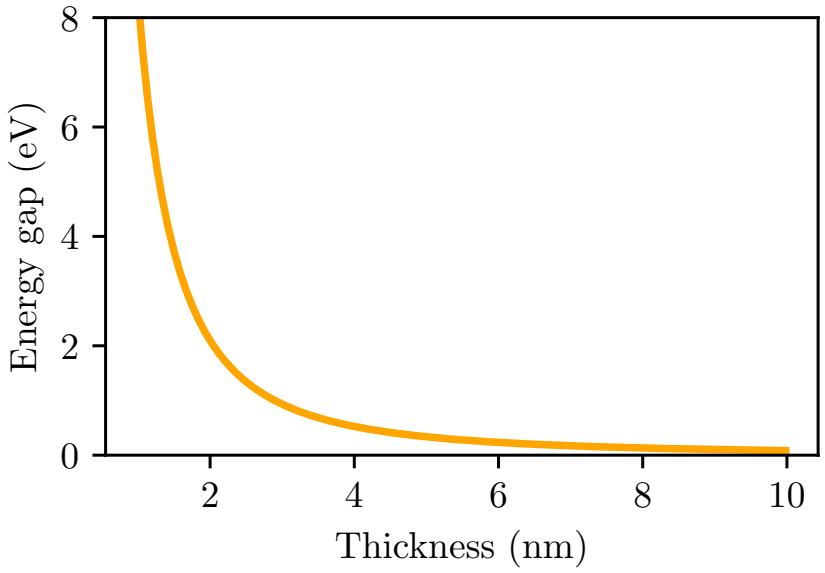

Figure 3.5: Band gap vs thickness for a theoretical material that has the $m^*[\Gamma^+_{8HH}]$ and $m^*[\Gamma^+_7]$ of pure Germanium and a zero band gap as calculated using eq. (3.3).

However, to gain a detailed understanding of how confinement affects the more complex band structure of α-tin, *ab initio* calculations are required. Of particular interest is the Γ^-_7 state. Calculations of Sn nanocrystals have shown that this state increases in energy as the material is confined [41]. This has been further confirmed through calculation of an orbital resolved band structure for a hydrogen terminated α-tin film. This film is displayed in fig. 3.6, which represents a twelve atom simulation cell periodic in the x- and y-directions (with the z-direction normal to the surface).

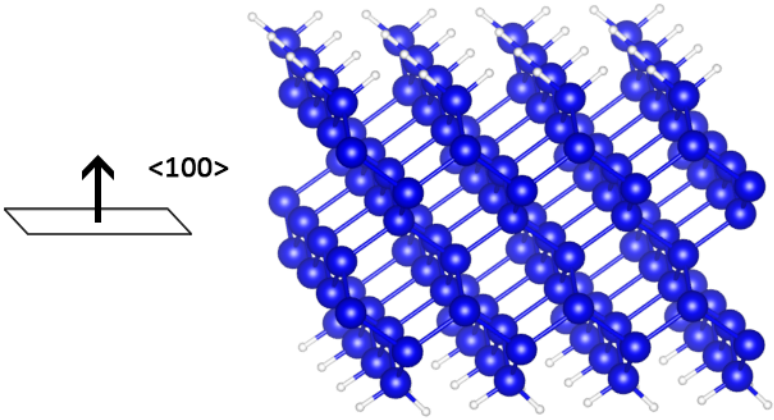

Figure 3.6: 1.3 nm thick, thin film, confined in the [001] direction. The white atoms represent hydrogen, and the blue atoms represent tin.

The projected density of states (PDOS) of this film is presented in fig. 3.7. This demonstrates the conduction band in the film comprising of mainly s-type states, associated with the Γ_7^- state in group IV materials, including α-tin [42]. The valence band displays none of this character, indicating that the Γ_7^- state has risen in energy.

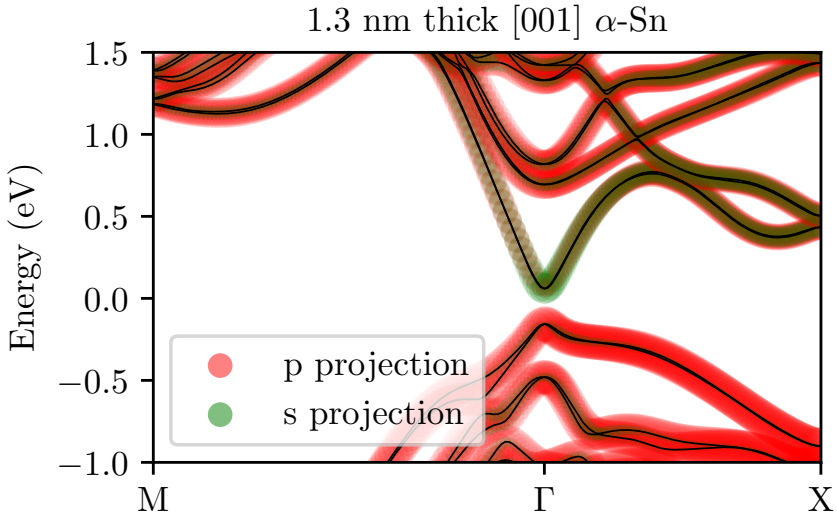

Figure 3.7: Orbital resolved band structure of a 1.3 nm thick, hydrogen terminated α-tin thin film, confined in the [001] direction.

The magnitude of the shift of the Γ_7^- state is of course dependent on direction and magnitude of confinement [34]. It is possible through confinement in other directions that this state remains part of the valence band. However, as shown in fig. 3.7, it can play an important factor in deciding the band gap of confined structures, and as such, should be taken into account when analyzing the electronic structures of alloys for use in semimetallic devices.

Table 3.3: Calculated effective masses (m*); deformation potentials of the Γ_7^- - Γ_8^+ energy difference ($a_{\Gamma diff}$); the L - Γ_{8v} gap (a_{Ldiff}); and the splitting parameters of the valence band due to uniaxial strain, shear strain, and spin-orbit effects (b, d, and Δ_0 respectively) of the Ge and α-Sn band structures. All effective masses are given in units of the electron rest mass (m_e), and all other are given in units of electron volt (eV).

Ge	This work (DFT/LDA)	Theory	Experiment
$m^*[\Gamma_7^-]$	0.056	0.034, 0.047 [43]	0.037 [44]
$m^*[\Gamma_{8HH}^+]$	0.226	0.203, 0.233 [43]	0.28 [44]
$m^*[\Gamma_{8LH}^+]$	0.058	0.043, 0.059 [43]	0.0438 [44]
$m^*[\Gamma_7^+]$	0.096	0.097, 0.122 [43]	0.095 [44]
$a_{\Gamma diff}$	-9.54	-8.6 [44]	
a_{Ldiff}	-3.36	-2.78 [45]	
b	-2.78	-2.66 [33], -2.16 [46]	-2.2 [44]
d	-5.95	6.06 [46]	
Δ_0	0.28	0.27 [43], 0.3 [33]	0.296 [44]
Sn			
$m^*[\Gamma_7^-]$	0.032		0.058 [44]
$m^*[\Gamma_{8HH}^+]$	0.508		0.21 [44]
$m^*[\Gamma_{8LE}^+]$	0.074		0.0233 [44]
$m^*[\Gamma_7^+]$	0.033	0.041 [44]	
$a_{\Gamma diff}$	-6.68	-9.1 [44], -6.97 [47]	
a_{Ldiff}	-1.53		
b	-2.39	-2.31 [33]	
d	-5.23	-4.1 [48]	
Δ_0	0.68	0.8 [33]	0.8 [29]

3.3.4 Predicting band shifts due to strain

Strain offers, in addition to quantum confinement, another parameter which can be used to adjust band gap energies. The deformation potentials allow for an efficient way of estimating how the electronic band structure of a material acts under small strains. These are extracted from DFT, by applying strains of 1% and -1% to the materials and measuring the energy shifts for idividual energy bands. Hydrostatic strains allows for the extraction of the a deformation potentials, while uniaxial and sheer strains allow for the extraction of b and d, respectively. The deformation potentials calculated within the meta-GGA XC functional are presented in table 3.3. Where possible in Table 3.3, the results of our DFT calculations are compared to experimental measurements. Our TB-mBJ-calculated direct and indirect band gaps are in good quantitative agreement with previous calculations and with low-temperature experimental measurements. For the hydrostatic, axial and shear deformation potentials, little experimental data are available. Here, to evaluate the accuracy of our calculated hydrostatic deformation potentials a_g, it is noted that the corresponding measurable band gap pressure coefficient $\frac{dE_g}{dP}$ is given by $\frac{dE_g}{dP} = -\frac{a_g}{B_0}$ [47]. Using the values from table 3.3 and table 3.1, $\frac{dE_g}{dP}$ = 12.87 and 4.53 meV kbar^{-1} are computed respectively for the pressure coefficients associated with the direct Γ_7^--Γ_8^+ and indirect (fundamental) L_6^+-Γ_8^+ band gaps of Ge. These values are in excellent quantitative agreement with the quoted values of 12.9 and 4.3 meV kbar^{-1} for Ge [49], as well as with previous experimental measurements [50–52] and theoretical calculations [47]. To apply the deformation potentials to the calculation of band gaps under strain, DPT is applied [45] as described in section 2.5.2.

The results of the DPT calculations are summarised in fig. 3.8(a) and 3.8(b), respectively. In each case, closed green circles show the TB-mBJ DFT-calculated direct Γ_7^--Γ_8^+ energy gap, calculated as a function of in-plane strain ϵ_{xx}, with in-

plane strain values < 0 (> 0) corresponding to compressive (tensile) strain. Closed red circles in fig. 3.8(a) and fig. 3.8(b) show the TB-mBJ DFT-calculated indirect L_6^+-Γ_8^+ energy gap. The green and red lines in fig. 3.8(a) and fig. 3.8(b), respectively, show the corresponding energy gaps calculated by DPT as described in section 2.5.2, using the parameters listed in tables 3.1,3.2, and 3.3. Solid and dashed lines respectively show the band gaps calculated with respect to HH- and LH-like Γ_8^+ VB states, where $E_{\mathrm{HH}} > E_{\mathrm{LH}}$ for $\epsilon_{xx} < 0$ (and vice versa), so that solid (dashed) lines represent the direct Γ_7^- and indirect L_6^+ band gaps involving HH- (LH-) like Γ_8^+ VB edge states in the compressive (tensile) strained regime. Closed blue triangles in fig. 3.8(a) show experimental measurements of the direct band gap of tensile-strained Ge epitaxial layers. [53] Then, good quantative agreement is noted in fig. 3.8(a) and fig. 3.8(b) between the full DFT and deformation potential theory calculations, reflecting the accuracy of our DFT-calculated elastic constants and deformation potentials. The increased deviation between the DFT-calculated and deformation potential theory results at high compressive strain in Ge is attributed to increasing non-linear strain contributions, which are not captured by DPT. The experimental measurements of the Ge direct band gap of Ref. [53] were performed at room temperature. In order to compare these data to our zero-temperature DFT calculations, the experimental data are rigidly shifted so that the measured and calculated direct band gaps coincide at zero strain. Good quantitative agreement is observed between theory and experiment, with our DFT-based deformation potential theory calculations quantitatively describing the tensile strain-induced reduction of the direct band gap.

Beginning with Ge, our calculations predict that pseudomorphic tensile strain can produce an indirect L_6^+-Γ_8^+ to direct Γ_7^--Γ_8^+ band gap transition, highlighted by the crossing of the dashed red and green lines in fig. 3.8, for in-plane tensile strain $\epsilon_{xx} \approx 1.4\%$. This transition is mostly driven by a downward shift of the Γ_7^- zone-centre CB edge energy due to the hydrostatic component of the pseudo-

morphic tensile strain, with an upward shift in energy of the LH-like Γ_8^+ VB edge states due to the biaxial component of the pseudomorphic tensile strain further reducing the band gap. This is in line with previous predictions [12, 54, 55] of an indirect- to direct-gap transition for $\epsilon_{xx} \approx 1.5\%$ and 1.9%. For larger tensile strains, further narrowing of the direct band gap is observed, and it is expected that a semiconducting to semimetallic transition can be achieved for tensile strain $\epsilon_{xx} \approx 4.4\%$. Under compressive strain an increase (decrease) of the direct Γ_7^--Γ_8^+ (indirect L_6^+-Γ_8^+) band gap is computed. Here, emphasis is placed on the fact that Ge under applied pseudomorphic strain is considered. Under purely hydrostatic applied compression it would be expected that both the direct and indirect band gaps increase in magnitude, as reflected by the negative values of the associated band gap hydrostatic deformation potentials (cf. table 3.3). Here, under compressive pseudomorphic strain, the upward energy shift of the HH-like Γ_8^+ VB edge states is faster than the upward energy shift of the L_6^+ CB edge states, leading to a net reduction of the indirect band gap.

Considering our calculated results for α-Sn in fig. 3.8(b), qualitatively similar behaviour is observed, as well as good quantitative agreement between the TB-mBJ DFT and deformation potential theory-calculated strain-dependent band gaps. However, while it would be expected that it should be possible to open up the inverted (negative) Γ_7^--Γ_8^+ energy gap under applied hydrostatic pressure, the splitting of the HH- and LH-like Γ_8^+ states in the presence of pseudomorphic strain prevents this. Specifically, it is observed that the biaxial component of the pseudomorphic strain pushes the HH-like Γ_8^+ states higher in energy at a rate which is approximately equal to the upward energy shift of the Γ_7^- states, due to the hydrostatic component of the strain. As such, the computed inverted direct band gap in fig. 3.8(b) remains approximately constant as a function of compressive in-plane strain (closed green circles and solid green line). Therefore, our TB-mBJ DFT calculations suggest that while it is in principle possible to drive a

semiconducting to semimetallic transition in highly tensile strained pseudomorphic Ge, it is not possible to achieve a semimetallic to semiconducting transition at realistic strains in pseudomorphic α-Sn bulk-like epitaxial layers.

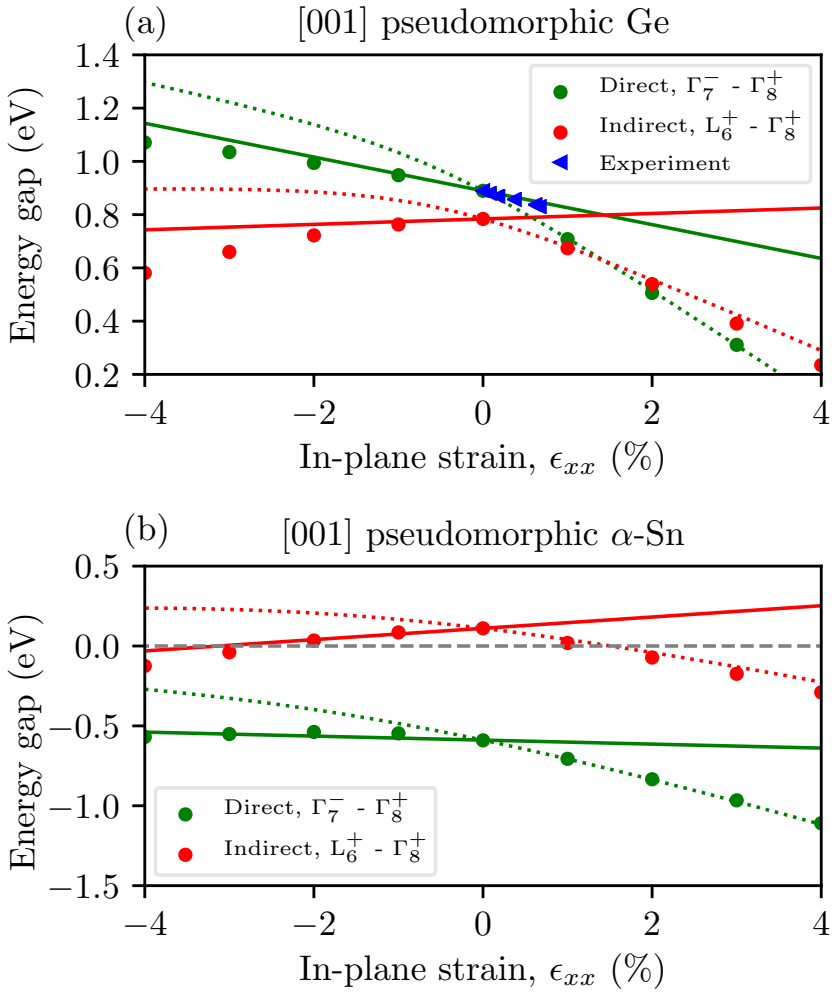

Figure 3.8: (a) meta-GGA DFT-calculated indirect (fundamental L_6^+-Γ_8^+; closed red circles) and direct (Γ_7^--Γ_8^+; closed green circles) band gaps, as a function of in-plane strain (lattice mismatch), $\epsilon_{xx} = \frac{a_S - a_L}{a_L}$, in pseudomorphically strained Ge. Solid and dashed lines represent band gaps calculated via deformation potential theory, as described in section 2.5.2 in conjunction with the data of tables 3.1,3.2, and 3.3. Solid (dashed) green lines indicate the direct band gap between Γ_7^- CB and HH- (LH-) like Γ_8^+ VB states. Solid (dashed) red lines indicate the indirect band gap between L_6^+ CB and HH- (LH-) like Γ_8^+ VB states. Closed blue triangles denote room-temperature experimental measurements [53]. (b) Same data as (a), calculated for α-Sn.

3.4 Conclusions

In this chapter, DFT-LDA calculations are performed on unit cells of elemental germanium and α-Sn for geometry optimisation as well as to obtain lattice parameters and elastic constants. These parameters show good agreement with previous theoretical and experimental values. By applying the structural properties to the critical thickness model, growth limits are calculated, with a 1% strain lowering the achievable thicknesses to approximately between 24 nm and 27 nm for both materials in the $\langle 100 \rangle$ direction. This is found to minimise internal strain energy brought about by biaxial strain through calculation of the epitaxial softening functions of the two materials.

The electronic properties are also shown to be in agreement with previous work, and as such verify the meta-GGA approach in calculating the electronic properties for these materials. By combining the structural and electronic properties using DPT, a computationally efficient model is achieved which can predict how the bands of germanium and α-tin behave under strain. This has been shown to agree with the meta-GGA calculations of the band gap at strains as high as 4%.

DFT calculations indicate that the Γ_7^- - Γ_8^+ energy difference of bulk α-tin can be an important factor in the resultant band gap when the material is confined. DPT and DFT demonstrate that this energy difference is mostly unaffected by compressive strain and increased by tensile strain. As α-tin's stability relative to β-tin has been shown to increase as a function of cell volume [56], tensile strain offers a means of increasing the Γ_7^- - Γ_8^+ overlap in bulk α-tin, therefore decreasing the band gap in confined structures, dependent on confinement direction. In section 5.4 it will be shown that small amounts of Ge have little impact on the negative band gap of relaxed bulk α-Sn. As such the required tensile strain could be applied by adding small amounts of Ge to an α-Sn film, such as InSb or CdTe, as has already been shown to improve the thermal stability of α-Sn [18] The

addition of the Ge would not alter the negative band gap directly, but the strain induced by the addition of the Ge into the Sn film grown on a substrate lattice matched to Sn would apply tensile strain.

While DPT does predict a semiconductor-to-semimetallic transition in bulk germanium at strains greater than 4%, the calculated critical thickness of such a film would be less than ≈3.8 nm. At this thickness band gaps on the order of magnitude of electron volts are estimated to be induced through confinement. This strongly suggests that semimetallic pure germanium cannot be readily fabricated.

References

[1] A. Sanchez-Soares, C. O'Donnell, and J. C. Greer, "Epitaxial stabilisation of $Ge_{1-x}Sn_x$ alloys." Unpublished.

[2] C. O'Donnell, A. Sanchez-Soares, C. A. Broderick, and J. C. Greer. Impact of stoichiometry and strain on $Ge_{1-x}Sn_x$ alloys from first principles calculations. *Journal of Physics D: Applied Physics*, vol. 54, no. 24, p. 245103, 2021.

[3] J. M. Soler, E. Artacho, J. D. Gale, A. García, J. Junquera, P. Ordejón, and D. Sánchez-Portal. The SIESTA method for ab initio order-N materials simulation. *Journal of Physics: Condensed Matter*, vol. 14, no. 11, p. 2745, 2002.

[4] T. Ozaki. Variationally optimized atomic orbitals for large-scale electronic structures. *Physical Review B*, vol. 67, no. 15, p. 155108, 2003.

[5] T. Ozaki and H. Kino. Numerical atomic basis orbitals from H to Kr. *Physical Review B*, vol. 69, no. 19, p. 195113, 2004.

[6] QuantumATK version 2017, Synopsys QuantumATK (www.synopsys.com/silicon/quantumatk.html).

[7] S. Smidstrup, T. Markussen, P. Vancraeyveld, J. Wellendorff, J. Schneider, T. Gunst, B. Verstichel, D. Stradi, P. A. Khomyakov, U. G. Vej-Hansen, *et al.* Quantumatk: An integrated platform of electronic and atomic-scale

modelling tools. *Journal of Physics: Condensed Matter*, vol. 32, p. 015901, 2020.

[8] H. J. Monkhorst and J. D. Pack. Special points for Brillouin-zone integrations. *Physical Review B*, vol. 13, no. 12, p. 5188, 1976.

[9] J. P. Perdew and A. Zunger. Self-interaction correction to density-functional approximations for many-electron systems. *Physical Review B*, vol. 23, no. 10, p. 5048, 1981.

[10] M. P. Polak, P. Scharoch, and R. Kudrawiec. The electronic band structure of $Ge_{1-x}Sn_x$ in the full composition range: indirect, direct, and inverted gaps regimes, band offsets, and the Burstein–Moss effect. *Journal of Physics D: Applied Physics*, vol. 50, no. 19, p. 195103, 2017.

[11] L. He, F. Liu, G. Hautier, M. J. T. Oliveira, M. A. L. Marques, F. D. Vila, J. J. Rehr, G.-M. Rignanese, and A. Zhou. Accuracy of generalized gradient approximation functionals for density-functional perturbation theory calculations. *Physical Review B*, vol. 89, no. 6, p. 064305, 2014.

[12] S. Gupta, B. Magyari-Köpe, Y. Nishi, and K. C. Saraswat. Achieving direct band gap in germanium through integration of Sn alloying and external strain. *Journal of Applied Physics*, vol. 113, no. 7, p. 073707, 2013.

[13] J. F. C. Baker and M. Hart. An absolute measurement of the lattice parameter of germanium using multiple-beam X-ray diffractometry. *Acta Crystallographica Section A*, vol. 31, p. 364, 1975.

[14] S.-G. Shen. Calculation of the elastic properties of semiconductors. *Journal of Physics: Condensed Matter*, vol. 6, p. 8733, 1994.

[15] H. J. McSkimin and P. Andreatch. Elastic moduli of germanium versus hydrostatic pressure at 25.0°C and -195.8°C. *Journal of Applied Physics*, vol. 34, p. 651, 1963.

[16] H. B. Huntington, The elastic constants of crystals. in *Solid State Physics*, vol. 7, p. 213, Cambridge: Elsevier, 1958.

[17] L. J. Bruner and R. W. Keyes. Electronic effect in the elastic constants of germanium. *Physical Review Letters*, vol. 7, p. 55, 1961.

[18] R. Farrow, D. Robertson, G. Williams, A. Cullis, G. Jones, I. Young, and P. Dennis. The growth of metastable, heteroepitaxial films of α-Sn by metal beam epitaxy. *Journal of Crystal Growth*, vol. 54, no. 3, p. 507, 1981.

[19] J. Thewlis and A. Davey. Thermal expansion of grey tin. *Nature*, vol. 174, no. 4439, p. 1011, 1954.

[20] D. L. Price, J. M. Rowe, and R. M. Nicklow. Lattice dynamics of grey tin and indium antimonide. *Physical Review B*, vol. 3, p. 1268, 1971.

[21] C. Buchenauer, M. Cardona, and F. Pollak. Raman scattering in gray tin. *Physical Review B*, vol. 3, no. 4, p. 1243, 1971.

[22] N. Bouarissa and F. Annane. Electronic properties and elastic constants of the ordered $Ge_{1-x}Sn_x$ alloys. *Materials Science and Engineering: B*, vol. 95, p. 100, 2002.

[23] V. Ozoliņš, C. Wolverton, and A. Zunger. Strain-induced change in the elastically soft direction of epitaxially grown face-centered-cubic metals. *Applied Physics Letters*, vol. 72, p. 427, 1998.

[24] V. Ozoliņš, C. Wolverton, and A. Zunger. Effects of anharmonic strain on the phase stability of epitaxial films and superlattices: Applications to noble metals. *Physical Review B*, vol. 57, no. 8, p. 4816, 1998.

[25] T. Asano, S. Kidowaki, M. Kurosawa, N. Taoka, O. Nakatsuka, and S. Zaima. Influence of Ge substrate orientation on crystalline structures of $Ge_{1-x}Sn_x$ epitaxial layers. *Thin Solid Films*, vol. 557, p. 159, 2014.

[26] E. P. O'Reilly. Valence band engineering in strained-layer structures. *Semiconductor Science and Technology*, vol. 4, no. 3, p. 121, 1989.

[27] F. Tran and P. Blaha. Accurate band gaps of semiconductors and insulators with a semilocal exchange-correlation potential. *Physical Review Letters*, vol. 102, no. 22, p. 226401, 2009.

[28] S. Zwerdling, B. Lax, L. M. Roth, and K. J. Button. Exciton and magneto-absorption of the direct and indirect transitions in germanium. *Physical Review*, vol. 114, no. 1, p. 80, 1959.

[29] S. Groves, C. Pidgeon, A. Ewald, and R. Wagner. Interband magnetoreflection of α-Sn. *Journal of Physics and Chemistry of Solids*, vol. 31, no. 9, p. 2031, 1970.

[30] B. L. Booth and A. W. Ewald. Nonparabolicity of the gray-tin $\Gamma_8{}^+$ conduction band. *Physical Review*, vol. 168, p. 796, 1968.

[31] P. Moontragoon, Z. Ikonić, and P. Harrison. Band structure calculations of Si–Ge–Sn alloys: Achieving direct band gap materials. *Semiconductor Science and Technology*, vol. 22, no. 7, p. 742, 2007.

[32] S. Wirths, D. Buca, and S. Mantl. Si–Ge–Sn alloys: From growth to applications. *Progress in Crystal Growth and Characterization of Materials*, vol. 62, no. 1, p. 1, 2016.

[33] A. Qteish and R. J. Needs. Improved model-solid-theory calculations for valence-band offsets at semiconductor-semiconductor interfaces. *Physical Review B*, vol. 45, p. 1317, 1992.

[34] J. P. Colinge and J. C. Greer, *Nanowire Transistors: Physics of Devices and Materials in One Dimension*. Cambridge: Cambridge University Press, 2016.

[35] C. Kittel, *Introduction to Solid State Physics*. New York: John Wiley&Sons Inc, 2005.

[36] Y.-S. Kim, M. Marsman, G. Kresse, F. Tran, and P. Blaha. Towards efficient band structure and effective mass calculations for III-V direct band-gap semiconductors. *Physical Review B*, vol. 82, p. 205212, 2010.

[37] H. Warlimont and W. Martienssen, *Springer Handbook of Condensed Matter and Materials Data*. Heidelberg: Spinger, 2005.

[38] D. Sherrington and W. Kohn. Speculations about grey tin. *Reviews of Modern Physics*, vol. 40, p. 767, 1968.

[39] L. Ansari, G. Fagas, J.-P. Colinge, and J. C. Greer. A proposed confinement modulated gap nanowire transistor based on a metal (tin). *Nano Letters*, vol. 12, no. 5, p. 2222, 2012.

[40] E. O'Reilly, *Quantum Theory of Solids*. London: Taylor & Francis, 2002.

[41] S. Küfner, J. Furthmüller, L. Matthes, M. Fitzner, and F. Bechstedt. Structural and electronic properties of α-tin nanocrystals from first principles. *Physical Review B*, vol. 87, no. 23, p. 235307, 2013.

[42] R. A. Carrasco, C. M. Zamarripa, S. Zollner, J. Menéndez, S. A. Chastang, J. Duan, G. J. Grzybowski, B. B. Claflin, and A. M. Kiefer. The direct bandgap of gray α-tin investigated by infrared ellipsometry. *Applied Physics Letters*, vol. 113, p. 232104, 2018.

[43] C. Rödl, J. Furthmüller, J. R. Suckert, V. Armuzza, F. Bechstedt, and S. Botti. Accurate electronic and optical properties of hexagonal germanium for optoelectronic applications. *Phys. Rev. Materials*, vol. 3, p. 034602, 2019.

[44] O. Madelung and U. Rössler, *Group IV Elements, IV-IV and III-V Compounds. Part b - Electronic, Transport, Optical and Other Properties*. Hei-

delberg: Springer, 2002.

[45] C. G. Van de Walle. Band lineups and deformation potentials in the model-solid theory. *Physical Review B*, vol. 39, no. 3, p. 1871, 1989.

[46] M. V. Fischetti and S. E. Laux. Band structure, deformation potentials, and carrier mobility in strained Si, Ge, and SiGe alloys. *Journal of Applied Physics*, vol. 80, p. 2234, 1996.

[47] S.-H. Wei and A. Zunger. Predicted band-gap pressure coefficients of all diamond and zinc-blende semiconductors: Chemical trends. *Physical Review B*, vol. 60, no. 8, p. 5404, 1999.

[48] B. J. Roman and A. W. Ewald. Stress-induced band gap and related phenomena in gray tin. *Physical Review B*, vol. 5, p. 3914, 1972.

[49] T. D. Eales, I. P. Marko, S. Schulz, *et al.* $Ge_{1-x}Sn_x$ alloys: Consequences of band mixing effects for the evolution of the band gap γ-character with Sn concentration. *Scientific Reports*, vol. 9, no. 1, p. 1, 2019.

[50] M. Cardona. Pressure dependence of the direct energy gap in germanium. *Journal of Physics and Chemistry of Solids*, vol. 17, p. 138, 1960.

[51] B. Welber, M. Cardona, Y.-F. Tsay, and B. Bendow. Effect of hydrostatic pressure on the direct absorption edge of germanium. *Physical Review B*, vol. 15, p. 875, 1977.

[52] A. R. Goni, K. Syassen, K. Strossner, and M. Cardona. Pressure dependence of the direct optical gap and refractive index of Ge and GaAs. *Semiconductor Science and Technology*, vol. 4, p. 246, 1989.

[53] M. El Kurdi, H. Bertin, E. Martincic, M. De Kersauson, G. Fishman, S. Sauvage, A. Bosseboeuf, and P. Boucaud. Control of direct band gap

emission of bulk germanium by mechanical tensile strain. *Applied Physics Letters*, vol. 96, no. 4, p. 041909, 2010.

[54] M. Virgilio, C. Manganelli, G. Grosso, G. Pizzi, and G. Capellini. Radiative recombination and optical gain spectra in biaxially strained n-type germanium. *Physical Review B*, vol. 87, no. 23, p. 235313, 2013.

[55] M. El Kurdi, G. Fishman, S. Sauvage, and P. Boucaud. Band structure and optical gain of tensile-strained germanium based on a 30 band k· p formalism. *Journal of Applied Physics*, vol. 107, no. 1, p. 013710, 2010.

[56] D. Mukherjee, K. D. Joshi, and S. C. Gupta. Pressure induced phase transition in tin: Ab-initio calculations. *Journal of Physics: Conference Series*, vol. 215, p. 012106, 2010.

Chapter 4

Structural properties and miscibility of strained and unstrained $Ge_{1-X}Sn_X$ alloys

4.1 Introduction

$Ge_{1-x}Sn_x$ alloys have a solid solubility limit of 1% tin in germanium [1], primarily due to the large difference in their atomic radii (15%). However, non-equilibrium growth techniques have been shown to enable larger incorporation of tin; significant progress has been made in past decades towards fabricating germanium-tin alloys by employing non-equilibrium epitaxial growth techniques, such as molecular beam epitaxy (MBE) and chemical vapor deposition (CVD), allowing realization of thin alloy films with thicknesses up to hundreds of nanometres [2–9].

Fabrication of crystalline $Ge_{1-x}Sn_x$ alloys in the range predicted to exhibit semimetallic behaviour in bulk form has also been experimentally achieved. Recently, atomically flat epitaxial films grown on Ge (100) with tin content as high as x = 0.46 were reported in the literature [10]. However, in this study, the high levels of

compressive strain resulting from the incorporation of such high tin content into films epitaxially strained to germanium substrates resulted in maximum crystalline film thicknesses of 3 nm. Such a low thickness might not be suitable for a device relying on semimetallic behaviour, as quantum confinement could open a band gap, depending on surface termination [11]. In contrast, the use of lattice-matched substrates has been reported to allow growth of alloys with compositions of $0.26 < x < 0.99$, and even stabilization of pure α-tin films with thicknesses in excess of 100 nm [2, 12–16]. As the semiconducting to semimetallic transition is predicted to occur at approximately 20% tin [17, 18], the reduction of strain associated with growth on lattice-matched substrates should allow fabrication of semimetallic $Ge_{1-x}Sn_x$ with thicknesses on the order of hundreds of nanometers, well above the length scales required for semimetal structures.

The aim of this chapter is to investigate the structural properties and thermodynamic stability of bulk and epitaxial $Ge_{1-x}Sn_x$ alloys in order to explore relative stability across the full alloy composition range. This allows us to devise strategies for maximizing the miscibility of $Ge_{1-x}Sn_x$ as well as the thicknesses of $Ge_{1-x}Sn_x$ films.

Sections of this chapter have been submitted for publication [19] or are published [20].

4.2 Computational details

Density functional theory (DFT) calculations are employed to obtain the parameters associated with alloy miscibility and stability, such as lattice parameters, elastic constants, and the alloy interaction energies described in section 2.4. As in the last chapter, a s4p4d3f2 basis set is employed for germanium and a s2p3d3f2 basis set is used for tin. Brillouin zone integrations are performed over a grid

generated according to the Monkhorst-Pack [21] scheme, maintaining a density of at least 7 k-points/$Å^{-1}$, and real-space quantities are discretised on a grid with an energy cut-off of at least 100 Ha. Spin orbit interactions are, as previously stated, not included in these calculations, although all alloy electronic band structure calculations reported in this thesis include spin orbit coupling.

Minimisation of the total energy with respect to ionic positions and periodic cell dimensions (geometry optimisation) is performed on all supercells to determine relaxed geometries, which are defined as having a maximum force acting on an atom less than a threshold of $|5 \times 10^{-2}\,\mathrm{eV/Å}|$, and with all elements of the corresponding stress tensors less than 0.1 GPa.

Special quasirandom structures (SQSs), as described in section 2.3, are implemented to mimic the site correlation functions of random alloys [22, 23]. A set of 64-atom cubic SQSs ($2 \times 2 \times 2$ simple cubic) have been generated stochastically using a simulated annealing procedure [24]. The dimensions of generated SQS allow targeting the site-site correlations of clusters found to be most relevant by the cluster expansion formalism, as will be seen in section 4.4.1.

The Bragg-Williams (BW) model, discussed in section 2.4.1, is used as a first approximation to estimate the Helmhotz free energy. To determine the nearest neighbour interactions in the BW model, energies for the homonuclear bonds Ge-Ge and Sn-Sn are obtained from the DFT total energies for relaxed diamond cells and for isolated Ge and Sn atoms, respectively. For the heteronuclear bond energy, a DFT total energy calculation is performed for a fictitious zinc-blende germanium tin alloy and taking the aforementioned isolated atom simulations as reference energies.

The most severe limitations inherent to the BW model can be overcome by including interactions beyond nearest neighbours through the cluster expansion (CE) formalism, as described in section 2.4.2. In order to define an optimal set

of clusters to include when building the CE for the germanium tin alloys, a set of 47 crystalline test structures with a maximum of 8 atoms per supercell are generated following an algorithm designed to maximise the predictive power of the fit whilst minimising the computational effort of the required first principles calculations [25]. The total energies for the test structures are used to extract the ECI coefficients for two atom clusters with a maximum range of 1 nm and for three atom clusters with a maximum range of 0.52 nm. The selection of clusters to include in the CE applies a statistical measure relying on a cross-validation score and variance minimisation techniques to reproduce the supercell energies for the test structures [26]. The resulting cross validation score is 5 meV/atom, which is comparable to the error expected from the DFT energies used to determine the ECI values.

The temperature dependence of the free energy requires determination of the configurational, electronic, and vibrational contributions to the entropy. The configurational entropy is estimated in a first approximation by enumerating unique atomic configurations for a random alloy at each composition, as detailed in section 2.4.1. The models employed for electronic and vibrational contributions to the free energy are outlined in section 2.4.3. The electronic band calculations employed for calculation of the electronic contributions are performed with the previously mentioned 64 atom SQSs. These cells are also used for estimating the vibrational contributions to the free energy.

Two cluster expansions are defined: the cluster expansion of the configurational energy from a set of 47 crystalline cells as described previously, and a second expansion for the temperature-dependent vibrational contributions to free energy computed from 64-atom SQS. These two expansions can then be merged to produce a set of temperature dependent ECI (TECI). In section 4.4.3, it will be shown that the electronic contributions to the free energy are negligible, and as such are

ignored. Once the TECI are determined, they can be implemented in semi-grand canonical ensemble Monte Carlo simulations, described in section 2.4.4, to calculate a phase diagram. Configurational entropy contributions are readily included in the MC method as the simulation samples accessible configurations at a given temperature. Supercells based on a face-centred cubic primitive cell ($84 \times 84 \times 84$) and with a corresponding lattice constant of 26 nm and 1,185,408 atomic sites are employed for an improved description of long-range order and ensemble averages. The number of equilibration passes and the averaging passes are determined based on a target precision of one part in a thousand for the atomic composition of the phase.

4.3 Structural and elastic properties of bulk $Ge_{1-x}Sn_x$

4.3.1 Lattice constant bowing

Many of the structural and elastic properties of the α-tin and germanium materials have been presented in the previous chapter. It is next investigated how the structural and elastic properties change over the alloy composition range $0 \leq x \leq 1$. This serves to verify the SQS plus DFT approach to calculating alloy properties.

To do this, the lattice constants and elastic constants from 64 atom SQSs across the composition range are fitted to:

$$p^{Ge_{1-x}Sn_x}(x) = p^{Ge}(1-x) + p^{Sn}x + b(p)x(1-x), \tag{4.1}$$

where $p^{Ge_{1-x}Sn_x}(x)$ is the alloy property p at composition x, p^{Ge} is the property for elemental germanium, p^{Sn} is the property for elemental α-Sn, and $b(p)$ is the bowing parameter. By fitting the data, it is then possible to generate continuous values of the properties over the composition range, allowing for the use of these

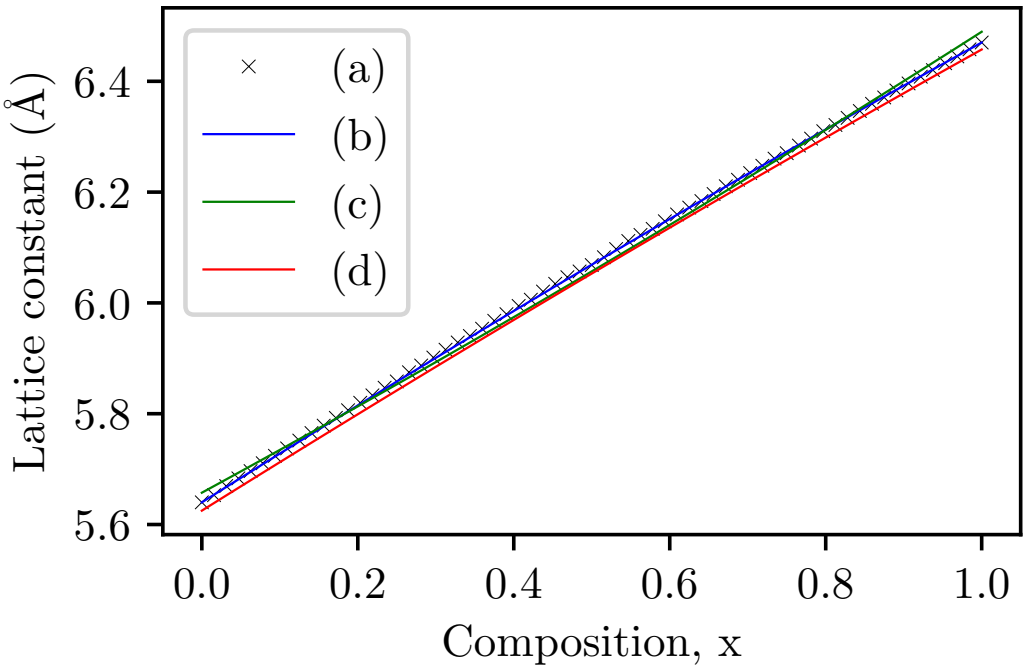

Figure 4.1: (a) Lattice constant of bulk 64 atom $Ge_{1-x}Sn_x$ cells as a function tin content (x), with the blue line (b) representing the fit to eq. (4.1). The experimental value (c) and the theoretical value (d) from Beeler et al. [27] are represented by the green and red lines respectively.

properties in models employed in later sections and chapters.

A small lattice constant bowing parameter of $b(a)$ = 0.056 Å is found, in agreement with other values reported in recent theoretical and experimental works: 0.047Å [27], -0.066Å [27], 0.041Å [3] and −0.083Å [17]. The data and fit to eq. (4.1) are represented in fig. 4.1. It is of note that the experimental data gives a bowing parameter of opposite sign to our theoretical calculations, however this could be as a result of compressive strain from the Si substrate on which the alloy was grown. These results lend credence to the SQS plus DFT approach, verifying that the cells reproduce one of the most fundamental material properties for these alloys.

4.3.2 Bond length analysis

Another method of verifying the SQS plus DFT approach is by analysing the bond lengths within the relaxed cells and comparing these to previously obtained theoretical and experimental results [28, 29]. The difference in atomic radii between the two alloy components results in the atomic positions in the relaxed SQS cells to exhibit a maximum root-mean-square deviation from ideal lattice sites of 0.157 nm at x = 0.5.

The Ge-Sn bond lengths presented in fig. 4.2 show good agreement with those obtained from previous studies. For previous DFT data obtained from cells of x = 0.0625 , average bond lengths of 2.583 Å and 2.584 Å are obtained, using the Heyd–Scuseria–Ernzerhof for solids (HSEsol) and local-density approxiation (LDA) exchange-correlation functions, respectively [28]. The value obtained from the corresponding SQSs in this work is 2.579 Å, showing good agreement with both of these previous models, deviating by less than 1% from the previous theoretical work. The previous study found that the standard deviation of the Ge-Ge bond lengths at this composition to be 0.014 Å, while in our calculations it was found to be 0.0128 Å, and the single Sn-Sn bond at this composition was found in HSEsol to be 2.704 Å, whereas our calculations show 2.706 Å.

The experimental extended X-ray absorption fine structure (EXAFS) data [29] on these bond lengths covers the 0.06 to 0.125 composition range and indicates Ge-Sn bond lengths ranging between 2.585 Å and 2.599 Å(including only the most strain relaxed films). The generated SQS cells within this range include the x = 0.0625, 0.09375, and 0.125 compositions, and exhibit average Ge-Sn bond lengths of 2.579 Å, 2.584 Å, and 2.591 Å, respectively, deviating from the average experimental bond lengths by less than 1%. Though the data does lie on the smaller side of the experimental range, this is to be expected as the LDA has been shown to cause an overestimation in binding energies, typically resulting in

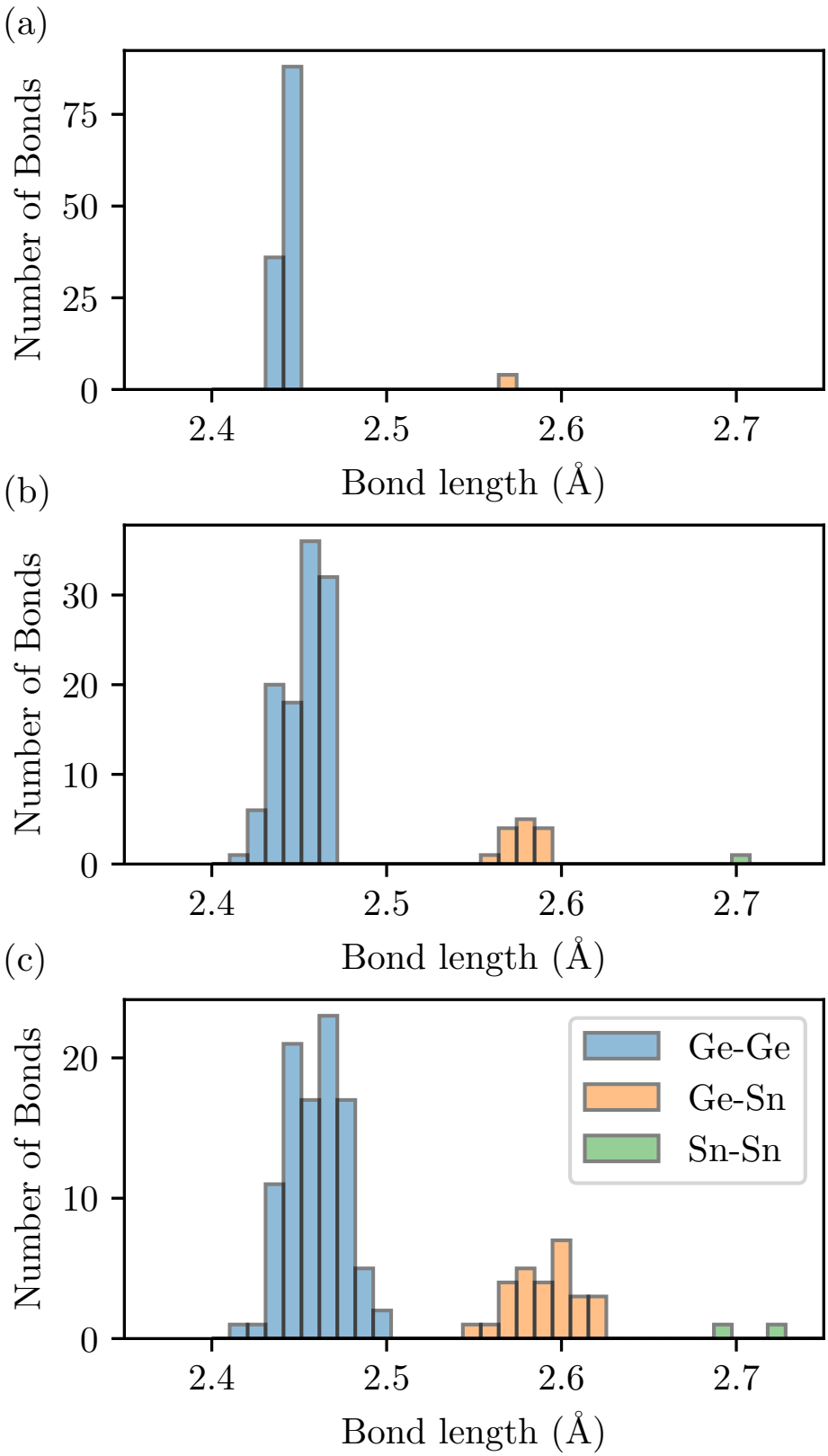

Figure 4.2: Bond lengths of 64 atom $Ge_{1-x}Sn_x$ SQSs for (a) x = 0.0156, (b) x = 0.0625, and (c) x = 0.125. The bond lengths have been sorted into bins of width 0.01 Å. The relaxed Ge-Ge bond length in germanium and the relaxed Sn-Sn bond length in α- tin are found to be 2.45 Å and 2.81 Å respectively.

smaller bond lengths [30].

The previous experimental and theoretical analysis has been performed for bond lengths at stoichiometries of $x < 0.125$. Going beyond the previously studies at low Sn compositions, fig. 4.3 presents the bond lengths across the full composition range of $0 \leq x \leq 1$ for the 64 atom SQS plus DFT/LDA model applied to fully relaxed cells. As is to be expected, the bond lengths increase as tin is added to the system, with the standard deviation increasing as x approaches 0.5, at which point the atoms displace away from the ideal fcc lattice sites, thereby increasing the deviation in bond lengths. This data ideally would be compared with EXAFS data of high tin content random $Ge_{1-x}Sn_x$ alloys, however, no such experimental data exists currently in the literature.

4.3.3 Elastic properties of $Ge_{1-x}Sn_x$ alloys

As stated in the previous chapter, the elastic constants parameterise how the material deforms with applied strain. While there are no experimental data for how the elastic constants vary as a result of alloying, there are conflicting theoretical studies [17, 31]. One previous study reports that the bowing parameters of the elastic constants are negligibly small [17], as calculated by DFT/LDA. However, Bouarissa et al. [31] shows that the elastic constant bowing is not negligible, although their calculations utilized the virtual crystal approximation (VCA). This involves creating a small cell of atoms, the pseudopotentials of which consist of a linear interpolation of the pseudopotentials of the alloy constituents, weighted by the alloy stoichiometry.

The elastic constant bowing parameters are obtained with the SQS plus DFT/LDA model and, in the same manner as the lattice constants, by fitting to eq. (4.1). Non-negligible bowing parameters of: $b(C_{11}) = -40.875$ GPa, $b(C_{12}) = -4.824$ GPa, and $b(C_{44}) = -30.408$ GPa are obtained. The effects of the bowing pa-

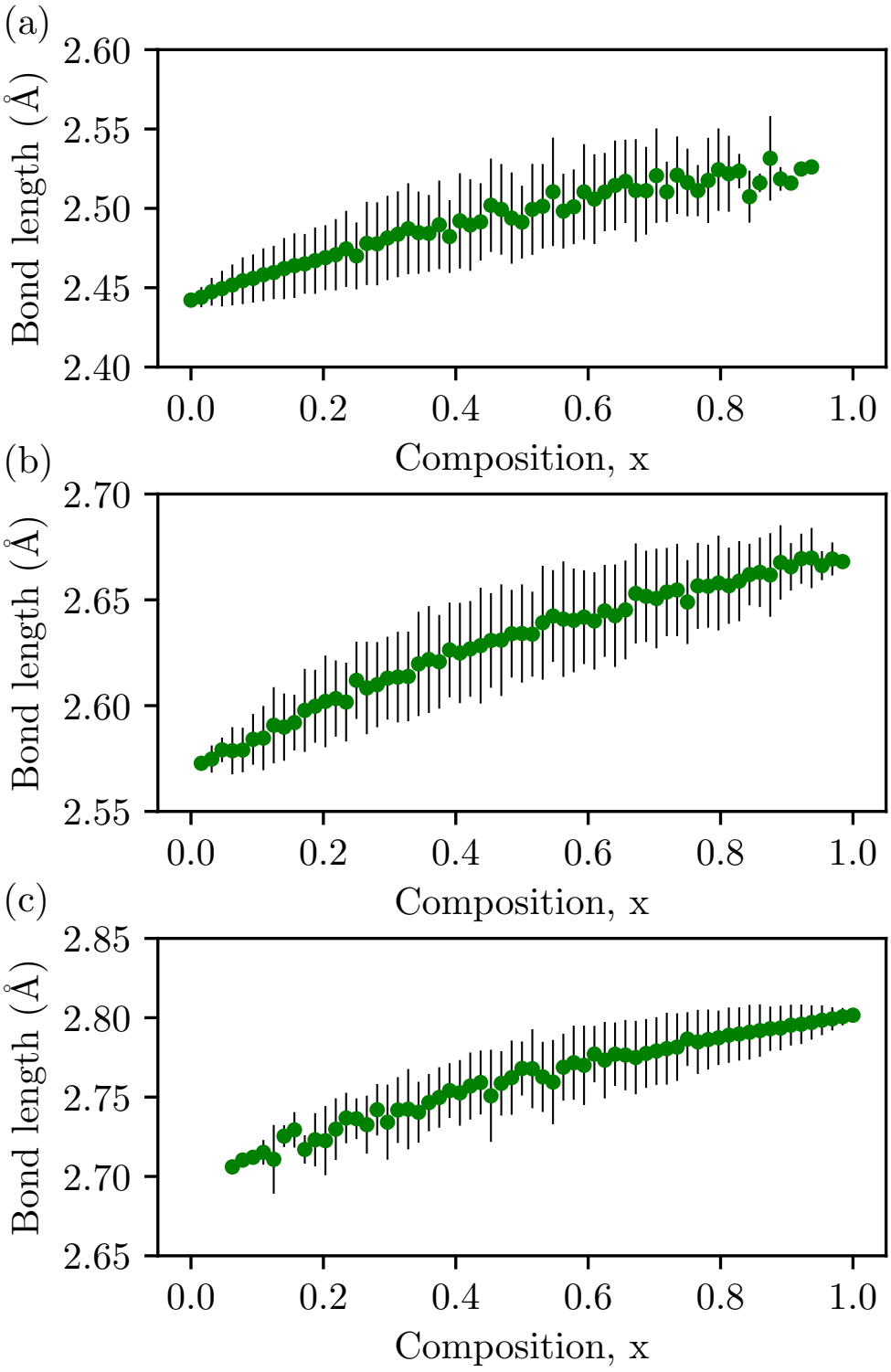

Figure 4.3: Average (a)Ge-Ge, (b) Ge-Sn, and (c) Sn-Sn bond lengths of 64 atom $Ge_{1-x}Sn_x$ from the SQS plus DFT/LDA model across the full composition range. Black bars indicate standard deviations.

rameters are compared to linear interpolations in fig. 4.4. The negative bowing parameters imply the material is softer relative to a linear interpolation, over the composition range. Of note is the C_{12} bowing parameter, which is shown to exhibit a composition dependent bowing, which becomes linear at high Sn content. The bowing parameters will be seen to be essential for predictions of the alloy critical thicknesses as well as for use in deformation potential theory, which will be applied in later chapters to predict alloy band gaps. Both of these methods are described in chapter 2.

4.4 Miscibility of bulk $Ge_{1-x}Sn_x$

4.4.1 Approximations to the formation energy

As discussed in chapter 2, the configurational dependence of a random alloy's energy across the composition range is required to analyse an alloy's miscibility through the generation of a phase diagram. However, generating such a diagram requires knowledge of a sizeable number of large simulation cells. This is computationally intractable using standard DFT methods. To circumvent this, alternative models are used to calculate the formation energies of the simulation cells. Two models are employed, the Bragg-Williams model and the cluster expansion formalism, as a means of estimating the free energy. The Bragg-Williams (BW) model, as discussed in section 2.4.1, is used to gain an understanding of the approximate behaviour of the alloy based on short range interactions, and the cluster expansion (CE) formalism, described in section 2.4.2, is used to provide a more accurate but more complex method of estimating the formation energy. Both of these models are compared to a small number of random SQS plus DFT/LDA calculations in order to gauge their accuracy.

The BW model requires obtaining nearest-neighbour interaction energies. In or-

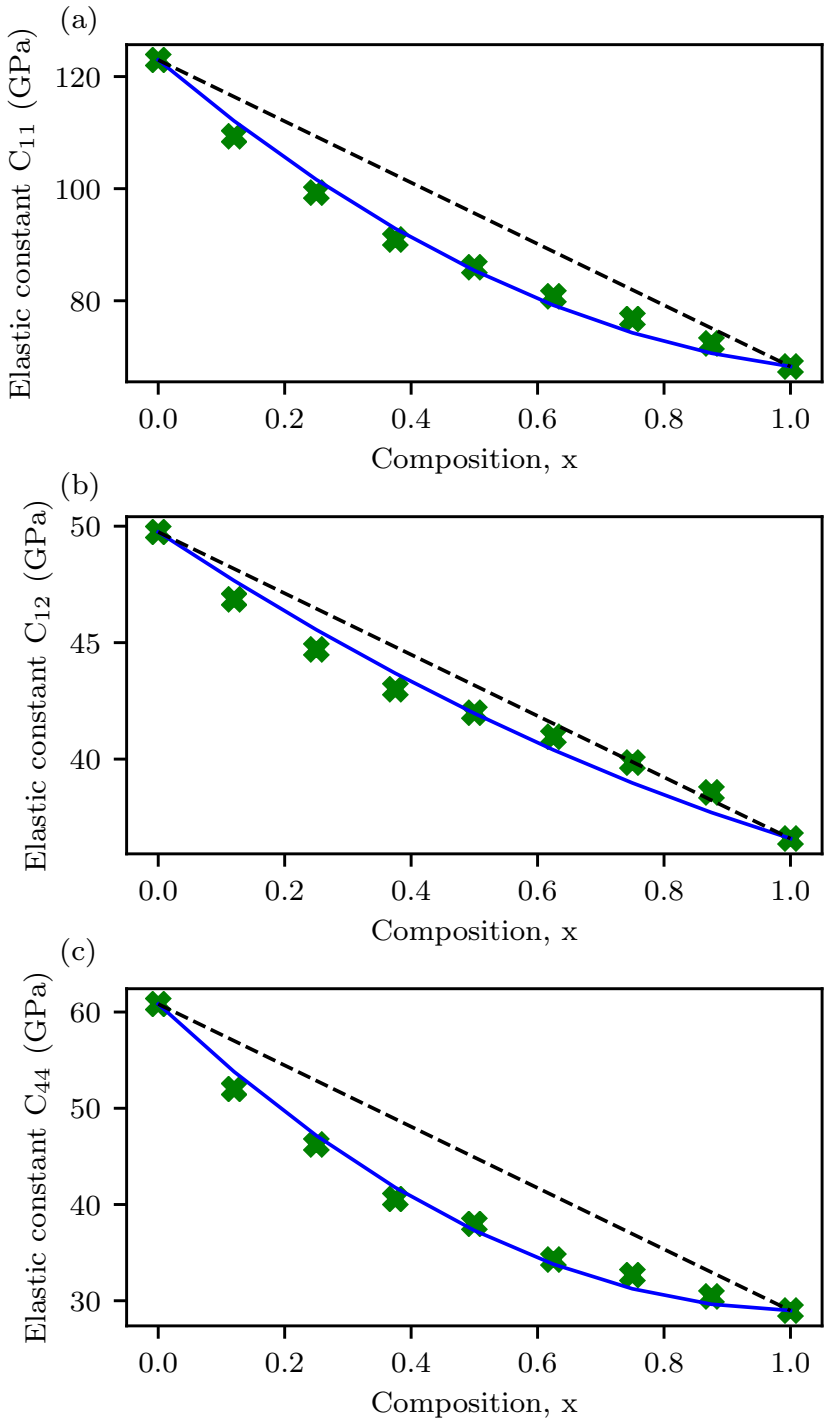

Figure 4.4: (a) C_{11}, (b) C_{12}, and (c) C_{44} elastic constants obtained from $Ge_{1-x}Sn_x$ 64 atom SQS cells. Blue solid lines represents the fits to eq. (4.1), and black dashed lines indicate a linear interpolation.

der to approximate these energies, the formation energy of germanium and tin's α phase, and an x = 0.5 alloy in a zincblende structure are found from DFT/LDA calculations, and the atomic energies are subtracted. A drawback to this parameterisation is that the bonds present in the zincblende structure of $Ge_{0.5}Sn_{0.5}$ are not representative of those found in a random alloy. However, this method provides a starting point for analysis of the miscibility of the system. Values of V_{SnSn} = −2.189 eV for the Sn-Sn bond, V_{GeGe} = −2.396 eV for the Ge-Ge bond, and V_{GeSn} = −2.281 eV for the Ge-Sn bond are found from these calculations. These parameters can be used to estimate the relative binding energy (V), described in section 2.4.1, given as:

$$V = V_{GeSn} - \frac{1}{2}(V_{GeGe} + V_{SnSn}). \tag{4.2}$$

These interaction energies predict a positive relative binding energy V_{GeSn} = 11 meV, indicating the alloy's preference to segregate at zero temperature. The internal energy E_i is calculated from:

$$E_i = \frac{Nz}{2}\{(1-x)V_{GeGe} + xV_{SnSn} + 2x(1-x)V\}, \tag{4.3}$$

where x is the concentration of Sn atoms, z is the number of nearest neighbours of each atom, and N is the total number of atoms. The formation energy (ΔH) is given as:

$$\Delta H = E_i - [(1-x)E_{Ge} + xE_{Sn}], \tag{4.4}$$

where E_{Ge} is the energy of a pure germanium cell and E_{Sn} is the energy of a pure α-tin cell. The formation energy over the composition range is depicted in fig. 4.5 and displays a positive formation energy at 0 K. However, when the configurational entropy is taken into account, as temperature reaches 300 K the miscibility gap vanishes, contrary to what is observed physically.

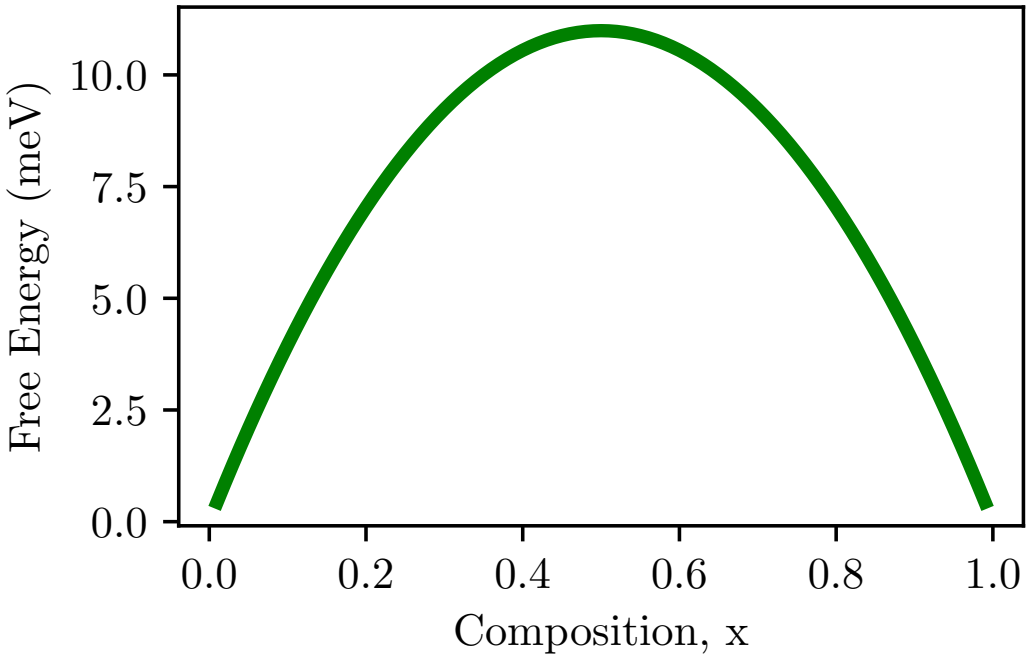

Figure 4.5: Formation energy of $Ge_{1-x}Sn_x$ per atom as calculated using BW model at 0 K parameterized from two atom primitive cells.

Figure 4.6 shows the formation energy per atom of random alloys with respect to spinodal decomposition across the concentration range, as predicted with the Bragg-Williams model, a nearest neighbour CE parameterised using the same cells as the BW model, a nearest neighbour cluster expansion as parameterised using the 64 atom SQSs, and as directly computed from DFT/LDA energetics for structurally optimized SQSs. Our BW model is observed to correctly predict immiscibility, however it significantly underestimates the formation energy of random alloys compared to results obtained with nearest neighbour CE fit to the SQSs and energies extracted from the SQS plus DFT/LDA model. As the BW model agrees, to within 1 meV, with the nearest neighbour CE fit to the same cells, the poor representation of the formation energy is deduced to be as a result of utilizing as few as three two atom simulation cells in obtaining the binding energies. By fitting the nearest neighbour CE to the 64 atom SQSs, it is found that it can reasonably reproduce the alloy formation energies, as long as it is fit to

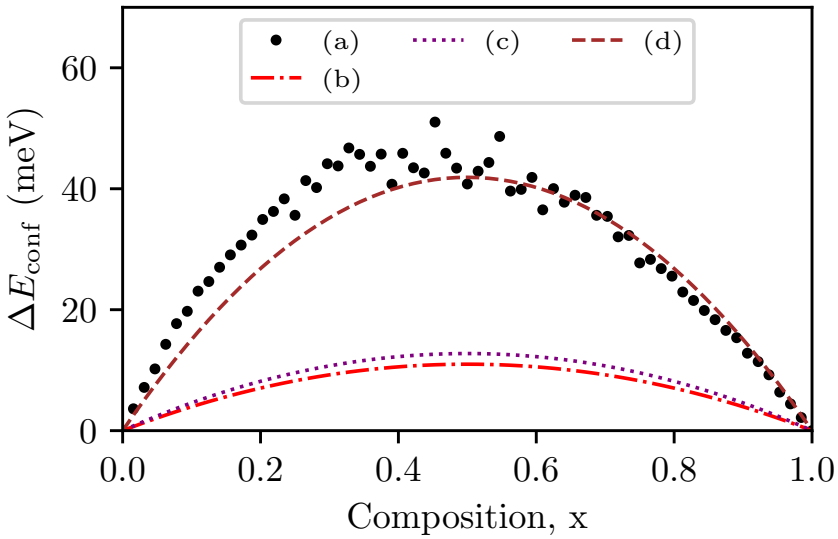

Figure 4.6: Formation energy of random $Ge_{1-x}Sn_x$alloys at zero temperature as calculated from (a) 64-atom SQSs as predicted by DFT simulations, (b) The BW model, (c) a nearest neighbour cluster expansion fit to the same three structures as the BW model, and (d) a nearest neighbour cluster expansion fit to the 64 atom SQSs.

a reasonable number of structures. This implies that the issue with the BW model is not with the model itself, but with how the bonding energies are obtained. The underestimation of the formation energy by the poor parameterisation over alloy composition is the cause of the predicted miscibility at 300 K by the BW model.

A more accurate description of alloy energetics has been obtained by fitting the energy of 47 crystalline structures with up to 8 atoms per cell to a cluster expansion including atomic pair interactions up to 1 nm apart, and atomic triplet interactions with a range up to 0.52 nm. Figure 4.7(a) shows fitted values of effective cluster interactions (ECIs), where ECIs are observed to decay rapidly with cluster diameter, and number of sites in the cluster from approximately 20 meV/atom, for nearest-neighbour pairs, down to less than 5 meV/atom for longer range pairs, and with even lower values associated to triplets included in the fit. The signs of these ECI, particularly the nearest neighbour ECI, have been ob-

served to flip depending on how many clusters are included in the fit, and which structures are used in the fit. As such, it is important to note that a cluster's contribution to the formation energy of a structure is dependent not only on the ECI but of the correlation function associated with that cluster. The CE cross-validation score, a measure of its predictive power analogous to the root mean square error [25], is 5 meV/atom, indicating a level of accuracy similar to that of DFT simulations used in the construction of the fit. In accordance with observed experimental behaviour and results from the BW model, CE results predict germanium and tin to be immiscible at zero temperature as no ordered structures were found to be energetically favourable with respect to segregation into each of the pure components across the entire composition range, or spinodal decomposition, reflected by the formation energies in fig. 4.7(b). It is of note that these ordered structures have a much higher formation energy than those of the SQSs. This is a reflection of our positive relative binding energy. As these small ordered simulation contain more Ge-Sn bonds, their formation energies are much higher than the SQSs, which contain a mixture of all three bond types, with like-like bonds being the energetically preferred bond type.

Figure 4.8 shows the formation energy per atom of random alloys, with respect to spinodal decomposition, across the concentration range as directly computed from DFT/LDA energetics for structurally optimized SQS, as predicted by a CE including triplet interactions applied to statistically random correlation functions, as well as the same CE applied to the same quasi-random correlation functions found within the SQSs. The higher accuracy and predictive power of the CE, achieved including longer range and triplet interactions, is reflected by its significantly smaller deviations away from formation energies directly computed from SQS plus DFT/LDA, where an RMS error of 2 meV/atom between both datasets has been computed. The CE predicted formation energies for quasi-random structures with site correlations corresponding to those of the previously generated

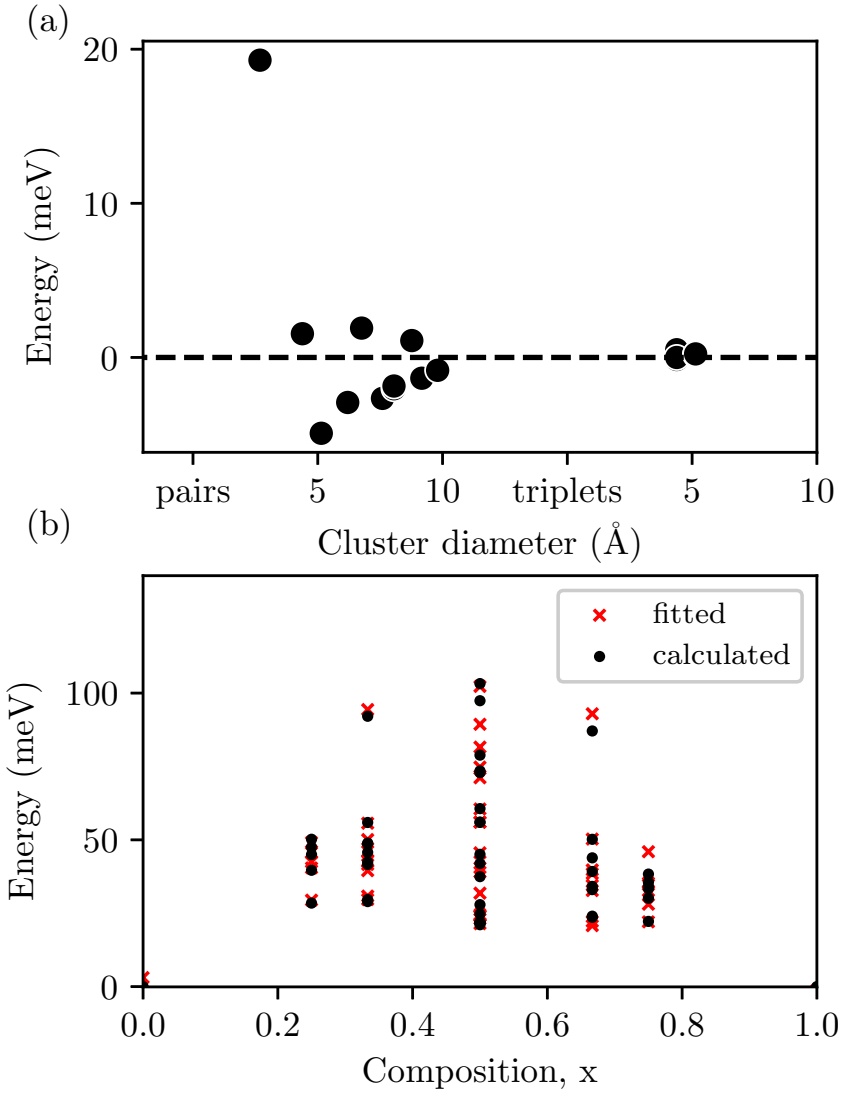

Figure 4.7: (a) Magnitude of effective cluster interactions (ECI) obtained in the cluster expansion fit for bulk alloys and (b) predicted and directly computed formation energies per atom for all structures included in the fit.

SQSs shows closer tracking of formation energies from SQS plus DFT/LDA calculations, especially around intermediate compositions where larger deviations are found. This highlights the impact of the imposed periodicity on SQS energetics. The inclusion of the triplet interactions also allows asymmetry in the formation energy curve. This is forbidden in the BW model as the formation energy reduces to $\Delta E_{\text{conf}} = V[x(1-x)]$, which is symmetric about $x = 0.5$. Asymmetry is also forbidden in cluster expansions which only include two atom clusters. This is due

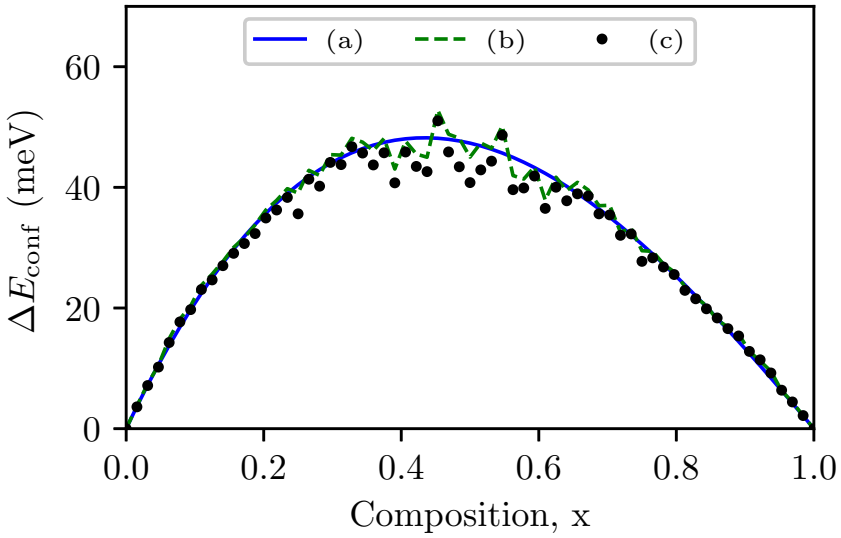

Figure 4.8: Formation energy at zero temperature of (a) random alloys and (b) quasi-random alloys as predicted by the cluster expansion; and (c) 64-atom SQSs as predicted by DFT simulations.

to the formula describing the ideally random correlation functions ($\bar{\Pi}_{k,m}$), given as $\bar{\Pi}_{k,m} = (2x-1)^k$, for a cluster with k vertices (lattice sites) and a range (maximum distance between two atoms) of m. This formula is always symmetrical for even values of k. As such, at least triplet interactions must be included to allow for asymmetry in the formation energy of a random alloy as predicted by the CE.

4.4.2 Decomposition of the formation energy

The asymmetry of the formation energy, visible in fig. 4.8, is investigated by decomposing the formation energy as calculated in DFT/LDA simulations as:

$$\Delta H = \Delta E_{VD} + \delta E_{UR}^{\text{chem}} + \delta E^{int}, \tag{4.5}$$

where the *volume deformation* energy ΔE_{VD} corresponds to the energy required to hydrostatically strain each of the constituents to the alloy's equilibrium lattice

parameter given as:

$$\Delta E_{VD} = (1-\mathrm{x})\big[E_{\mathrm{Ge}}(a_{\mathrm{Ge}_{1-\mathrm{x}}\mathrm{Sn}_{\mathrm{x}}}) - E_{\mathrm{Ge}}(a_{\mathrm{Ge}})\big] + \mathrm{x}\big[E_{\mathrm{Sn}}(a_{\mathrm{Ge}_{1-\mathrm{x}}\mathrm{Sn}_{\mathrm{x}}}) - E_{\mathrm{Sn}}(a_{\mathrm{Sn}})\big],$$

where $E_i(a_j)$ is the energy for i= {Ge,Sn} at the equilibrium lattice constant a_j for j={Ge, Sn, $Ge_{1-x}Sn_x$}. The *chemical* or *spin-flip* energy ($\delta E_{UR}^{\mathrm{chem}}$) corresponds to the energy gained when both components already constrained to the relaxed alloy lattice parameter bond together to form the alloy, given as:

$$\delta E_{UR}^{\mathrm{chem}} = E_{\mathrm{Ge}_{1-\mathrm{x}}\mathrm{Sn}_{\mathrm{x}}}(a_{\mathrm{Ge}_{1-\mathrm{x}}\mathrm{Sn}_{\mathrm{x}}}) - \big[(1-\mathrm{x})E_{\mathrm{Ge}}(a_{\mathrm{Ge}_{1-\mathrm{x}}\mathrm{Sn}_{\mathrm{x}}}) + \mathrm{x}E_{\mathrm{Sn}}(a_{\mathrm{Ge}_{1-\mathrm{x}}\mathrm{Sn}_{\mathrm{x}}})\big],$$

in the same notation as eq. (4.6), with the atomic positions still at their ideal lattice sites. The *internal relaxation* energy (δE^{int}) from eq. (4.5) is the energy gained when atomic positions in the alloy are allowed to relax, given as:

$$\delta E^{int} = E_{\mathrm{Ge}_{1-\mathrm{x}}\mathrm{Sn}_{\mathrm{x}}}(a_{\mathrm{Ge}_{1-\mathrm{x}}\mathrm{Sn}_{\mathrm{x}}})|_R - E_{\mathrm{Ge}_{1-\mathrm{x}}\mathrm{Sn}_{\mathrm{x}}}(a_{\mathrm{Ge}_{1-\mathrm{x}}\mathrm{Sn}_{\mathrm{x}}})|_{UR},$$

where R and UR indicate whether the atomic positions are relaxed or constrained to the ideal diamond lattice sites, respectively.

Figure 4.9 shows the dependence of each contribution as computed for 64-atom SQS across the composition range, and table 4.1 lists their magnitude at compositions x=0.25, x=0.50, and x=0.75. The large difference between the Ge and Sn equilibrium lattice parameter results in the volume deformation energy dominating and destabilising the alloys, and the marked asymmetry observed for this quantity can be ascribed to the significant difference between the components' bulk moduli; the volume expansion required to accommodate Sn into Ge-rich alloys increases the formation energy significantly more than the corresponding volume contraction associated with incorporation of Ge into Sn-rich alloys. Contributions arising from chemical interactions between different atomic species

Table 4.1: Formation energy (ΔH) decomposed into contributions listed in eq. (4.5), the *volume deformation* energy ΔE_{VD}, the *chemical* or *spin-flip* energy ($\delta E_{UR}^{\text{chem}}$), and the *internal relaxation* energy (δE^{int}), for bulk alloys with varying composition as calculated from DFT/LDA simulations of bulk alloys employing 64 atom SQSs.

Composition (x)	ΔH	ΔE_{VD}	δE_{UR}^{chem}	δE^{int}
	(meV/atom)			
0.25	36	192	-88	-67
0.50	41	207	-90	-76
0.75	28	128	-52	-48

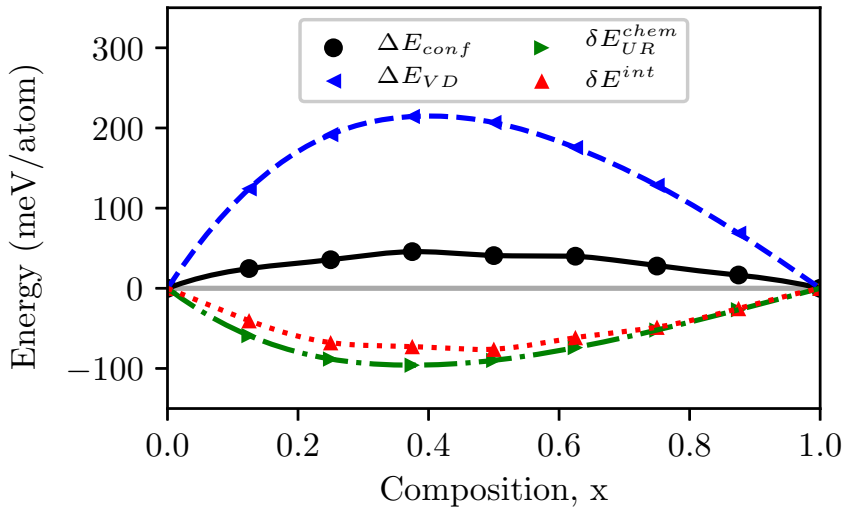

Figure 4.9: Decomposition of the formation energy obtained from DFT/LDA simulations of bulk alloys employing 64 atom SQSs.

and the relaxation of internal coordinates are of a similar magnitude and act to stabilise the alloys, partially offsetting the effects of the volume deformations. Although the magnitude of stabilising contributions correlates with the magnitude of volume deformation energies, the asymmetry present in the latter dominates formation energies and thus results in larger destabilisation for germanium-rich alloys compared to tin-rich alloys.

4.4.3 Finite temperature effects

The model is extended to finite temperatures by estimating the magnitude of configurational, electronic, and vibrational entropy contributions to alloy free energy, as described in section 2.4.3. In order to verify the bond stiffness versus bond length model employed to calculate vibrational contributions to the free energy in this work, we first present the phonon dispersions and phonon density of states computed with the bond stiffness versus bond length model, compared to experimental data. Figure 4.10 shows the phonon dispersions for germanium (Ge) and α-tin (α-Sn) as calculated using the model, with experimentally measured frequencies at high symmetry points marked with blue circles. The general features of phonon dispersions are reproduced reasonably well by the bond stiffness versus bond length approximation. Although the frequency of optical phonons at the Brillouin zone centre are reproduced within 5%, frequencies at some high symmetry points exhibit deviations of up to 20% with respect to experimentally measured values [32, 33].

Figure 4.11 depicts the frequency evolution of the Ge-Ge-like longitudinal optical (LO) vibrational mode in $Ge_{1-x}Sn_x$ alloys as a function of composition. Results obtained with the bond stiffness versus bond length model are compared to Raman spectroscopy measurements from Ref. [35]; calculated frequencies deviate less than 3% from measured values, and a similar linear decrease in Ge-Ge mode frequency is observed for increasing Sn composition. Figure 4.12 shows the evolution of the phonon density of states with Sn composition; a general trend whereby all peaks broaden and shift towards lower frequencies with increasing Sn content is observed. However, these films from which the experimental data were obtained are only partially relaxed, so this must be taken into consideration when comparing the obtained bulk theoretical values and the experimental data. In these experimental films it is likely that compressive strain increases as

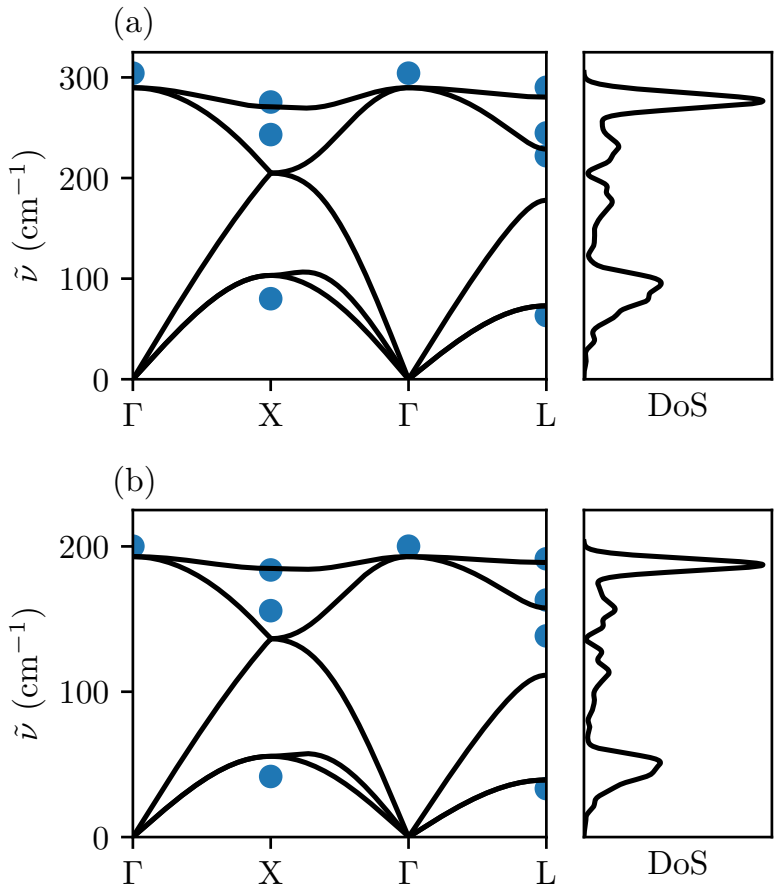

Figure 4.10: Phonon dispersions and phonon density of states for (a) Ge and (b) α-Sn computed with the bond stiffness versus bond length model. Experimental values for Ge [34] and α-Sn [33] are shown as blue circles.

Sn content increases. This would in turn increase the frequency of the Ge-Ge longitudinal mode, and as such the slope of line (a) in fig. 4.11 would be steeper if these films were fully strain relaxed.

As can be seen from the analysis of the dispersions and the evolution of the Ge-Ge LO mode as a function of Sn composition, the bond stiffness vs bond length model correctly reproduces the main qualitative features of Ge, α-Sn, and $Ge_{1-x}Sn_x$ reported in the literature. Even though accuracy is not enough for detailed quantitative predictions, the model provides an adequate description for identifying trends in the evolution of the vibrational properties of $Ge_{1-x}Sn_x$ alloys.

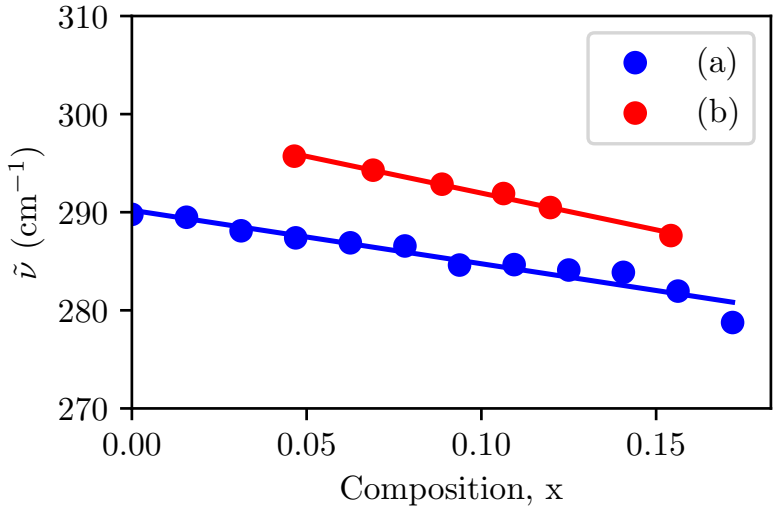

Figure 4.11: Frequency of Ge-Ge like longitudinal optical phonon modes in relaxed $Ge_{1-x}Sn_x$ alloys as a function of Sn composition (a) computed from the bond stiffness versus bond length model and (b) from Raman spectroscopy measurements [35].

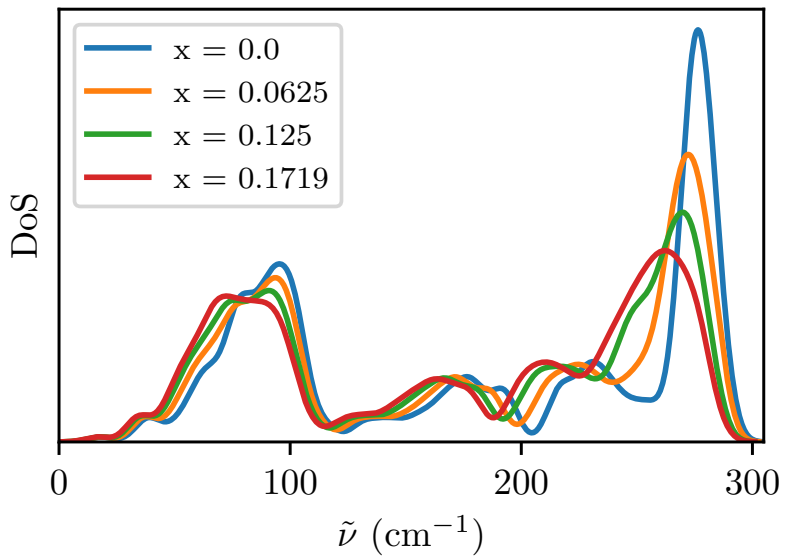

Figure 4.12: Evolution of the phonon density of states in relaxed $Ge_{1-x}Sn_x$ alloys for increasing Sn composition.

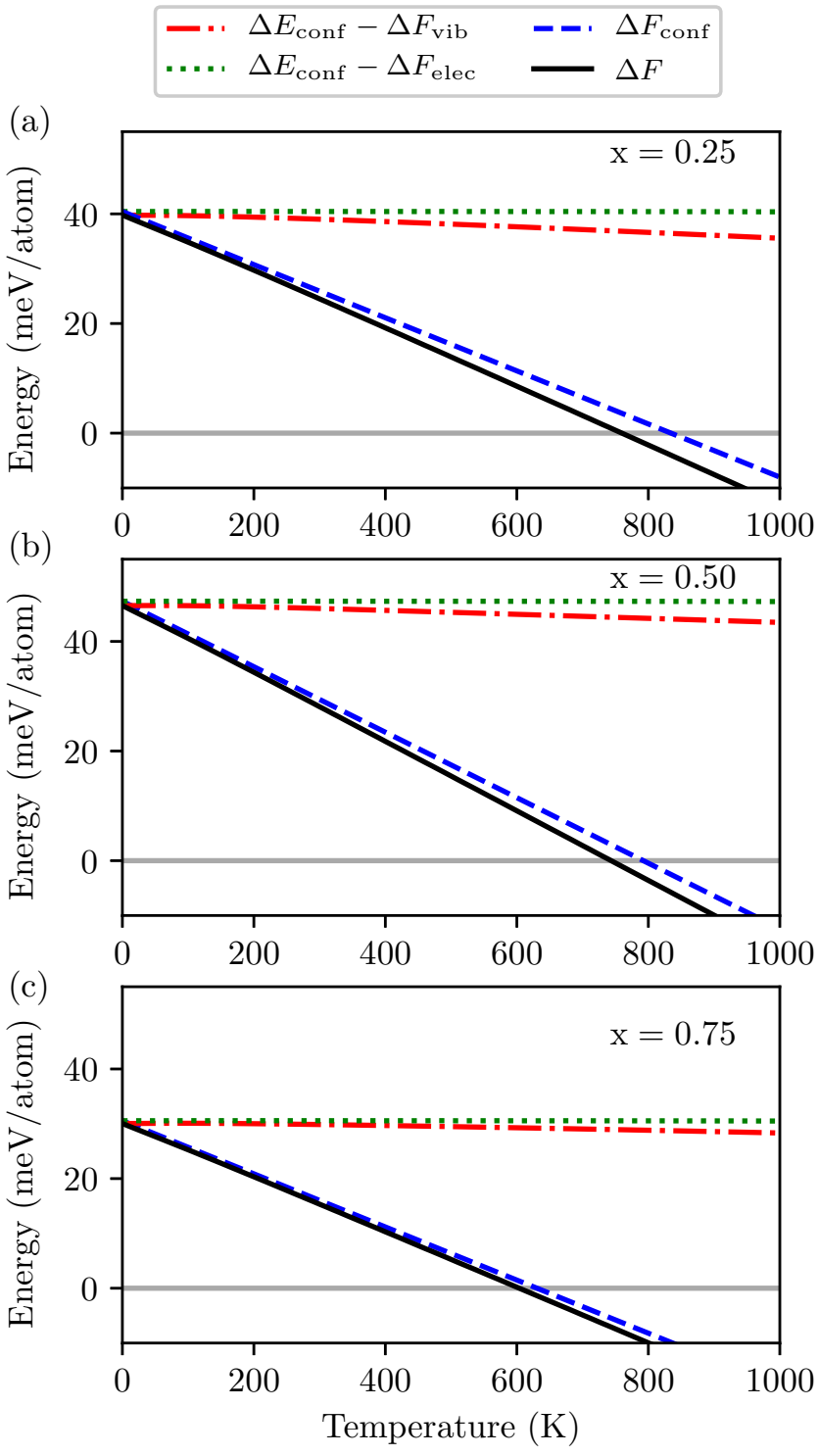

Figure 4.13: The total free energy of mixing (ΔF), the configurational free energy (ΔF_{conf}), the difference between ΔE_{conf} and the vibrational contributions to the free energy (ΔF_{vib}) and the difference between ΔE_{conf} and the electronic contributions to the free energy (ΔF_{elec}) as estimated from the CE of the $Ge_{1-x}Sn_x$ alloy as a function of temperature for (a) x = 0.25, (b) x = 0.50, and (c) x = 0.75 alloy compositions, normalized to the total free energy of mixing at 0 K.

Figure 4.13 shows the temperature dependence of the free energy of mixing relative to the unmixed alloy constituents (ΔF) for structures at compositions of x = 0.25, 0.5, and 0.75. Configurational contributions dominate alloy stabilization while vibrational entropy of mixing contributes to a lesser degree, with values approximately an order of magnitude lower at temperatures above 200 K in compositions shown in the figure. The electronic contributions to the alloy free energy have been found to be negligible, with computed values varying within a range of 1 meV/atom at temperatures up to 1000 K across the entire concentration range, as expected for non-metallic alloys. Predicted critical temperatures, *i.e.* temperatures at which the disordered phase becomes energetically favourable, indicated by a negative ΔF, are observed to decrease for larger tin compositions in a result attributable to the asymmetry observed in the alloy's configurational energy of mixing ΔH (see fig. 4.8).

4.4.4 Phase diagrams calculations

The impact of the asymmetry on the system's critical temperature is revealed by the phase boundary between the disordered phase (*i.e.* random alloy) and decomposition into the elemental phases. Lattice model Monte Carlo simulations employing the CE fit enable larger supercells than tractable with DFT to be studied, resulting in a much-improved treatment for ensemble averages over large numbers of alloy configurations. Temperature effects are included by combining ECIs describing the internal configurational energies with configurational and vibrational free energy contributions. The resulting phase diagram for $Ge_{1-x}Sn_x$ is shown in fig. 4.14, where two horizontal lines indicating the temperatures for the $\alpha \rightarrow \beta$ phase transition and melting point of tin have been included for reference. The higher transition temperatures found with this method, when compared to those shown in fig. 4.13, are attributed to a more accurate treatment of configurational

entropy contributions, as the MC simulation accounts for energy variations across alloy configurations. Germanium-rich alloys with compositions up to $x = 0.005$ are predicted to be stable below the eutectic temperature, in agreement with previous reports [36]; for tin-rich alloys, stability is only observed for compositions $x > 0.995$ at temperatures where α-Sn remains stable. It is worth noting that only the thermodynamic properties of alloys based on cubic structures have been simulated when computing the phase diagram. Since neither the liquid phase nor β-Sn have been considered in the model, deviations from experimentally derived phase diagrams are to be expected at temperatures above the α-Sn $\rightarrow$ β-Sn transition temperature. The predicted stability of tin-rich alloys in the temperature range where β-Sn is stable is an artefact due to considering cubic structures only. At intermediate compositions, predicted critical temperatures are well above the melting temperature for tin; experimental literature reports no such alloys in a solid state. These results support previous reports that growth of bulk equilibrium $Ge_{1-x}Sn_x$ alloys at technologically relevant compositions is not possible at standard pressure. It is worth noting that inclusion of vibrational free energy contributions reduces predicted critical temperatures, with larger reductions for germanium-rich compositions. This can be attributed to a stabilising effect associated from softening of phonon modes by addition of tin, partially counteracting the destabilising effects of volume deformations [35, 37, 38].

4.5 $Ge_{1-x}Sn_x$ under epitaxial strain

4.5.1 Formation energy of strained cells relative to coherent segregation

The primary factor leading to the high critical temperatures has been shown to arise from the large difference in equilibrium volumes for germanium and tin.

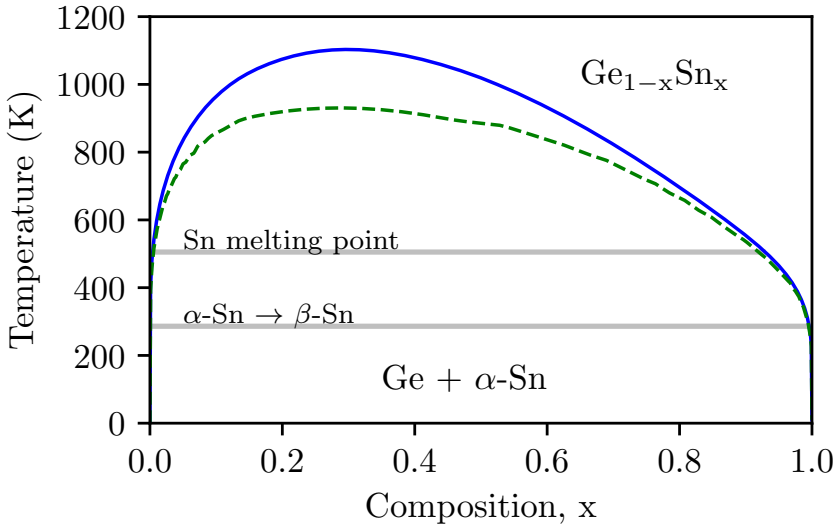

Figure 4.14: Phase diagram of bulk alloys as computed using a lattice model Monte Carlo simulation based on a cubic structure. CE fits constructed including (dashed line) and excluding (solid line) vibrational degrees of freedom have been employed. Regions above the curves represent stability for random alloys. Horizontal lines indicate temperatures at which phase transformation and melting occurs for Sn.

Although these findings can be anticipated based on the large difference between the atomic radii of germanium and tin, the purpose of this work is to quantify the magnitude of the energies required to be overcome to stabilise thin films. By coherent epitaxial growth, the lattice spacing parallel to a substrate can, to a large extent, be constrained within a thin film and result in stabilisation [39–41]. The extent to which coherent growth can stabilise germanium tin alloys is examined by constraining lattice parameters for the SQS along a selected plane to mimic the effect of growth on substrates for which epitaxially stable films of α-Sn and/or germanium-tin alloys have already been demonstrated, namely: Ge (0.564 nm), ZnTe/GaSb (0.610 nm), and CdTe/InSb (0.648 nm) [2, 12, 15, 16, 42, 43]. The CdTe/InSb substrate corresponds to the lattice parameter of Sn, and ZnTe/GaSb corresponds to approximately the average of the Ge and Sn lattice parameters. The strain imparted by the Ge substrate to the $Ge_{1-x}Sn_x$ alloy is compressive, starting at 0 strain at x= 0 and ranging as high as 15% at x= 1. This 15% limit

is set by the lattice mismatch between Ge and Sn. The reverse is true for the CdTe/InSb substrate, being able to apply a maximum tensile strain of 15%, on an x= 0 alloy. ZnTe/GaSb, being intermediary in lattice constant to the previous two substrates, can impart a maximum of approximately 7.5% compressive or tensile strain, for x=1 or x=0 alloys, respectively.

As stated in section 3.2.3, ⟨100⟩-oriented films tend to minimise internal strain energy, and thus structural defects for epitaxially coherent $Ge_{1-x}Sn_x$ films, compared to other film orientations. Epitaxial growth on (001)-oriented substrates is simulated by constraining the lattice constants of 64-atom SQSs in the two axes perpendicular to the [001] direction to match the lattice spacing of each of the substrates while allowing the cell to relax along the [001] direction. While this scheme neglects the potentially large role of surfaces and interfaces inherently present in thin films, it provides a baseline for the energetics of the alloy compositions independent of these effects.

Figure 4.15 shows the computed epitaxial formation energy relative to constituents strained to the *substrate* lattice parameter, referred to here as coherent segregation. This can be represented as:

$$\Delta H_{\text{coherent}} = E_{\text{alloy}}(a_{\text{epi}}) - (1-\text{x})E_{\text{Ge}}(a_{\text{epi}}) - \text{x}E_{\text{Sn}}(a_{\text{epi}}), \tag{4.6}$$

where $E_{\text{i}}(a_{\text{epi}})$ is the energy of material i epitaxially strained to the substrate lattice parameter and allowed to relax out of plane. Relaxations within the SQS plus DFT/LDA model of alloys constrained to Ge(100) substrates with compositions above x = 0.56 resulted in amorphous structures, and have thus been excluded from the analysis. These highly compressively strained SQSs do not exhibit a face-centered cubic structure, as can be seen in fig. 4.16. Figure 4.17 compares the bond lengths in this compressively strained cell to those of the relaxed cell. From this comparison an overall broadening is observed in the spread for each

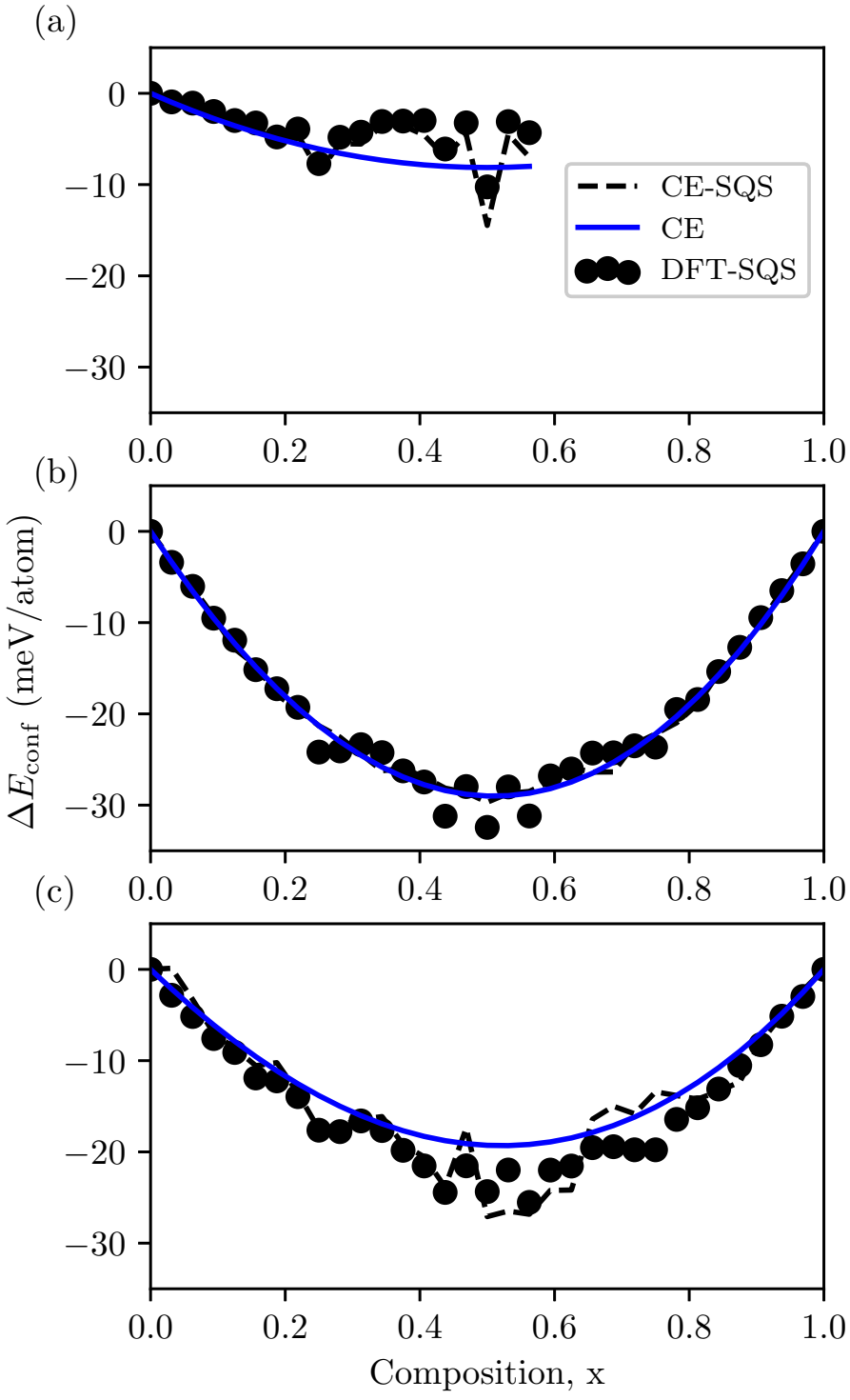

Figure 4.15: Formation energy with respect to coherent decomposition as calculated from DFT plus SQS, a cluster expansion using random correlations (CE), and a cluster expansion using quasi-random correlations (CE-SQS) as a function of composition, for alloys grown on (a) Ge, (b) ZnTe/GaSb, and (c) CdTe/InSb. Formation energies for alloys grown on Ge are only shown for $x < 0.56$, as above this alloy composition the cells became amorphous.

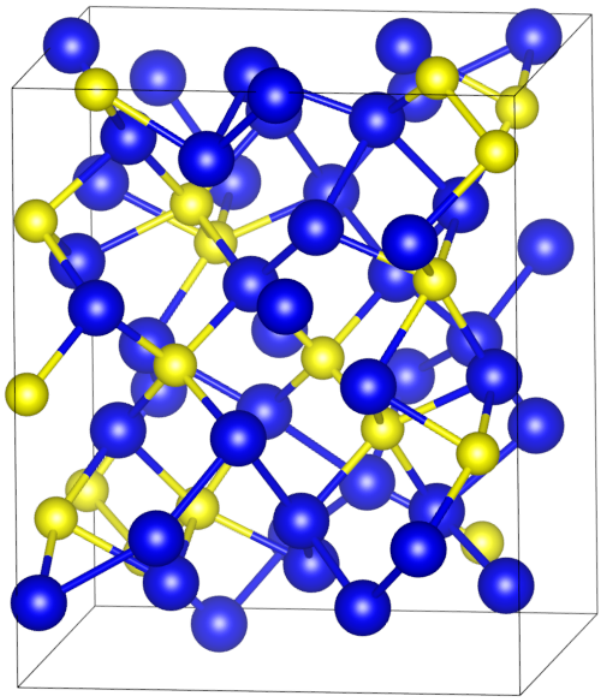

Figure 4.16: $Ge_{0.281}Sn_{0.719}$ SQS epitaxially strained to the lattice parameter of Ge, exhibiting an amorphous structure as opposed to the expected face-centered cubic structure. Blue atoms represent Sn and yellow atoms represent Ge.

bond length. It is also of note that each type shows an increase in length for many of the bonds present, despite the applied compressive strain. This may be as a result of the atoms relaxing so far from their ideal lattice parameters that their nearest neighbours change.

The strain-induced increase in energy of the alloy constituents imposed by the *substrate* is observed to result in the miscibility of the alloy over the full composition range, even at zero temperature. Formation energies obtained from *ab-initio* simulations have been fitted to CEs, as described in section 4.4.1, in order to investigate the case of random alloys and eliminate variations arising from the use of quasi-random correlations in the SQS +DFT/LDA model. The CE fits predict all $Ge_{1-x}Sn_x$ alloys to be energetically favourable with respect to coher-

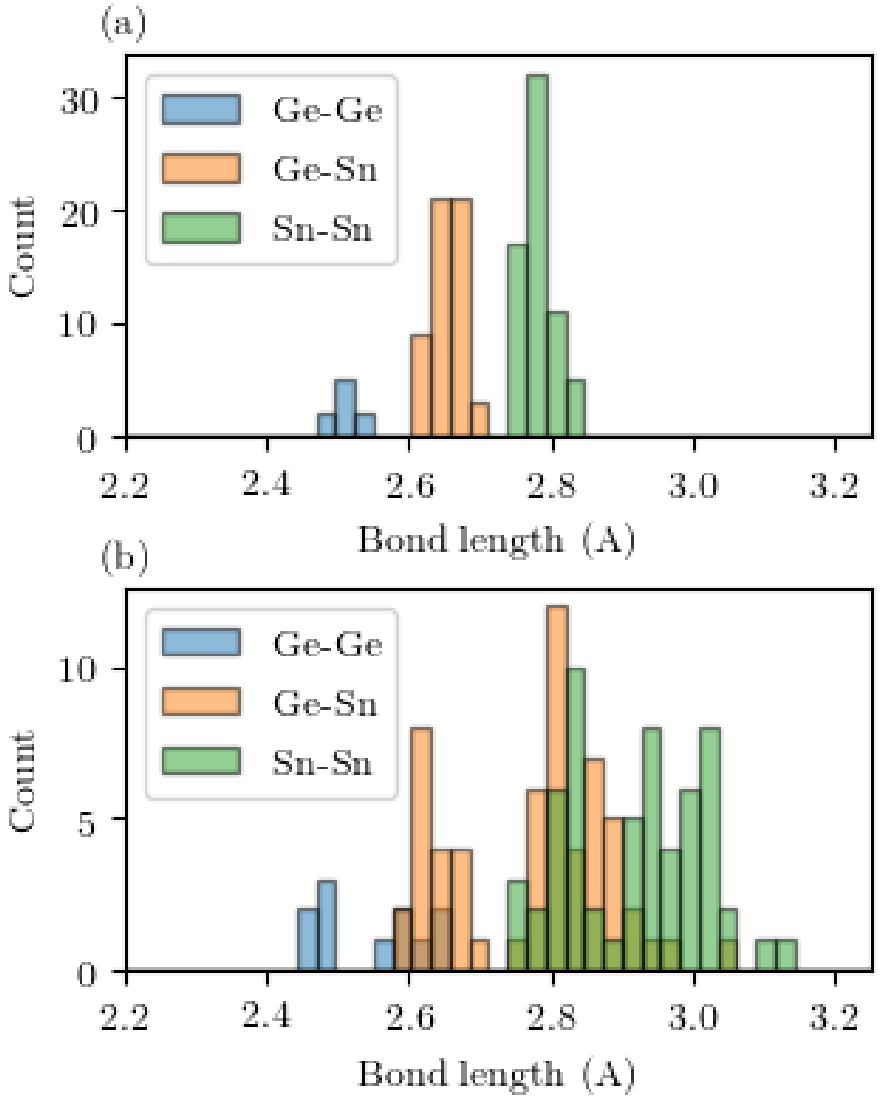

Figure 4.17: Bond lengths for (a) a relaxed $Ge_{0.281}Sn_{0.719}$ SQS and (b) the same SQS epitaxially strained to the lattice parameter of Ge.

ent segregation on each of the three substrates. The results show a trend where, for a given composition, miscibility decreases within this approximation along the (ZnTe/GaSb)-(CdTe/InSb)-Ge sequence, with the maximum difference in stability at x = 0.5, indicating growth on germanium to be the least favourable across the composition range. However, as we will see in section 4.5.5, $Ge_{1-x}Sn_x$ alloys with too large a lattice mismatch to the simulated substrate cannot reach usable thicknesses when grown. As such, while the Ge substrate may cause poorer miscibility for low Sn content $Ge_{1-x}Sn_x$ alloys when compared to the ZnTe/GaSb

substrate within this approximation, the ZnTe/GaSb substrate would not be suitable for these low x compositions due to the large strain imparted by the substrate lowering the mechanical stability of the $Ge_{1-x}Sn_x$ alloy.

From analysis of the vibrational contributions to the free energy in a manner similar to fig. 4.13, it is found that the aforementioned sequence in pseudomorphic alloy stability is maintained at finite temperatures, although we note that the bond stiffness versus bond length model and harmonic approximation employed in this work are inadequate to describe the vibrational properties of pseudomorphic germanium and tin with up to 15% biaxial strain, as evident from the c_{eq} calculations employing continuum elastic theory (CET), as described in section 4.5.4.

4.5.2 Decomposition of epitaxially strained formation energies relative to coherent segregation

Decompositions of epitaxial formation energies akin to those defined for bulk alloys in eq. (4.5) are presented in table 4.2 for alloys with composition x = 0.5. The effects of growth on lattice-matched substrates can be observed in the formation energy decomposition corresponding to ZnTe/GaSb substrates. While computed epitaxial spin-flip ($\delta E^{\text{chem,epi}}$) and internal relaxation ($\delta E^{\text{int,epi}}$) energies remain similar to the values for the corresponding bulk alloy, volume deformation energy relative to epitaxially coherent decomposition $\Delta E_{VD}^{\text{epi}}$ is reduced by 37%, resulting in a significantly enhanced stability.

By comparing results across substrates it is observed that coherent segregation results in an overall reduction of $\Delta E_{VD}^{\text{epi}}$ as *substrate* lattice parameter increases. The formula for calculating this parameter has been altered from eq. (4.5), and

Table 4.2: Epitaxial formation energy decomposition for alloys with composition x = 0.5 grown on each of the substrates included in this study.

Substrate	ΔH^{epi}	$\Delta E_{VD}^{\text{epi}}$	$\delta E_{UR}^{chem,\text{epi}}$	$\delta E^{int,\text{epi}}$
		(meV/atom)		
Ge	-10	195	-107	-97
ZnTe/GaSb	-32	131	-89	-75
CdTe/InSb	-24	114	-76	-62

now takes the form:

$$\Delta E_{VD}^{\text{epi}} = [E_{\text{Ge}}(a_{\text{alloy}}) - E_{\text{Ge}}(a_{\text{epi}})](1-\text{x}) + [E_{\text{Sn}}(a_{\text{alloy}}) - E_{\text{Sn}}(a_{\text{epi}})]\text{x}, \tag{4.7}$$

where $E_{\text{i}}(a_{\text{alloy}})$ is the energy of material i = {Ge, Sn} with the in plane lattice parameter of the epitaxially strained alloy.

By comparing results across the different substrates, it is observed that destabilisation of component segregation results in an overall reduction of $\Delta E_{VD}^{\text{epi}}$ with increasing substrate lattice parameter due to germanium's larger bulk modulus. However, the magnitudes of stabilising contributions $\delta E_{UR}^{\text{chem,epi}}$ and $\delta E^{\text{int,epi}}$ are observed to also decrease with increasing bond lengths associated with alloys grown on substrates with larger lattice spacings. This leads to the ZnTe/GaSb substrate exhibiting the lowest value of $\Delta E_{\text{conf}}^{\text{epi}}$ across the three substrates.

4.5.3 Formation energy of strained cells relative to relaxed segregation

The relative stability of alloys grown on different substrates in fig. 4.18 are compared by computing epitaxial alloys' formation energies with respect to spinodal decomposition into their bulk components, given as:

$$\Delta H_{\text{relaxed}} = E_{\text{alloy}}(a_{\text{epi}}) - (1-\text{x})E_{\text{Ge}}(a_{\text{Ge}}) - \text{x}E_{\text{Sn}}(a_{\text{Sn}}), \tag{4.8}$$

where $\Delta H_{\text{relaxed}}$ is the formation energy, $E_{\text{alloy}}(a_{\text{epi}})$ is the energy of the epitaxially strained $Ge_{1-x}Sn_x$ alloy, $E_{\text{Ge}}(a_{\text{Ge}})$ is the energy of Ge at the Ge lattice constant, and $E_{\text{Sn}}(a_{\text{Sn}})$ is the lattice constant of Sn at the Sn lattice constant. The substrate providing the lowest formation energy (and thus highest stability with respect to non-coherent decomposition) is observed to depend on alloy composition. Within the chosen set of substrates, Ge is preferred for compositions below x = 0.25, CdTe/InSb for compositions above x = 0.76, and ZnTe/GaSb for $0.25 < x < 0.76$, indicating the latter to be energetically favourable across most of the composition range where the alloy exhibits semimetallic behaviour. These results are consistent with the most energetically favourable substrate matching to the relaxed lattice parameter. The asymmetry discussed for bulk alloys whereby tin-rich compositions exhibit increased stability is also observed for alloys grown on ZnTe/GaSb, as can be clearly seen in fig. 4.18.

However, decomposition into completely relaxed alloy components is unrealistic, as strain would be applied by the substrate. Varying local strain would also be exhibited as a result of Sn rich and Sn poor regions of the film. As such, the approximation of relaxed segregation highlights behaviour in an idealised model where these effects are ignored.

4.5.4 Out-of-plane relaxation of strained cells

Figure 4.19 shows the magnitude of the out-of-plane lattice parameter c_{eq} for each substrate as computed with SQS plus DFT/LDA and as predicted by continuum elasticity theory (CET) [40], which is utilized in the deformation potential theory described in section 2.5.2 and the critical thickness model described in section 2.5.1. Good agreement between both methods is obtained across most of the composition range in Ge and ZnTe/GaSb substrates, whereas significant deviations are observed below approximately x = 0.5 tin content alloys coherent

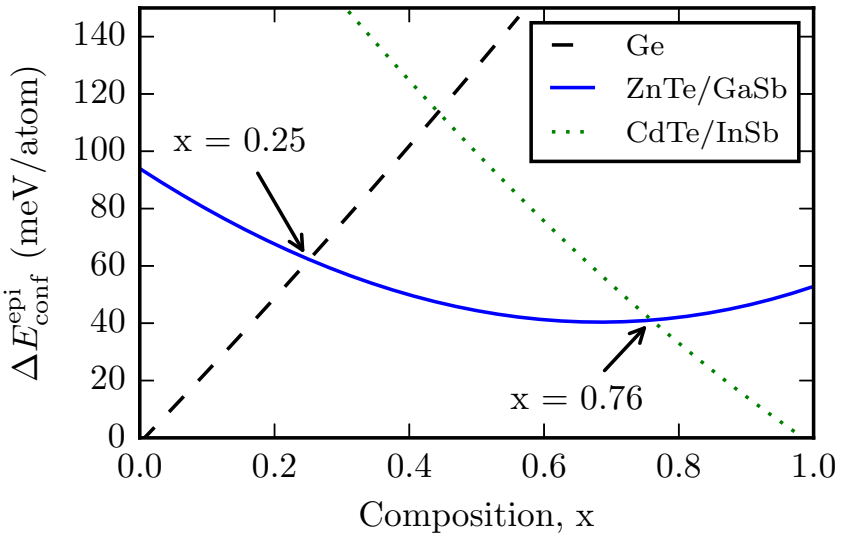

Figure 4.18: Formation energy of epitaxially grown $Ge_{1-x}Sn_x$ alloys with respect to decomposition into bulk components.

with CdTe/InSb substrates. This is likely due to the magnitude of strain exceeding the range at which CET is an effective approximation. Alloy compositions of x = 0.5 epitaxially strained to this substrate lattice parameter undergo 7.5% tensile strain, leading to anharmonic effects not accounted for in CET. This agreement sheds some light on the accuracy of the critical thickness model, the results of which will be presented in the subsequent section, and deformation potential theory, which will be discussed in the following chapter.

4.5.5 Critical thickness of epitaxially strained $Ge_{1-x}Sn_x$ alloys

As discussed in the previous chapter, the critical thicknesses of a material under strain allow us to assess the stability of a material grown on a lattice mismatched substrate. If the critical thickness of the material is lower than the threshold thickness for a band gap to emerge through quantum confinement, a thickness corresponding to a semimetallic film is not achievable on the given substrate. To compute the critical thickness t_c for $Ge_{1-x}Sn_x$ grown on Ge, ZnTe and CdTe

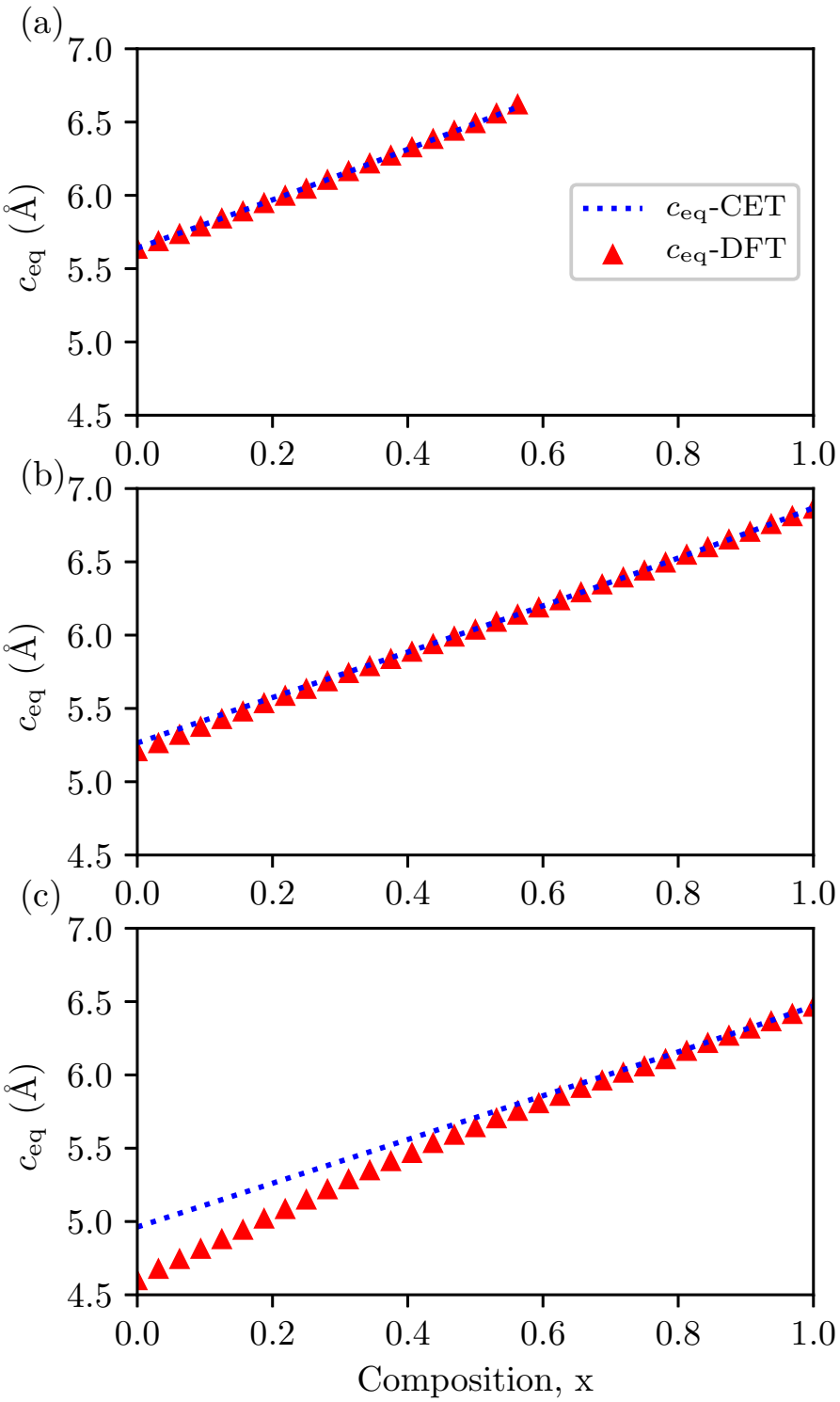

Figure 4.19: Out-of-plane equilibrium cell parameter c_{eq} for alloys grown on (a) Ge, (b) ZnTe/GaSb, and (c) CdTe/InSb, as calculated from SQS plus DFT/LDA and continuum elastic theory.

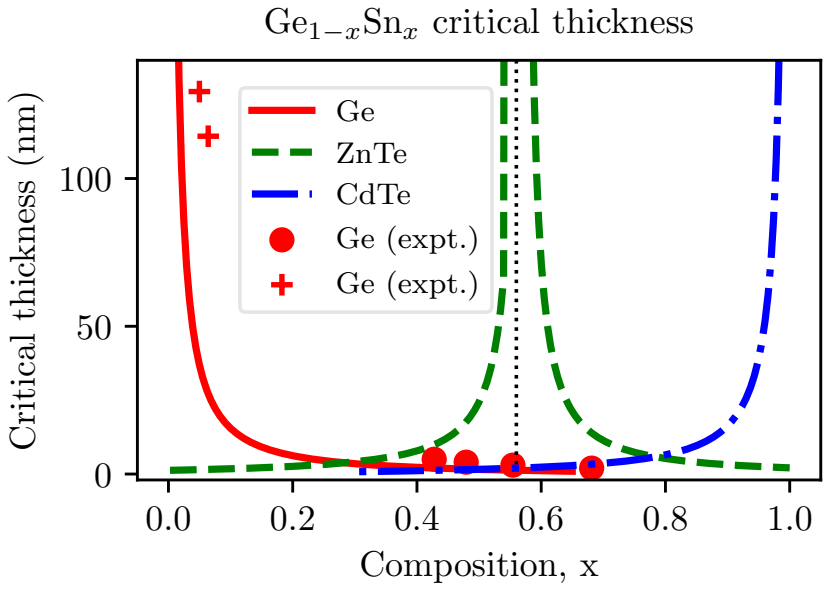

Figure 4.20: Calculated Sn composition-dependent critical thickness t_c of pseudomorphically strained $Ge_{1-x}Sn_x$ grown on [001]-oriented Ge (solid red line), ZnTe (dashed green line), or CdTe (dash-dotted blue line) substrates. Closed red circles denote the critical thicknesses inferred in Ref. [10] based on structural characterisation of $Ge_{1-x}Sn_x$/Ge epitaxial layers.

substrates the DFT-calculated lattice and elastic constants are employed, utilizing the bowing parameters presented previously in this chapter. The results of these calculations are shown in fig. 4.20. The critical thicknesses at $|\epsilon_{xx}| = 1\%$ are calculated in order to provide guideline strain-thickness limit estimations. The estimated strain-thickness limits are, respectively, $t_c \times |\epsilon_{xx}| = 22.8$ nm % and 24.4 nm % for $Ge_{1-x}Sn_x$ grown on Ge and CdTe. For $Ge_{1-x}Sn_x$/ZnTe, which is under compressive (tensile) in-plane strain for $x \gtrsim 0.54$ ($x \lesssim 0.54$), a strain-thickness limit $t_c \times |\epsilon_{xx}| = 23.3$ nm % (23.5 nm %) is estimated.

To compare the different substrates, we choose a reference critical thickness of 5 nm, as this is approximately the thickness for which a band gap begins to open for the fictitious system with a zero band gap and effectives masses corresponding to germanium, described in section 3.3.3. For $Ge_{1-x}Sn_x$/Ge, we compute that the critical thickness reduces to 5 nm for Sn composition $x = 0.234$, corresponding to an in-plane compressive strain of magnitude $|\epsilon_{xx}| = 3.4\%$. In section 4.5.1

we predicted based on LDA-calculated SQS total energies that it is energetically favourable for $Ge_{1-x}Sn_x$ to become amorphous for $x \gtrsim 0.56$. These $2\times2\times2$ simple cubic supercells have a thickness of $2 \times a(x) = 1.2$ nm, where $a(x)$ is the relaxed alloy lattice constant along [001]. Indeed, we calculate $t_c \leq 2\,a(x)$ for $x \geq 0.566$. This excellent quantitative agreement between DFT alloy SQS total energy calculations and the critical thickness method employed here provides confidence in our predicted strain-thickness limits for $Ge_{1-x}Sn_x$. We also compare our calculated $Ge_{1-x}Sn_x$/Ge critical thickness to experimental data which were estimated based on structural characterisation of $Ge_{1-x}Sn_x$/Ge epitaxial layers and measured elastic constants for Ge and α-Sn [10](closed red circles in fig. 4.20) and obtained from secondary ion mass spectrometry [44](red crosses in fig. 4.20). While our calculations slightly underestimate the experimental values, particularly at low Sn content, we note otherwise excellent qualitative agreement across the composition range for which data are available. It is likely that the increased critical thickness in the experimental data is brought about from non equilibrium effects creating kinetic barriers, preventing the formation of dislocations [45]. For $Ge_{1-x}Sn_x$/ZnTe we compute that t_c is reduced to 5 nm for $x = 0.334$ ($x = 0.808$), corresponding to a tensile (compressive) in-plane strain of magnitude $|\epsilon_{xx}| = 3.1\%$ ($|\epsilon_{xx}| = 3.4\%$). Finally, for tensile strained $Ge_{1-x}Sn_x$/CdTe, we compute $t_c = 5$ nm for $x = 0.759$, corresponding to a tensile in-plane strain of magnitude $|\epsilon_{xx}| = 2.8\%$. We therefore note that growing $Ge_{1-x}Sn_x$ on these three substrates allows $t_c \geq 5$ nm to be achieved across almost the entire composition range with the exclusion of a gap for $0.234 \leq x \leq 0.334$, corresponding to relaxed lattice constants in the range $a(x) \approx 5.84$ – 5.92 Å. Experimental data are not included for the ZnTe substrate, or the CdTe substrate. Utilizing ZnTe as a substrate for $Ge_{1-x}Sn_x$ is not common in the literature and as such there is no such critical thickness data. While there do exist experiments on high Sn content $Ge_{1-x}Sn_x$ films lattice matched to CdTe, obtaining the critical thickness is problematic as at a certain

thickness there is a thermodynamic phase transformation from α to β. As such it is difficult to ascertain whether there are dislocations, or whether the thickness limit is reached as a result of this phase change.

4.6 Conclusions

The lattice constants and bond lengths of the 64 atom $Ge_{1-x}Sn_x$ SQS cells are shown to match previously obtained experimental and theoretical work, thereby indicating consistency for the SQS approach to random alloy calculations for this work. The elastic constants calculated across the composition range for use in critical thickness and MST calculations are shown to exhibit significant alloy bowing. A study for the thermodynamic stability of GeSn alloys has been undertaken with models for both relaxed and pseudomorphic thick GeSn layers. A CE fit is performed and demonstrated to be capable of reproducing energies from DFT calculations for SQS across the full alloy composition range. From the CE, an asymmetry in the formation energies of random alloys as a function of alloy composition is identified, whereby introduction of Sn into Ge-rich alloys results in larger formation energies relative to the case of introducing Ge into Sn-rich alloys. A decomposition of the formation energy into a volume deformation, chemical, and relaxation terms reveals the volume deformation energy dominates the zero-temperature formation energies and drives immiscibility for these alloys with the chemical and relaxation energies serving to reduce the formation energies. Evaluation of free energy at finite temperatures reveals the configurational entropy dominates stabilising contributions, with vibrational terms contributing to a lesser extent, and the electronic contributions having a negligible impact in the temperature range of interest. CE fits describing configurational and temperature-dependent vibrational properties are employed to calculate the system's phase diagram using lattice Monte Carlo simulations. It

is shown that the critical temperature for stability of $Ge_{1-x}Sn_x$ alloys generally decreases at higher Sn compositions as a result of the aforementioned asymmetry in the formation energy versus composition. As well, vibrational terms introduce an opposing asymmetry in the phase diagram, whereby the stability of Ge-rich alloys is enhanced at finite temperatures due to the softening of phonon modes associated with incorporation of Sn into the lattice. The phase diagram identifies critical temperatures between the range of the melting temperatures for Sn and Ge for essentially the entire composition range, in good agreement with known experimental properties for bulk GeSn alloys. It should be noted that relaxation in thin films or nanowires can be enhanced by strain relaxation normal to the surfaces and can serve to stabilise nanostructures.

The influence of pseudomorphic growth on stability was considered by studying alloys biaxially strained along the (001)-orientation to the lattice spacing of substrates previously used for coherent epitaxial growth of $Ge_{1-x}Sn_x$, which provide lattice matching at compositions x=0, and approximately for x=0.5 and x=1. Analysis of the formation energies reveals that pseudomorphic growth enhances alloy stability by impeding coherent segregation, resulting in alloy stability even at zero temperature. Growth on ZnTe/GaSb substrates is predicted to provide the greatest epitaxial stabilisation across most of the composition range. Comparing pseudomorphic formation energies across substrates with respect to incoherent segregation reveals ZnTe/GaSb to be energetically favourable across approximately half of the composition range ($0.25 < x < 0.76$), with Ge (CdTe/InSb) substrates providing greater stability for $x < 0.25$ ($x > 0.76$). This result correlates with the calculations of thin film critical thicknesses using continuum elasticity theory.

Results presented in this work emphasise built-in strain to be the driver of immiscibility in $Ge_{1-x}Sn_x$ alloys. Strategies for stabilisation must thus be directed at

tackling this issue by balancing several complementary effects, such as relaxation normal to surfaces in nanostructures, by targeting Sn-rich compositions, and by choice of substrates that induce epitaxial stabilisation of alloys while delivering suitable critical thicknesses and electronic properties. In the context of materials engineering, selection of alloy composition, strain, film thickness (quantum confinement), and surface chemistry enable a wide range of options for the tailoring of the thermomechanical and electronic properties of GeSn alloys for technological applications.

References

[1] U. Mizutani, *Hume-Rothery Rules for Structurally Complex Alloy Phases*. Boca Raton: CRC Press, 2010.

[2] J. Piao, R. Beresford, T. Licata, W. Wang, and H. Homma. Molecular-beam epitaxial growth of metastable Ge_{1-x} Sn_x alloys. *Journal of Vacuum Science & Technology B: Microelectronics Processing and Phenomena*, vol. 8, no. 2, p. 221, 1990.

[3] F. Gencarelli, B. Vincent, J. Demeulemeester, A. Vantomme, A. Moussa, A. Franquet, A. Kumar, H. Bender, J. Meersschaut, W. Vandervorst, R. Loo, M. Caymax, K. Temst, and M. Heyns. Crystalline properties and strain relaxation mechanism of CVD grown GeSn. *ECS Journal of Solid State Science and Technology*, vol. 50, no. 9, p. 875, 2013.

[4] B. R. Conley, A. Mosleh, S. A. Ghetmiri, W. Du, R. A. Soref, G. Sun, J. Margetis, J. Tolle, H. A. Naseem, and S.-Q. Yu. Temperature dependent spectral response and detectivity of GeSn photoconductors on silicon for short wave infrared detection. *Optics Express*, vol. 22, p. 15639, 2014.

[5] S. Wirths, D. Buca, and S. Mantl. Si–Ge–Sn alloys: From growth to applications. *Progress in Crystal Growth and Characterization of Materials*, vol. 62, no. 1, p. 1, 2016.

[6] W. Dou, M. Benamara, A. Mosleh, J. Margetis, P. Grant, Y. Zhou, S. Al-

Kabi, W. Du, J. Tolle, B. Li, *et al.* Investigation of GeSn strain relaxation and spontaneous composition gradient for low-defect and high-Sn alloy growth. *Scientific Reports*, vol. 8, no. 1, p. 5640, 2018.

[7] L. Wei, Y. Miao, R. Pan, W. wei Zhang, C. Li, H. Lu, and Y.-F. Chen. Highly strained $Ge_{1-x}Sn_x$ alloy films with high Sn compositions grown by MBE. *Journal of Crystal Growth*, vol. 557, p. 125996, 2021.

[8] I. Dascalescu, N. C. Zoita, A. Slav, E. Matei, S. Iftimie, F. Comanescu, A.-M. Lepadatu, C. Palade, S. Lazanu, D. Buca, V. S. Teodorescu, M. L. Ciurea, M. Braic, and T. Stoica. Epitaxial GeSn obtained by high power impulse magnetron sputtering and the heterojunction with embedded GeSn nanocrystals for shortwave infrared detection. *ACS Applied Materials & Interfaces*, vol. 12, no. 30, p. 33879, 2020.

[9] Y.-C. Tai, P.-L. Yeh, S. An, H.-H. Cheng, M. Kim, and G.-E. Chang. Strain-free GeSn nanomembranes enabled by transfer-printing techniques for advanced optoelectronic applications. *Nanotechnology*, vol. 31, no. 44, p. 445301, 2020.

[10] A. Suzuki, O. Nakatsuka, S. Shibayama, M. Sakashita, W. Takeuchi, M. Kurosawa, and S. Zaima. Growth of ultrahigh-Sn-content $Ge_{1-x}Sn_x$ epitaxial layer and its impact on controlling Schottky barrier height of metal/Ge contact. *Japanese Journal of Applied Physics*, vol. 55, no. 4S, p. 04EB12, 2016.

[11] A. Sanchez-Soares, C. O'Donnell, and J. C. Greer. Electronic structure tuning via surface modification in semimetallic nanowires. *Physical Review B*, vol. 94, no. 23, p. 235442, 2016.

[12] R. Farrow, D. Robertson, G. Williams, A. Cullis, G. Jones, I. Young, and P. Dennis. The growth of metastable, heteroepitaxial films of α-Sn by metal

beam epitaxy. *Journal of Crystal Growth*, vol. 54, no. 3, p. 507, 1981.

[13] H. Höchst and I. Hernandez-Calderon. Angular resolved photoemission of InSb (001) and heteroepitaxial films of α-Sn (001). *Surface Science*, vol. 126, no. 1-3, p. 25, 1983.

[14] M. T. Asom, E. A. Fitzgerald, A. R. Kortan, B. Spear, and L. C. Kimerling. Epitaxial growth of metastable SnGe alloys. *Applied Physics Letters*, vol. 55, p. 578, 1989.

[15] P. John, T. Miller, and T.-C. Chiang. Core-level photoemission studies of the α-Sn/InSb (100) heterostructure system. *Physical Review B*, vol. 39, no. 5, p. 3223, 1989.

[16] R. C. Bowman, P. M. Adams, M. A. Engelhart, and H. Höchst. Structural characterization of α-Sn and α-$Sn_{1-x}Ge_x$ alloys grown by molecular beam epitaxy on CdTe and InSb. *Journal of Vacuum Science & Technology A: Vacuum, Surfaces, and Films*, vol. 8, p. 1577, 1990.

[17] M. P. Polak, P. Scharoch, and R. Kudrawiec. The electronic band structure of $Ge_{1-x}Sn_x$ in the full composition range: indirect, direct, and inverted gaps regimes, band offsets, and the Burstein–Moss effect. *Journal of Physics D: Applied Physics*, vol. 50, no. 19, p. 195103, 2017.

[18] P. Moontragoon, Z. Ikonić, and P. Harrison. Band structure calculations of Si–Ge–Sn alloys: Achieving direct band gap materials. *Semiconductor Science and Technology*, vol. 22, no. 7, p. 742, 2007.

[19] A. Sanchez-Soares, C. O'Donnell, and J. C. Greer, "Epitaxial stabilisation of $Ge_{1-x}Sn_x$ alloys." Unpublished.

[20] C. O'Donnell, A. Sanchez-Soares, C. A. Broderick, and J. C. Greer. Impact of stoichiometry and strain on $Ge_{1-x}Sn_x$ alloys from first principles calculations. *Journal of Physics D: Applied Physics*, vol. 54, no. 24, p. 245103, 2021.

[21] H. J. Monkhorst and J. D. Pack. Special points for Brillouin-zone integrations. *Physical Review B*, vol. 13, no. 12, p. 5188, 1976.

[22] A. Zunger, S.-H. Wei, L. G. Ferreira, and J. E. Bernard. Special quasirandom structures. *Physical Review Letters*, vol. 65, p. 353, 1990.

[23] K. Hass, L. Davis, and A. Zunger. Electronic structure of random $Al_{0.5}$ $Ga_{0.5}As$ alloys: Test of the "special-quasirandom-structures" description. *Physical Review B*, vol. 42, no. 6, p. 3757, 1990.

[24] A. van de Walle, P. Tiwary, M. De Jong, D. Olmsted, M. Asta, A. Dick, D. Shin, Y. Wang, L.-Q. Chen, and Z.-K. Liu. Efficient stochastic generation of special quasirandom structures. *Calphad*, vol. 42, p. 13, 2013.

[25] A. van de Walle and G. Ceder. Automating first-principles phase diagram calculations. *Journal of Phase Equilibria*, vol. 23, no. 4, p. 348, 2002.

[26] M. Stone. Cross-validatory choice and assessment of statistical predictions. *Journal of the Royal Statistical Society: Series B (Methodological)*, vol. 36, p. 111, 1974.

[27] R. Beeler, R. Roucka, A. V. G. Chizmeshya, J. Kouvetakis, and J. Menéndez. Nonlinear structure-composition relationships in the $Ge_{1-y}Sn_y$/Si(100) (y<0.15) system. *Physical Review B*, vol. 84, p. 035204, 2011.

[28] E. J. O'Halloran, C. A. Broderick, D. S. P. Tanner, S. Schulz, and E. P. O'Reilly. Comparison of first principles and semi-empirical models of the structural and electronic properties of $Ge_{1-x}Sn_x$ alloys. *Optical and Quantum Electronics*, vol. 51, p. 314, 2019.

[29] F. Gencarelli, D. Grandjean, Y. Shimura, B. Vincent, D. Banerjee, A. Vantomme, W. Vandervorst, R. Loo, M. Heyns, and K. Temst. Extended X-ray absorption fine structure investigation of Sn local environment in strained

and relaxed epitaxial $Ge_{1-x}Sn_x$ films. *Journal of Applied Physics*, vol. 117, p. 095702, 2015.

[30] L. He, F. Liu, G. Hautier, M. J. T. Oliveira, M. A. L. Marques, F. D. Vila, J. J. Rehr, G.-M. Rignanese, and A. Zhou. Accuracy of generalized gradient approximation functionals for density-functional perturbation theory calculations. *Physical Review B*, vol. 89, no. 6, p. 064305, 2014.

[31] N. Bouarissa and F. Annane. Electronic properties and elastic constants of the ordered $Ge_{1-x}Sn_x$ alloys. *Materials Science and Engineering: B*, vol. 95, p. 100, 2002.

[32] W. Weber. Adiabatic bond charge model for the phonons in diamond, Si, Ge, and $\alpha - Sn$. *Physical Review B*, vol. 15, p. 4789, 1977.

[33] D. L. Price, J. M. Rowe, and R. M. Nicklow. Lattice dynamics of grey tin and indium antimonide. *Physical Review B*, vol. 3, p. 1268, 1971.

[34] G. Nilsson and G. Nelin. Phonon dispersion relations in Ge at 80° K. *Physical Review B*, vol. 3, p. 364, 1971.

[35] É. Bouthillier, S. Assali, J. Nicolas, and O. Moutanabbir. Decoupling the effects of composition and strain on the vibrational modes of GeSn semiconductors. *Semiconductor Science and Technology*, vol. 35, p. 095006, 2020.

[36] R. W. Olesinski and G. J. Abbaschian. The Ge-Sn (germanium-tin) system. *Bulletin of Alloy Phase Diagrams*, vol. 5, no. 3, p. 265, 1984.

[37] A. Gassenq, L. Milord, J. Aubin, N. Pauc, K. Guilloy, J. Rothman, D. Rouchon, A. Chelnokov, J. M. Hartmann, V. Reboud, and V. Calvo. Raman spectral shift versus strain and composition in GeSn layers with 6%–15% sn content. *Applied Physics Letters*, vol. 110, p. 112101, 2017.

[38] C. Xu, P. M. Wallace, D. A. Ringwala, S. L. Y. Chang, C. D. Poweleit, J. Kouvetakis, and J. Menéndez. Mid-infrared (3–8 μm) $Ge_{1-y}Sn_y$ alloys (0.15<y<0.30): Synthesis, structural, and optical properties. *Applied Physics Letters*, vol. 114, p. 212104, 2019.

[39] D. M. Wood and A. Zunger. Epitaxial effects on coherent phase diagrams of alloys. *Physical Review Letters*, vol. 61, no. 13, p. 1501, 1988.

[40] A. Zunger and D. Wood. Structural phenomena in coherent epitaxial solids. *Journal of Crystal Growth*, vol. 98, p. 1, 1989.

[41] V. Ozoliņš, C. Wolverton, and A. Zunger. Effects of anharmonic strain on the phase stability of epitaxial films and superlattices: Applications to noble metals. *Physical Review B*, vol. 57, no. 8, p. 4816, 1998.

[42] C. A. Hoffman, J. R. Meyer, R. J. Wagner, F. J. Bartoli, M. A. Engelhardt, and H. Höchst. Three-band transport and cyclotron resonance in α-Sn and α-$Sn_{1-x}Ge_x$ grown by molecular-beam epitaxy. *Physical Review B*, vol. 40, no. 17, p. 11693, 1989.

[43] E. Calavita, M. A. Engelhart, and Höchst, Heteroepitaxy of strained metastable α – Sn films. in *The Physics of Semiconductors: Proceedings of the 20th International Conference*, 1990.

[44] H. V. Stanchu, A. V. Kuchuk, Y. I. Mazur, J. Margetis, J. Tolle, S.-Q. Yu, and G. J. Salamo. Strain suppressed Sn incorporation in GeSn epitaxially grown on Ge/Si(001) substrate. *Appl. Phys. Lett.*, vol. 116, no. 23, p. 232101, 2020.

[45] F. Gencarelli, B. Vincent, J. Demeulemeester, A. Vantomme, A. Moussa, A. Franquet, A. Kumar, H. Bender, J. Meersschaut, W. Vandervorst, R. Loo, M. Caymax, K. Temst, and M. Heyns. Crystalline properties and strain

relaxation mechanism of CVD grown GeSn. *ECS Transactions*, vol. 50, no. 9, pp. 875–883, 2013.

Chapter 5

Engineering the semiconducting to semimetallic transition in $Ge_{1-X}Sn_X$ alloys via strain

5.1 Introduction

In this chapter the electronic structure of $Ge_{1-x}Sn_x$ alloys is investigated across the full alloy composition range, including the impact of strain on the electronic band gap. Previous theoretical investigations of the $Ge_{1-x}Sn_x$ electronic structure spanning the full composition range have revealed the evolution of the alloy from being an indirect-gap semiconductor ($x \lesssim 0.1$), to a direct-gap semiconductor ($0.1 \lesssim x \lesssim 0.2$), and a semimetal ($x \gtrsim 0.2$) [1–3]. The evolution of the alloy band gap suggests broad scope to exploit a combination of alloying (α-Sn incorporation in Ge) and strain (choice of substrate) to engineer the semiconducting to semimetallic transition in $Ge_{1-x}Sn_x$ alloys.

Previous theoretical calculations have identified the semiconducting to semimetallic transition as occurring for Sn compositions x in the range of 0.2 to 0.4 in

unstrained alloys [1–3]. However, due to the low solid solubility of Sn in Ge, [4] growth of $Ge_{1-x}Sn_x$ alloys with sufficiently high Sn compositions to bring about a semimetallic band structure is challenging. Recent investigations have demonstrated that this limitation can be overcome with non-equilibrium growth conditions, allowing higher Sn compositions to be achieved in nanostructure growth than in the growth of bulk-like epitaxial layers [5–8]. Sn incorporation has been demonstrated to correlate with thickness in thin film growth, with high Sn compositions $x \approx 0.46$ achieved via growth of films having thickness of ≈ 3 nm [6].

Though the previous chapter indicates that growth on a lattice-matched substrate enhances miscibility, growth of strained $Ge_{1-x}Sn_x$ thin films can be exploited to reduce the Sn composition required to induce a semiconducting to semimetallic transition. Application of tensile strain has been predicted to induce an indirect to direct band gap transition in Ge [9–11]. While, in theory, application of high tensile strain could induce a semiconducting to semimetallic transition in Ge, the required strains, corresponding to $\approx 4.5\%$ lattice-mismatch, as presented in chapter 3 for a pseudomorphically strained, (001)-oriented epitaxial layer, are sufficiently large that critical thickness limitations would impede growth. This strain requirement is reduced by Sn incorporation, suggesting the possibility to simultaneously exploit Sn composition and strain to engineer the semiconducting to semimetallic transition.

Sections of this chapter have been published [12].

5.2 Computational details

Special quasirandom structures (SQSs) are again implemented within density functional theory (DFT) in order to calculate alloy properties. Structural relaxations are carried out in the local density approximation (LDA) [13] in the

same manner as the previous chapter, employing the same s4p4d3f2 basis set for germanium and s2p3d3f2 basis set for tin. The density of the employed Monkhorst-Pack grid is again at least 7 k-points/Å, and the corresponding energy cut-off is at least 100 Ha. The electronic structure calculations are performed using the TB09 meta-GGA (Tran-Blaha modified Becke-Johnson LDA) exchange-correlation functional [14], as in chapter 3, in order to overcome the band gap underestimation inherent in the LDA. To simulate $Ge_{1-x}Sn_x$ alloy supercells the Becke-Roussel mixing parameter c is interpolated as:

$$c(x) = \frac{(1-x)\Omega_{Ge}c_{Ge} + xc_{Sn}\Omega_{Sn}}{(1-x)\Omega_{Ge} + x\Omega_{Sn}}, \tag{5.1}$$

where Ω_{Sn} and Ω_{Ge} are the equilibrium volumes of the α-Sn and Ge primitive unit cells, respectively. This interpolation scheme interpolates between the values of c_{Ge} and c_{Sn} based on the fraction of the total volume each element occupies in a $Ge_{1-x}Sn_x$ alloy supercell, reflecting the extended nature of exchange-correlation effects in terms of the difference in covalent radius between Ge and Sn. Due to the large relativistic effects associated with Sn, the electronic structure calculations explicitly include spin-orbit coupling.

The same 64 atom SQS simulation cells are utilized as in the previous chapter, targeting disordered-state pair and triplet correlations with a range up to one nanometre. These cells are relaxed in the same manner as the previous chapter and to the same tolerances. To simulate epitaxial growth of $Ge_{1-x}Sn_x$ layers, pseudomorphic strain is applied in the same manner as the previous chapter: by restricting the lattice constant in the plane perpendicular to the growth direction to be equal to that of the chosen substrate material, and allowing the lattice constant to relax along the growth direction. The internal atomic degrees of freedom (ionic positions) are allowed to relax freely so as to minimise the lattice free energy [15].

5.3 Overcoming band folding in supercells

The use of disordered alloy supercells results in (i) local relaxation of the crystal lattice, which breaks the underlying cubic symmetry of the diamond structure and hence lifts band degeneracies present at high-symmetry points in the band structures of Ge and α-Sn [16, 17], and in (ii) folded electronic band structures, due to the reduced size of the supercell Brillouin zone compared to that associated with a primitive unit cell. These factors complicate interpretation of the alloy electronic structure. To overcome these limitations and track the evolution of the CB and VB edge states in disordered alloy supercells, overlaps between alloy states and selected states of unperturbed Ge_{64} supercells are calculated. This approach, which is similar to the computation of the spectral function (at a single k-point) employed in popular zone unfolding schemes, enables the evolution of both the energy and character of the alloy band edge states to be identified and tracked in a quantitative manner [18].

An example of this analysis is presented in fig. 5.1 for a $Ge_{48}Sn_{16}$ (x= 0.25) SQS. The left-hand panel in fig. 5.1 shows the folded supercell band structure, while the right-hand panel shows the (squared) overlaps calculated by projecting the zone-centre CB edge (Γ_7^-), heavy-hole (HH) and light-hole (LH) VB edge (Γ_8^+), and spin-orbit split-off (SO) VB edge (Γ_8^+) states of a Ge_{64} supercell on to the full spectrum of $Ge_{48}Sn_{16}$ alloy supercell zone centre states. This allows the identification of (i) the Ge Γ_7^- CB edge character residing primarily on two supercell states, reflecting Sn-induced alloy band mixing which transfers direct (Ge Γ_7^-) character to the hybridised alloy CB edge [19], (ii) SO band edge remaining comparatively unperturbed for x $\approx$ 0.25, reflecting that for low x, Sn incorporation tends primarily to impact the CB structure [3, 19, 20], and (iii) splitting in energy and hybridisation of the LH- and HH-like VB edge states, reflecting a loss of cubic symmetry due to short-range alloy disorder and associated local relaxation

of the crystal lattice [18]. In the presence of pseudomorphic strain the biaxial component of the strain further reduces the lattice symmetry, acting to push HH-like states upwards and the LH-like downwards in energy in the presence of compressive in-plane strain, and vice-versa for tensile strain (as described in section 2.5.2). Despite short-range alloy disorder driving hybridisation between HH- and LH-like VB states it is generally found, as expected for a pure (unalloyed) semiconductor such as Ge, that the state at the alloy Fermi level possesses more Ge HH Γ_8^+ character in the presence of compressive in-plane strain, and more Ge LH Γ_8^+ character in the presence of tensile in-plane strain (eq. (2.44) and eq. (2.45), respectively).

The presence of reduced lattice symmetry and alloy-induced hybridisation complicates interpretation of the alloy electronic structure. Generally no single alloy supercell state possesses, for example, 100% Γ_7^- or Γ_8^+ character. To identify an appropriate Γ_7^--Γ_8^+ energy gap in these calculations, the lowest energy supercell state possessing appreciable Ge Γ_7^- character, and the highest energy supercell state possessing appreciable Ge Γ_8^+ character, are selected as the conduction and valence band, respectively. In the case of semiconducting $Ge_{1-x}Sn_x$ ($x \lesssim 0.2$), this identifies the fundamental band gap, while for higher Sn compositions it identifies the maximum *inverted* energy gap that must be overcome by quantum confinement to open up a direct band gap above the Fermi level. For reference, calculated overlaps for relaxed (unstrained) and pseudomorphically strained $Ge_{1-x}Sn_x$ SQSs are provided as fig. 5.2.

5.4 Bulk $Ge_{1-x}Sn_x$ band gaps

A key parameter for the assessment of the suitability of a material for optoelectronics and electronics is the band gap. Germanium has been shown to have

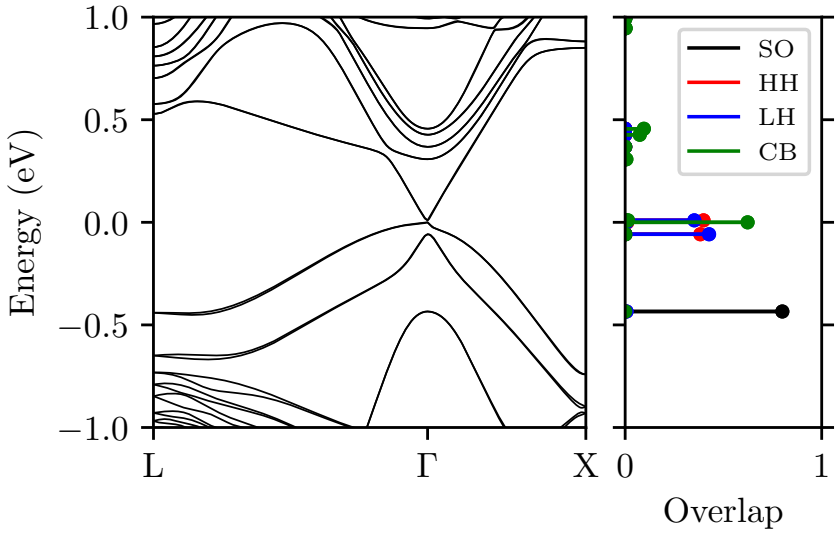

Figure 5.1: Left-hand pane: meta-GGA DFT-calculated band structure of a $Ge_{48}Sn_{16}$ (x = 0.25) SQS. Right-hand pane: calculated squared overlaps between the alloy SQS zone centre states and the SO (Γ_7^-, solid black lines), HH (Γ_8^+, solid red lines), LH (Γ_8^+, solid blue lines), and CB (Γ_7^-, solid green lines) states of a pure (Sn-free) Ge_{64} supercell.

an indirect gap (L - Γ_8^+), while α-Sn has been shown to have a *negative*, direct, optical gap (Γ_7^- - Γ_8^+). α-Sn exhibits a vanishing density of states at the Fermi level and is thus characterised as a semimetal. This is due to the negative Γ_7^- - Γ_8^+ energy difference, known as the *inverted* band gap. α-Sn has previously been predicted to have suitable electronic properties for semimetal devices [21–23]. This is made possible by the ability for a band gap to be induced in α-Sn through quantum confinement, when the Γ_7^- state is raised above the Γ_8^+ state [24], which was demonstrated in section 3.3.3. As such, depending on confinement direction, it is evident for a band gap to be induced through confinement, a $Ge_{1-x}Sn_x$ alloy with a zero Γ_7^- - Γ_8^+ energy difference must overcome a smaller energy separation than that of α-Sn. This indicates that a band gap would be induced at larger film thicknesses at a composition where these states are degenerate, dependent on the effective masses and the direction of confinement. It follows that Γ_7^- - Γ_8^+ energy difference is an important factor to take into consideration when designing semimetallic $Ge_{1-x}Sn_x$ devices.

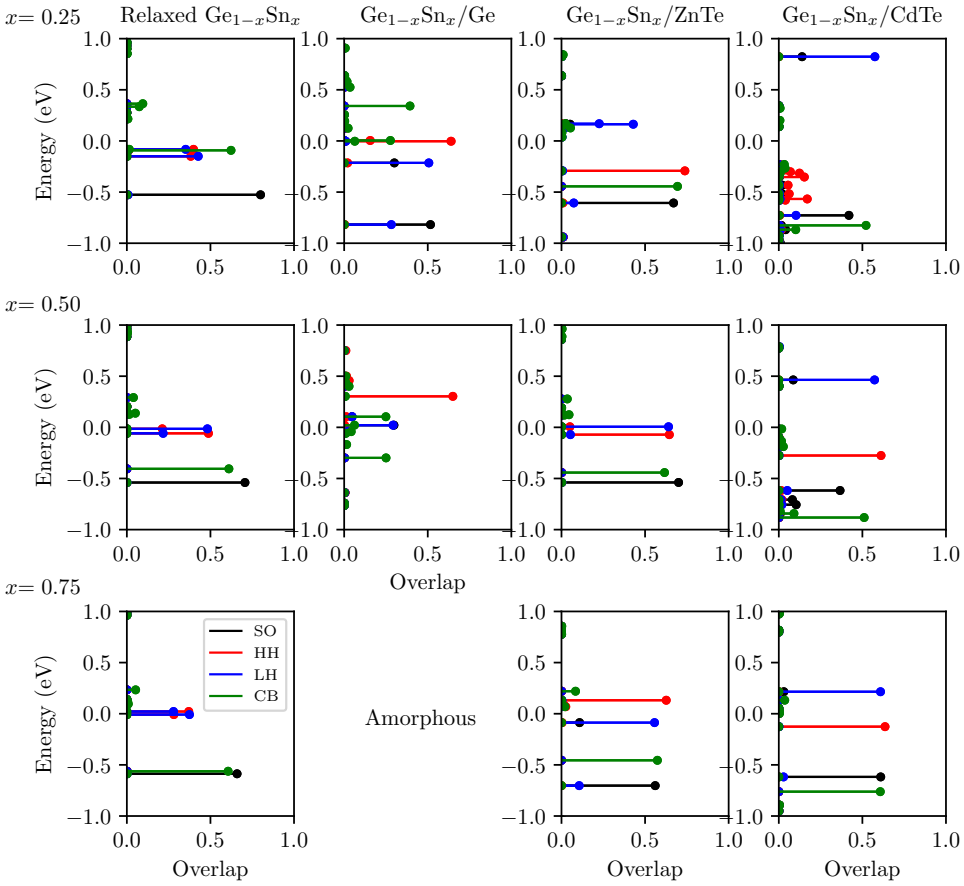

Figure 5.2: Calculated squared overlaps between the alloy SQS zone centre states and the SO (Γ_7^-, solid black lines), HH (Γ_8^+, solid red lines), LH (Γ_8^+, solid blue lines), and CB (Γ_7^-, solid green lines) states of a Ge_{64} supercell. Columns indicate alloy substrate (Relaxed, Ge, ZnTe and CdTe) and rows indicate alloy composition ($x = 0.25, 0.5$ and 0.75).

Previous theoretical calculations have predicted the evolution and nature of the $Ge_{1-x}Sn_x$ alloy band gap across the full composition range from Ge to α-Sn [1, 3, 25]. Beginning with the indirect-gap semiconductor Ge, Sn incorporation drives rapid band gap reduction and an indirect- to direct-gap transition for x $\lesssim 0.1$. Beyond this composition, the direct band gap decreases in magnitude until it closes for x ≈ 0.21, at which point the alloy becomes a zero-gap semimetal possessing an *inverted* Γ_7^--Γ_8^+ state ordering. Throughout the remainder of the composition range the alloy band structure remains semimetallic. TB-mBJ DFT calculations have been employed to verify the evolution of the $Ge_{1-x}Sn_x$ band gap, using unstrained 64-atom SQSs in which all lattice vectors and ionic coordi-

nates are freely relaxed, as described in section 5.2. This is presented in fig. 5.3, closed red circles denote the calculated fundamental alloy band gap. The solid black line shows the corresponding fundamental band gap calculated via a cluster expansion approach [26], allowing for prediction of alloy properties as though the SQS lattice correlation functions correspond exactly to those of truly statistically random substitutional alloys. This cluster expansion approach is based on that employed in the previous chapter for 64 atom SQSs. To obtain this CE, the band gaps of the relaxed bulk $Ge_{1-x}Sn_x$ SQSs are fit to the quasirandom correlations functions present in the cells, as described in section 2.4.2. This is then used to predict the band gap for fully random correlation functions, in order to get a smooth band gap curve. The dashed black line in fig. 5.3 denotes zero band gap, highlighting the semiconducting to semimetallic transition, with negative values referring to an *inverted* (negative) $\Gamma_7^- - \Gamma_8^+$ energy gap.

At low Sn compositions $x \lesssim 0.21$, a rapid band gap reduction with increasing x is calculated (discussion of the indirect- to direct-gap transition in this composition range is postponed until section 5.7.1). The calculated band gaps are also compared to experimental measurements in fig. 5.3. Generally, $Ge_{1-x}Sn_x$ is grown as a thin strained, or thick relaxed, epitaxial layer on a substrate having a lattice constant close to that of Ge. The resultant pseudomorphic strain complicates comparison between calculated and measured band gaps, due to the impact of strain on the magnitude of the band gap, as described in section 2.5.2. In fig. 5.3 the results of the TB-mBJ DFT calculations are compared to experimental data in which the impact of pseudomorphic strain is minimised. Specifically, our calculations are compared to the results of photo-modulated reflectance (Ref. [27]; open green triangles) and optical absorption (Refs. [28] and [29]; open pink triangles and blue squares, respectively) spectroscopic measurements. The photo-modulated reflectance measurements of Ref. [27] were performed on epitaxial layers grown on nominally lattice-matched $In_yGa_{1-y}As$ buffer layers, so that strain

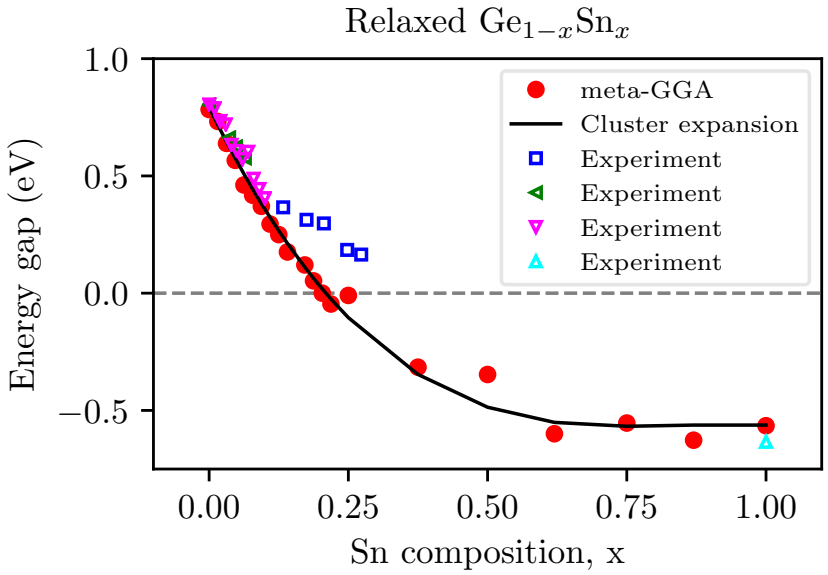

Figure 5.3: Meta-GGA DFT-calculated band gap as a function of Sn composition x of $Ge_{1-x}Sn_x$ alloy SQSs across the full alloy composition range. The solid black line represents the corresponding cluster expansion calculation. Open green triangles, pink triangles, and blue squares denote measured low temperature band gaps in the semiconducting regime [27–29], and the light blue triangle denotes the experimentally measured inverted gap of α-Sn [30]. The horizontal dashed line denotes zero band gap, demarcating between semiconducting and semimetallic band structure.

should be minimised. The absorption measurements of Ref. [28] were performed on strained $Ge_{1-x}Sn_x$ epitaxial layers, but the data were then corrected to account for the strain-induced change to the band gap, based on strain values extracted from x-ray diffraction measurements. The absorption measurements of Ref. [29] were performed on thick, relaxed epitaxial layers grown on Si substrates. Excellent quantitative agreement between the calculated band gap evolution and that measured by Lin et al. [27] and by Tran et al. [28] is noted. However, our calculations deviate from the measurements of Xu et al. [29] for $0.15 \lesssim x \lesssim 0.25$. While spectroscopic ellipsometry (SE) measurements have been shown to be accurate in the past, agreeing with photoluminescence measurements of SiGeSn samples to within ≈ 30 meV [31], it is possible that the disagreement between the calculated and experimental results are caused by experimental factors. Firstly, given the large lattice mismatch between $Ge_{1-x}Sn_x$ and the Si substrates employed by Xu

et al., it is possible that there remains residual compressive strain associated with partial relaxation in these samples, which would act to increase the band gap, potentially explaining why our calculations underestimate the measured band gaps for these samples. Secondly, it is possible that inaccuracy is introduced when fitting the raw SE data, however no information on the estimated error of the fits is given. Another area of uncertainty mentioned in this study is brought about by the not fully understood line shape present in the direct band gap transition of α-Sn, which would have more of an impact in obtaining transitions for high Sn content alloys. It is also possible that the disagreement is as a result of assumptions made in the theoretical model. For example, if the alloy structures are not truly random and were to exhibit some short range ordering, this would increase the band gap by $\approx$ 100 meV [32]. However, it is of note that the calculations that predicted this short range order were conducted for room temperature, whereas the growth of the experimental films was conducted between 545 K and 590 K, and as such short range order would be drastically decreased at these higher temperatures. The closed light-blue triangle represents the α-Sn *inverted* direct Γ_7^--Γ_8^+ energy gap, measured by Booth and Ewald [30] via magnetoresistance. Overall good agreement between our theoretical calculations and comparable experimental data is noted.

The unstrained $Ge_{1-x}Sn_x$ band gap is predicted to close for $x \approx 0.21$. Analysis of the alloy supercell electronic structure for SQSs having $x \gtrsim 0.21$ demonstrates vanishing DOS at the Fermi level, verifying that the alloy remains semimetallic for $0.21 \lesssim x \leq 1$, in agreement with recent theoretical calculations [3, 25]. For Sn compositions $x \gtrsim 0.5$ it is predicted that the magnitude of the *inverted* Γ_7^--Γ_8^+ energy gap remains close to the value −0.589 eV calculated for α-Sn (given on table 3.2). There are, however, divergent predictions in the literature regarding the precise nature of the semimetallic band structure for $x \gtrsim 0.2$. Using empirical pseudopotential calculations in the virtual crystal approximation, Lan et al. [25]

predicted that the band ordering remains topological in this composition range, i.e. with Γ_7^- states respectively lying lower and higher in energy than Γ_8^+ and Γ_7^+ states. Conversely, by applying zone unfolding to DFT calculations for SQS supercells, Polak et al. [3] predicted the presence of a non-topological *inverted SO* band structure for $0.45 \lesssim x \lesssim 0.85$, in which the Γ_7^- states drop below the Γ_7^+ states in energy. However, it is noteworthy that the quadratic composition dependent band gap fit applied by Polak et al. to extract this conclusion is poorer in quality for $x \gtrsim 0.3$ compared to its accuracy at lower Sn compositions.

To resolve these conflicting predictions, a direct analysis of the alloy supercell zone-centre states has been undertaken, via projection onto reference Γ_7^-, Γ_8^+, and Γ_7^+ states calculated for an unperturbed, Sn-free Ge_{64} supercell as described in section 5.2. Applying this quantitative approach, it is found that the alloy state retaining the largest calculated Γ_7^- character reduces in energy with increasing x, approaching the state retaining the largest calculated Γ_7^+ character. At $x = 0.625$ ($Ge_{24}Sn_{40}$ SQS) it is calculated that these Ge Γ_7^-- and Γ_7^+-derived alloy states become approximately degenerate, remaining so for higher Sn compositions up to $x = 0.875$ (Ge_8Sn_{56} SQS), beyond which composition the relative energy of the Ge Γ_7^--derived alloy state increases to reach its value in α-Sn (i.e. lying ≈ 100 meV above Γ_7^+ in energy). In only one of the supercells analysed was a Ge Γ_7^--derived alloy state found to lie lower in energy than a Γ_7^+-derived state, and in that case did so by only 10 meV. Our calculations therefore suggest that $Ge_{1-x}Sn_x$ most likely retains topological band ordering for $0.2 \lesssim x \leq 1$, but it is noted that the specific band ordering close to $x = 0.6$ in small supercell calculations is determined in part by the impact on alloy-induced band hybridisation of the precise alloy disorder and lattice relaxation present in a given disordered alloy supercell.

Deviations between previous predictions are attributed to the simplified manner in which the alloy band structure was analysed, generally based on either (i)

assumed virtual crystal-like behaviour and simple polynomial fits to composition-dependent band gaps obtained from theoretical data, or (ii) extrapolation of low x experimental data across the full composition range. In particular, large uncertainties associated with extrapolation of experimental data have produced divergent predictions, including [29] (i) that the magnitude of the *inverted* Γ_7^--Γ_8^+ alloy energy gap exceeds that of α-Sn by up to 0.2 eV [3], or (ii) that the direct Γ_7^--Γ_8^+ band gap remains open and of a constant magnitude ≈ 0.1 eV up to $x \approx 0.7$. Conversely, emphasis is placed on the fact that our conclusions are based on direct interrogation of the character and evolution of hybridised alloy supercell eigenstates calculated from first principles and without simplifying approximations.

From fig. 5.3, the Γ_7^- - Γ_8^+ energy gap can be seen to not decrease below the value for α-Sn. It follows that alloys of composition above $x \approx 0.21$ would be suitable in the creation of confinement modulated semimetal devices, as a similar energy would need to be overcome by confinement to induce a gap. By keeping the tin content as low as possible to avoid immiscibility, but above this threshold, band gaps can be realized at larger thicknesses as there is less of a negative energy difference to overcome with confinement.

5.5 Electronic structure evolution in pseudomorphically strained SQSs

Strain allows for another parameter, aside from composition, that can be modified to modulate the Γ_7^- - Γ_8^+ energy gap. Previously the effect of compressive strain has been shown on the band gap of $Ge_{0.83}Sn_{0.17}$ alloys [33]. This study has shown that when compressive strain imparted by a Ge virtual substrate is relaxed via releasing them from the substrate via patterning as microdisks. The in-plane biaxial compressive strain, measured from reciprocal space mapping, was

given as -1.3% for the as grown samples, and as −0.2% in the microdisks. The reduction in compressive strain is observed to cause a decrease in the band gap of approximately 50 meV.

By epitaxially straining the 64 atom bulk SQSs, epitaxially coherent films constrained to a substrate lattice parameter are approximated, as in the previous chapter. The same lattice parameters are utilized: Ge (5.64 Å), ZnTe (6.1 Å), and CdTe (6.48Å). These substrates allow for an insight into how the energy gap of random $Ge_{1-x}Sn_x$ alloys are modified by compressive strain (germanium, up to 15% tensile strain) and tensile strain (tin, up to 15% tensile strain), and an intermediary lattice parameter (ZnTe). The Γ_7^- - Γ_8^+ energy differences for these cells are then calculated, in a similar manner to the unstrained cells.

The Γ_7^- - Γ_8^+ energy differences are displayed in fig. 5.4. There are two effects at work in these cells. Strain works to decrease or increase the Γ_7^- - Γ_8^+ energy difference, depending on whether it is tensile or compressive strain, respectively, consistent with the pure germanium and α-tin calculations in chapter 3. Alloying also affects the gap, as incorporating more tin lowers the gap, as observed in relaxed structures.

Comparing the calculated relaxed $Ge_{1-x}Sn_x$ cells and the cells compressively strained to the Ge lattice constant in fig. 5.4, it is noted that the latter closely track the former for $x \lesssim 0.3$. The strained $Ge_{1-x}Sn_x$/Ge band gaps are calculated to slightly exceed those of relaxed $Ge_{1-x}Sn_x$ in this composition range, reflecting that compressively pseudomorphic strain acts to increase the band gap, as demonstrated in chapter 3. As the Sn composition is increased above 0.3, it is noted that the calculated magnitude of the *inverted* Γ_7^--Γ_8^+ energy gap of strained $Ge_{1-x}Sn_x$/Ge exceeds that in relaxed $Ge_{1-x}Sn_x$, i.e. the Ge Γ_7^--derived alloy state is lower in energy relative to the Ge Γ_8^+-derived state that defines the alloy Fermi level. This is contrary to the expected trend based on the compressive strain

present in these two $Ge_{1-x}Sn_x$/Ge SQSs. Based on the analysis of the character of the eigenstates in these two SQSs (as seen in fig. 5.2), this unusual behaviour is attributed to alloy-induced hybridisation, which distributes Ge Γ_7^- character over an energy range $\lesssim 1$ eV in width. Computing the weighted average energy of the supercell eigenstates, using the computed Ge Γ_7^- character of each state as the weight for that state's energy, reverses this trend and leads to $Ge_{1-x}Sn_x$/Ge *inverted* band gaps which are smaller in magnitude than in relaxed $Ge_{1-x}Sn_x$, as expected.

The cells epitaxially constrained to the lattice spacing of CdTe substrate exhibit a significant negative energy separation between the Γ_7^- - Γ_8^+ states over the composition range. This indicates that the tensile strain, applied by incorporating germanium into the alloy on this substrate, overcomes the effect of reducing the tin content in the cell. As a result, overall the Γ_7^- and Γ_8^+ energy difference decreases as the tin content is reduced. As such the magnitude of the *inverted* band gap increases to below that of α-Sn, causing the opening of a band gap through quantum confinement to become more challenging. Constraining the cells epitaxially to the ZnTe lattice constant is shown to cause a similar energy separation of the Γ_7^- and Γ_8^+ states to α-Sn across the composition range. As such, this presents the possibility of similar band gaps brought about by confinement, dependent on the curvature of the bands and other surface effects, such as interactions with the substrate and termination used on the film [22]. It is important to note that as these strained cells are comprised of the same SQSs as those in section 5.4, the same fluctuations brought about by the periodicity and specific correlation functions present in the relaxed calculations are also present in the strained calculations. Also, while we assume randomness in these simulation cells, it is possible that short range order could be exhibited if these cells are fabricated at low enough growth temperatures [32]. As well as this, utilizing $\lesssim 10^2$-atom supercells limits the number of states that can hybridise as a result

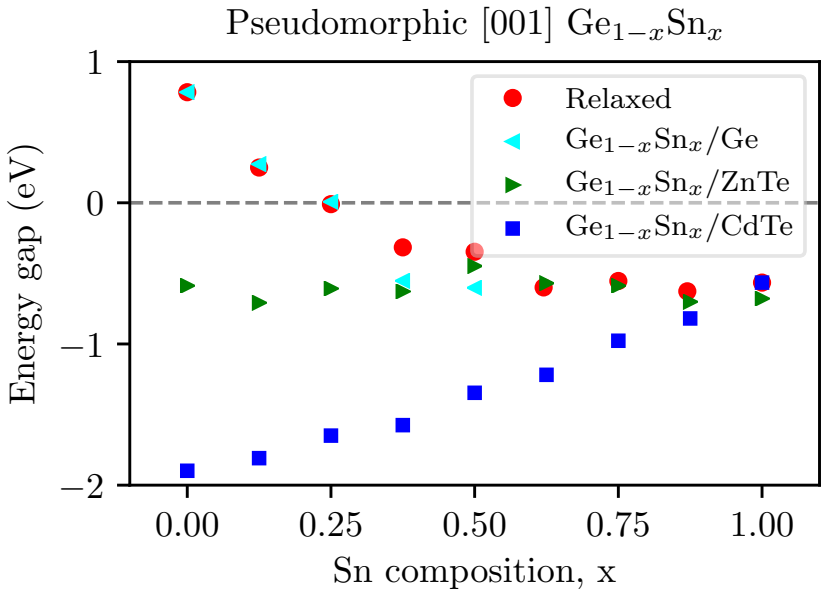

Figure 5.4: Lowest energy gap (the L - Γ_8^+ or the Γ_7^- - Γ_8^+ gap) across the full composition range for $Ge_{1-x}Sn_x$ alloys epitaxially strained to the Ge, ZnTe, and α-Sn lattice constants.

of alloying. As such, the observed Sn-induced Γ-L band mixing observed in the conduction band persists across the entire composition range as a result of the supercell size [34].

5.6 Effect of tensile strain on the alloy band gap

Due to the critical thickness limiting the dimensions at which the above alloys could be fabricated on the suggested substrates, knowledge of the least amount of strain and tin content required for the semiconducting to semimetallic transition is of importance when designing devices. By employing tensile strain, the amount of tin required is reduced, thus reducing possible segregation during growth. However, the critical thickness is lowered by the applied tensile strain.

The composition at which the band gap of $Ge_{1-x}Sn_x$ vanishes, becoming semimetallic, has been calculated across a tensile strain range from 0% to 4% strain. This is presented in fig. 5.5(a). The data were obtained by calculating the lowest

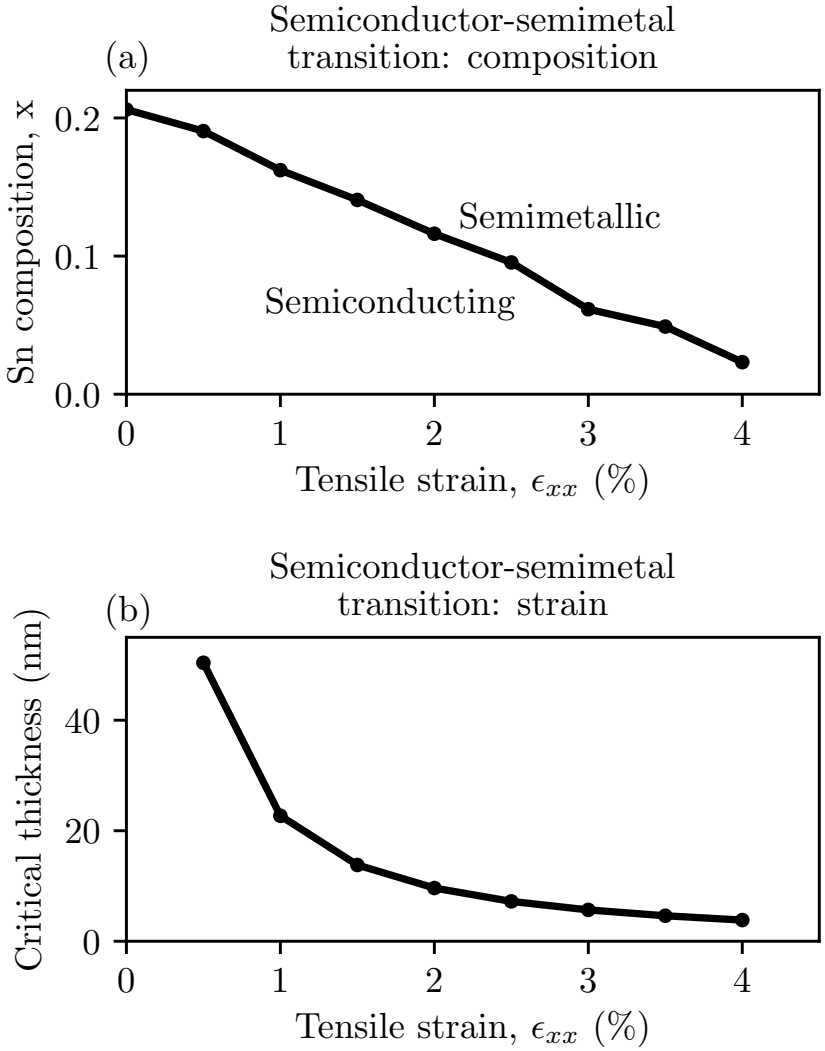

Figure 5.5: (a) Composition at which $Ge_{1-x}Sn_x$ becomes semimetallic versus tensile epitaxial strain required at this composition, and (b) critical thicknesses of these structures as a result of the epitaxial strain.

composition at which the Γ_7^- and Γ_8^+ states become degenerate at 0.5% strain intervals. Where the zero band gap did not fall on one of the compositions available from the 64 atom SQS, the composition was linearly interpolated between the two compositions either side of the semimetallic transition. While this shows the semimetal/semiconducting boundary, compositions and strains that are above this might still be suitable for semimetal electronics if a band gap can still be opened with confinement in the same manner that a band gap is predicted to open in α-Sn. Figure 5.5(b) shows the critical thickness of these structures, this

indicates that care must be taken when utilizing strains higher than 2-3% as the reduced critical thickness above these strains might limit growth to thicknesses below those at which quantum confinement opens a band gap, depending on the chosen substrate [22].

The effect of tensile strain on the valence band is also of interest here. Epitaxial strain splits the valence band in these materials, as discussed in section 2.5.2. Specifically, tensile strain shifts the light hole band upwards and the heavy hole band downwards in energy, with the reverse being true for compressive strain, as observed in fig. 3.8, where a 1% tensile strain the valence band splitting is on the order of 100 meV for both Ge and α-Sn. The light hole band exhibits a much smaller effective mass than the heavy hole band, approximately 1.5 times that of the electron effective mass, from $\mathbf{k}\cdot\mathbf{p}$ theory [35]. As such, the light hole band is shifted downwards in energy as a result of confinement at larger dimensions than the heavy hole band, from eq. (3.3). This allows for higher band gaps to be opened through quantum confinement at larger thickness. This holds true as long as the light hole band is at a higher energy level than the heavy hole band. Eventually, confinement will cause the light hole band to decrease below the energy of the heavy hole band, and the widening of the band gap as a function of thickness will abruptly slow down. This would not occur in the presence of compressive strain, as the heavy hole band is already at a higher energy than the light hole band, and as such will be affected by confinement similarly to an unstrained material. This behaviour indicates that strain is not only useful in the modulation of the band gap of the bulk material, but also influences the band gap induced through quantum confinement. As such, care must be taken when choosing strain parameters for the construction of semimetallic devices, as the rate at which the band gap opens, as a function of thickness, can differ to that of the relaxed material.

The in-plane lattice constants of the alloys presented in fig. 5.5 all lie within the range of 5.804 Å to 5.885 Å. So, to attain an alloy with the least amount of overlap between the Γ_7^- and Γ_8^+ states, substrates within this range should be experimentally investigated for growing semimetallic $Ge_{1-x}Sn_x$ structures.

InP has a low-temperature direct band gap of 1.42 eV and a lattice constant of 5.87 Å [36], lying within the range described above, making it an ideal candidate for such a substrate. A structure with a slight tensile strain could also be fabricated by growing $Ge_{1-x}Sn_x$ on a substrate of $In_yGa_{1-y}As$, an alloy already utilized as a substrate experimentally [27]. $In_yGa_{1-y}As$ has a lattice constant of 5.65 Å at y = 0 and 6.06 Å at y = 1 [37], covering the lattice parameter range required to fabricate the alloys along the semiconducting to semimetallic boundary given in fig. 5.5. This also allows the $In_yGa_{1-y}As$ alloy to match the lattice constant of $Ge_{1-x}Sn_x$ up to x = 0.5. The band gap of $In_yGa_{1-y}As$ ranges from 1.44 eV at y = 0 to 0.36 eV at y = 1, and as such it is desirable to minimize the In composition in the substrate in order to maximize the substrate band gap.

5.7 Deformation potential theory (DPT)

5.7.1 Analysis of band edge shifts with strain

To analyze the shift in the band gap brought about by strain in these cells, deformation potential theory (DPT) has been employed. The strain-dependent band gaps of pseudomorphic $Ge_{1-x}Sn_x$ alloys grown on Ge, ZnTe, and CdTe are investigated, and an analysis is performed on the combination of alloying and strain in the engineering of the semiconducting to semimetallic transition. Closed blue circles in fig. 5.6(a), fig. 5.6(b), and fig. 5.6(c) respectively show the DFT-calculated direct band gaps for pseudomorphically strained $Ge_{1-x}Sn_x$/Ge, $Ge_{1-x}Sn_x$/ZnTe, and $Ge_{1-x}Sn_x$/CdTe alloy SQSs. Results for $Ge_{1-x}Sn_x$/Ge are

shown only for x< 0.56, beyond which composition the 64-atom SQSs exceed the calculated critical thickness and become amorphous upon LDA relaxation.

These DFT calculations are compared to deformation potential theory calculations in which the hydrostatic band gap deformation potential $a_{\Gamma diff}$ is obtained via (i) linear interpolation between the values for Ge and α-Sn at each value of x (dashed red lines), or (ii) fitting to the results of the DFT calculations (solid black lines). In both cases, the VB edge axial deformation potential b for the alloy is determined by linear interpolation between the corresponding values for Ge and α-Sn (given in table 3.1). The solid black lines in fig. 5.6(a), fig. 5.6(b), and fig. 5.6(c) correspond to a best fit value $a_{\Gamma diff}$ = −5.34 eV, obtained by fitting to the DFT-calculated *inverted* direct energy gap of $Ge_{1-x}Sn_x$/ZnTe in fig. 5.6(b). It is noted that the fitting of $a_{\Gamma diff}$ is relatively insensitive to either Sn composition or choice of substrate, with similar values obtained by fitting to the DFT results for $Ge_{1-x}Sn_x$/Ge or $Ge_{1-x}Sn_x$/CdTe. It is also noted that this composition-independent best-fit value for $a_{\Gamma diff}$ produces good quantitative agreement between the full DFT and model deformation potential calculations, tending only to break down in the presence of large in-plane strains $|\epsilon_{xx}| \gtrsim 5\%$, where linear-in-strain deformation potential theory would be expected to lose accuracy, respectively at high and low x in fig. 5.6(a) and fig. 5.6(c). Here, the calculations predict (a) that the semiconducting to semimetallic transition occurs for x ≈ 0.26 in compressively strained pseudomorphic $Ge_{1-x}Sn_x$/Ge, (b) that $Ge_{1-x}Sn_x$/ZnTe is semimetallic across the full composition range, with the magnitude of the *inverted* Γ_7^--Γ_8^+ energy gap lying in the range 0.45 – 0.71 eV, and (c) that growth of $Ge_{1-x}Sn_x$ on CdTe (or, equivalently, α-Sn) increases the magnitude of the *inverted* Γ_7^--Γ_8^+ energy gap, making it more challenging to open up a band gap via quantum confinement than in α-Sn.

It is noted that the best-fit value $a_{\Gamma diff}$ = −5.34 eV for the hydrostatic deforma-

tion potential associated with the $Ge_{1-x}Sn_x$ direct band gap is not intermediate between the values of −9.54 and −6.68 eV, calculated respectively for the Γ_7^--Γ_8^+ band gaps of Ge and α-Sn (given in table 3.2). This suggests that alloy-related band mixing effects play a key role in determining the nature of the band gap in $Ge_{1-x}Sn_x$ alloys. Indeed, the best-fit value for $a_{\Gamma diff}$ is intermediate between the values associated with the direct Γ_7^--Γ_8^+ and indirect L_6^+-Γ_8^+ band gaps of Ge, reflecting that band folding in the 64-atom supercell calculations allows for hybridisation of Ge Γ- and L-point states in response to Sn incorporation. This is in agreement with recent theoretical analysis [19] suggesting that Sn incorporation in Ge drives strong hybridisation of Ge Γ- and L-point CB edge states, leading to a band gap that is neither purely indirect nor direct in nature, and which evolves continuously from indirect to direct in nature for $x \lesssim 0.1\%$ via alloy band mixing effects. This conclusion is supported by pressure-dependent measurements [38], which demonstrate that the pressure coefficient $\frac{dE_g}{dP}$ associated with the $Ge_{1-x}Sn_x$ fundamental band gap starts out equal to that of the indirect L_6^+-Γ_8^+ band gap of Ge at x = 0 (4.3 meV kbar^{-1}), and increases continuously with increasing x until it reaches a value close to that associated with the direct Γ_7^--Γ_8^+ band gap of Ge by $x \approx 0.1$ (12.9 meV kbar^{-1}). Converting the best-fit value $a_{\Gamma diff}$ = −5.34 eV to a pressure coefficient, an intermediate value $\frac{dE_g}{dP} \approx 7$ meV kbar^{-1} is obtained. It is noted that the limited band folding present in the $\lesssim 10^2$-atom supercells accessible using meta-GGA DFT calculations limits the number of states that can hybridise in response to alloying. As such, the observed Sn-induced Γ-L band mixing observed in these calculations persists across the entire composition range as an artefact of the supercells employed in the calculations [34]. Overall, our calculations then support the emerging re-evaluation of the nature of the indirect- to direct-gap transition in $Ge_{1-x}Sn_x$ alloys in terms of alloy band mixing effects [19, 38].

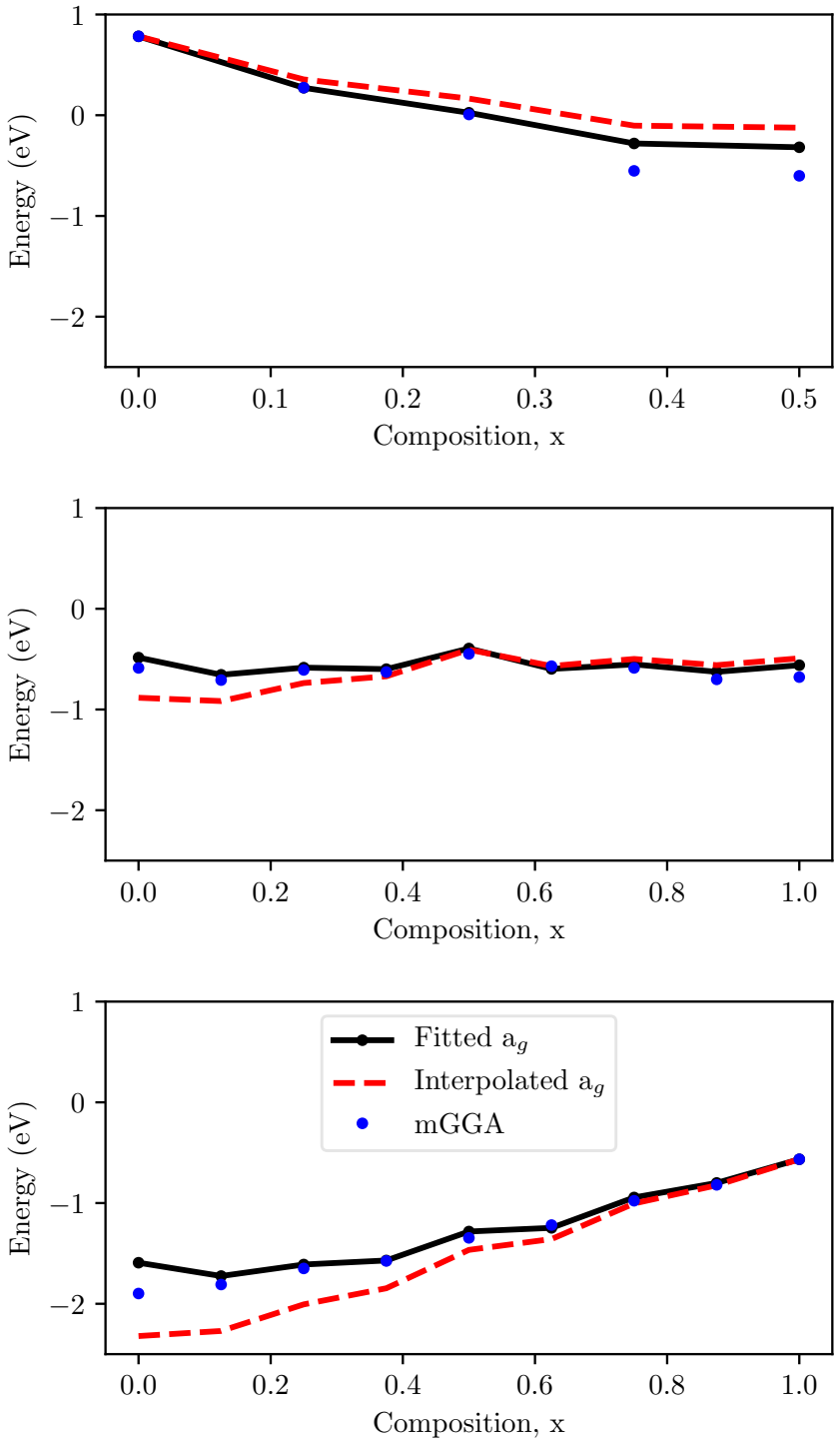

Figure 5.6: Γ_7^--Γ_8^+ energy gap as a function of Sn composition x, for pseudomorphically strained $Ge_{1-x}Sn_x$ alloy SQSs strained to (001)-oriented (a) Ge, (b) ZnTe, and (c) CdTe substrates. Closed blue circles indicate those calculated from meta-GGA DFT. Red dashed and solid black lines denote those calculated using DPT employing an interpolated value for $a_{\Gamma diff}$ and the best-fit value of −5.34 eV, respectively.

5.7.2 Predicting the alloy band gap under pseudomorphic strain

Figure 5.6 demonstrates calculated band gaps across the composition range, using the relaxed band gap energies as starting points, with DPT employed to estimate the shift due to strain. However, if an accurate continuous depiction of the relaxed band gap were obtained, then it would be possible to estimate band gaps of strained $Ge_{1-x}Sn_x$ across the full composition range without the need for DFT, thus drastically cutting computational time. To represent the relaxed band gap, the cluster expansion of the relaxed SQSs, presented in fig. 5.3, has been chosen. To calculate the band gap shift as a result of strain, DPT is employed, using the fitted value of $a_{\Gamma diff}$ = −5.34 eV. As previously stated, the limited band folding present in the 64 atom supercells limits the number of states that can hybridise in response to alloying. As such, the Sn-induced Γ-L band mixing observed in our calculations persists across the entire composition range as an artefact of the supercells employed in our calculations [34]. Therefore, the accuracy of the model can be improved through fitting of $a_{\Gamma diff}$ to larger alloy cells.

Figure 5.7 shows a comparison of the semimetal to semiconducting boundary, as calculated within this approximation and, as seen in fig. 5.5(a), obtained from DFT. The two models display very close agreement, to within less than x = 0.01, at tensile strains up to 2.5%, at which point the semiconducting to semimetallic boundary deviates by less than x = 0.025 from the DFT values. It is noted that this deviation is in large part due to the disagreement between the cluster expansion of the relaxed alloy band gap and the DFT calculated values, and as such is caused by the quasirandom nature of the cells. Beyond 2.5%, it is possible that the low critical thickness would inhibit the growth of semimetallic films, as the films would only be able to be grown to thicknesses at which quantum confinement would open a band gap, as indicated by the calculations in section 3.3.3.

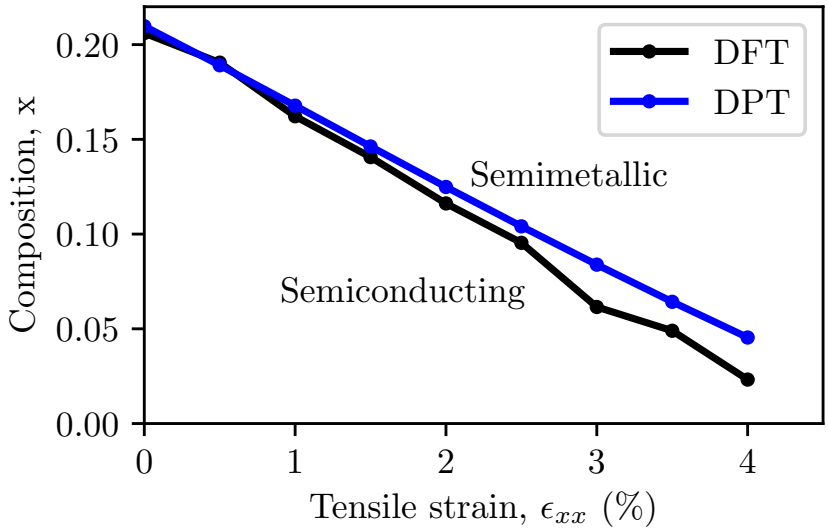

Figure 5.7: Semiconductor to semimetal transition as a function of tin composition and tensile strain, as calculated from the DFT and DPT models.

By extending this model it is possible to calculate at what strains and compositions the magnitude of the negative Γ_7^- - Γ_8^+ gap exceeds that of pure α-Sn. This allows for an estimation of the usable composition range of $Ge_{1-x}Sn_x$ for semimetal devices. The calculations represented in fig. 5.8 uses this method to calculate the band gap of the $Ge_{1-x}Sn_x$ alloy over a tensile strain and composition range. The strain magnitude is limited to 2.5% in this figure, beyond which the critical thickness is below 7 nm. The black line indicates the DFT data from fig. 5.5 (a), showing close agreement between the two methods. The green area on the plot depicts compositions at which the Γ_7^- - Γ_8^+ energy difference is less than zero and greater than that of α-tin, highlighting the most suitable choices for semimetal devices.

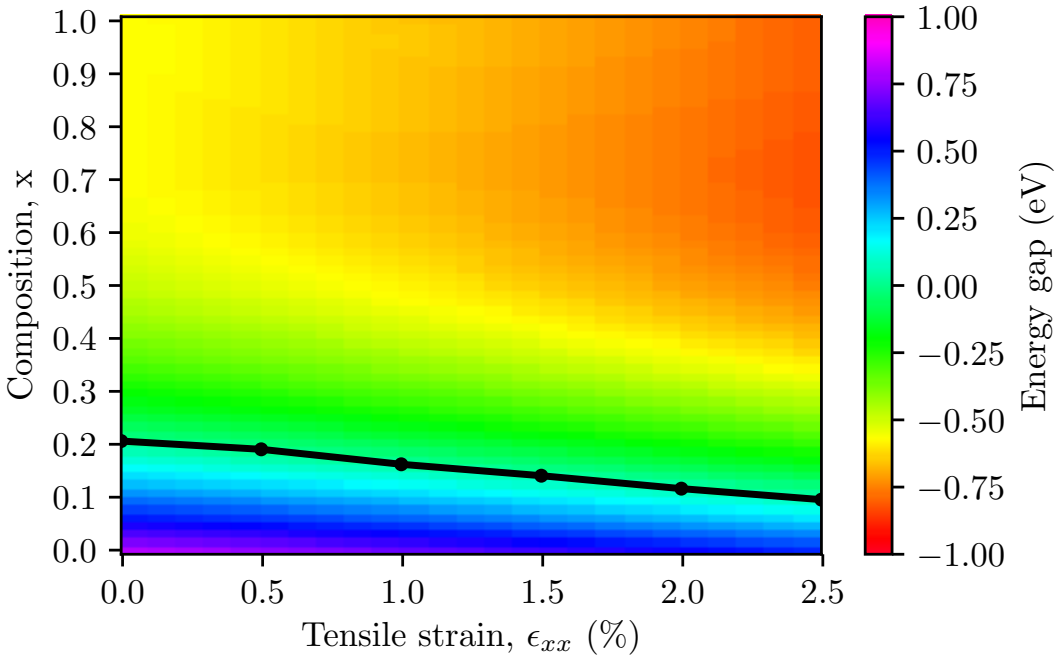

Figure 5.8: Band gap as a function of composition and tensile strain, as calculated with a mixture of deformation potential theory and the cluster expansion formalism. The black line indicates the semiconducting to semimetallic transition as calculated from the meta-GGA/DFT plus SQS method, showing good agreement between the two different approaches.

5.8 Conclusions

The band gap of the $Ge_{1-x}Sn_x$ is calculated over the full composition range using an SQS plus DFT/meta-GGA model. The calculated band gaps show good agreement with previous experimental work and indicate a crossover from semiconducting to semimetallic at $x \approx 0.21$.

These same cells are then epitaxially strained to the same substrate lattice parameters as in the previous chapter. The ZnTe substrate is shown to counteract the effects of alloying, enforcing a Γ_7^- - Γ_8^+ energy difference similar to α-Sn over the full composition range, although many of these compositions are not realistic due to the large strains imposing too small a critical thickness. The CdTe and Ge substrates are shown to offer no improvement to semiconductor-to-semimetal transition at any composition, however they clearly demonstrate the effects of

tensile and compressive strain on the band gap, respectively.

The semiconducting-to-semimetal transition is calculated from DFT as a function of strain and composition. This is compared to the critical thickness of the same compositions, showing that beyond ≈ 2.5% tensile strain the critical thickness could be too low to fabricate a semimetallic device. However, a 2% tensile strain is shown to lower the transition from x ≈ 0.21 to x ≈ 0.12. This degree of strain could be applied through growth on an $In_yGa_{1-y}As$ substrate, with the composition of the substrate tuned to a suitable lattice constant. However, $In_yGa_{1-y}As$ is shown to have a large 1.44 eV band gap at y = 0, which reduces to 0.36 eV at y = 1. As such, minimizing the amount of indium is desirable in order for there to be a suitable substrate band gap. The InP 5.87 Å lattice constant and low-temperature indirect band gap of 1.42 eV also make InP a suitable substrate to allow for the fabrication of a composition/strain combination on the semiconducting to semimetallic border.

DPT is then used to analyse the character of the Γ_7^- - Γ_8^+ energy difference. The deviations of the meta-GGA calculations away from the DPT predictions indicate clear hybridisation between the conduction band states, with the deformation potentials behaving intermediary to that of the L - Γ_8^+ and Γ_7^- - Γ_8^+ gap. Using a fitted Γ_7^- - Γ_8^+ deformation potential, DPT is combined with a cluster expansion of the relaxed Γ_7^- - Γ_8^+ energy difference over the composition range, in order to make predictions over a large range of strains and compositions. This allows for the estimation of the suitable strains and compositions which can be implemented to fabricate semimetallic $Ge_{1-x}Sn_x$ alloys.

References

[1] P. Moontragoon, Z. Ikonić, and P. Harrison. Band structure calculations of Si–Ge–Sn alloys: Achieving direct band gap materials. *Semiconductor Science and Technology*, vol. 22, no. 7, p. 742, 2007.

[2] D. W. Jenkins and J. D. Dow. Electronic properties of metastable Ge_xSn_{1-x} alloys. *Physical Review B*, vol. 36, no. 15, p. 7994, 1987.

[3] M. P. Polak, P. Scharoch, and R. Kudrawiec. The electronic band structure of $Ge_{1-x}Sn_x$ in the full composition range: indirect, direct, and inverted gaps regimes, band offsets, and the Burstein–Moss effect. *Journal of Physics D: Applied Physics*, vol. 50, no. 19, p. 195103, 2017.

[4] R. W. Olesinski and G. J. Abbaschian. The Ge-Sn (germanium-tin) system. *Bulletin of Alloy Phase Diagrams*, vol. 5, no. 3, p. 265, 1984.

[5] S. Biswas, J. Doherty, D. Saladukha, Q. Ramasse, D. Majumdar, M. Upmanyu, A. Singha, T. Ochalski, M. A. Morris, and J. D. Holmes. Non-equilibrium induction of tin in germanium: towards direct bandgap $Ge_{1-x}Sn_x$ nanowires. *Nature Communications*, vol. 7, p. 11405, 2016.

[6] A. Suzuki, O. Nakatsuka, S. Shibayama, M. Sakashita, W. Takeuchi, M. Kurosawa, and S. Zaima. Growth of ultrahigh-Sn-content $Ge_{1-x}Sn_x$ epitaxial layer and its impact on controlling Schottky barrier height of metal/Ge

contact. *Japanese Journal of Applied Physics*, vol. 55, no. 4S, p. 04EB12, 2016.

[7] J. Piao, R. Beresford, T. Licata, W. Wang, and H. Homma. Molecular-beam epitaxial growth of metastable Ge_{1-x} Sn_x alloys. *Journal of Vacuum Science & Technology B: Microelectronics Processing and Phenomena*, vol. 8, no. 2, p. 221, 1990.

[8] G. He and H. A. Atwater. Synthesis of epitaxial Sn_xGe_{1-x} alloy films by ion-assisted molecular beam epitaxy. *Applied Physics Letters*, vol. 68, no. 5, p. 664, 1996.

[9] S. Gupta, B. Magyari-Köpe, Y. Nishi, and K. C. Saraswat. Achieving direct band gap in germanium through integration of Sn alloying and external strain. *Journal of Applied Physics*, vol. 113, no. 7, p. 073707, 2013.

[10] M. Virgilio, C. Manganelli, G. Grosso, G. Pizzi, and G. Capellini. Radiative recombination and optical gain spectra in biaxially strained n-type germanium. *Physical Review B*, vol. 87, no. 23, p. 235313, 2013.

[11] M. El Kurdi, G. Fishman, S. Sauvage, and P. Boucaud. Band structure and optical gain of tensile-strained germanium based on a 30 band k· p formalism. *Journal of Applied Physics*, vol. 107, no. 1, p. 013710, 2010.

[12] C. O'Donnell, A. Sanchez-Soares, C. A. Broderick, and J. C. Greer. Impact of stoichiometry and strain on $Ge_{1-x}Sn_x$ alloys from first principles calculations. *Journal of Physics D: Applied Physics*, vol. 54, no. 24, p. 245103, 2021.

[13] J. P. Perdew and A. Zunger. Self-interaction correction to density-functional approximations for many-electron systems. *Physical Review B*, vol. 23, no. 10, p. 5048, 1981.

[14] F. Tran and P. Blaha. Accurate band gaps of semiconductors and insulators with a semilocal exchange-correlation potential. *Physical Review Letters*,

vol. 102, no. 22, p. 226401, 2009.

[15] A. Sanchez-Soares, C. O'Donnell, and J. C. Greer, "Epitaxial stabilisation of $Ge_{1-x}Sn_x$ alloys." Unpublished.

[16] C. G. Van de Walle. Band lineups and deformation potentials in the model-solid theory. *Physical Review B*, vol. 39, no. 3, p. 1871, 1989.

[17] M. P. C. M. Krijn. Heterojunction band offsets and effective masses in III-V quaternary alloys. *Semiconductor Science and Technology*, vol. 6, no. 1, p. 27, 1991.

[18] M. Usman, C. A. Broderick, Z. Batool, K. Hild, T. J. C. Hosea, S. J. Sweeney, and E. P. O'Reilly. Impact of alloy disorder on the band structure of compressively strained $GaBi_xAs_{1-x}$. *Phys. Rev. B*, vol. 87, p. 115104, 2013.

[19] E. J. O'Halloran, C. A. Broderick, D. S. P. Tanner, S. Schulz, and E. P. O'Reilly. Comparison of first principles and semi-empirical models of the structural and electronic properties of $Ge_{1-x}Sn_x$ alloys. *Optical and Quantum Electronics*, vol. 51, p. 314, 2019.

[20] C. Eckhardt, K. Hummer, and G. Kresse. Indirect-to-direct gap transition in strained and unstrained Sn_xGe_{1-x} alloys. *Phys. Rev. B*, vol. 89, p. 165201, 2014.

[21] L. Ansari, G. Fagas, J.-P. Colinge, and J. C. Greer. A proposed confinement modulated gap nanowire transistor based on a metal (tin). *Nano Letters*, vol. 12, no. 5, p. 2222, 2012.

[22] A. Sanchez-Soares, C. O'Donnell, and J. C. Greer. Electronic structure tuning via surface modification in semimetallic nanowires. *Physical Review B*, vol. 94, no. 23, p. 235442, 2016.

[23] A. Sanchez-Soares and J. C. Greer. A semimetal nanowire rectifier: Balancing quantum confinement and surface electronegativity. *Nano Letters*, vol. 16, no. 12, p. 7639, 2016.

[24] S. Küfner, J. Furthmüller, L. Matthes, M. Fitzner, and F. Bechstedt. Structural and electronic properties of α-tin nanocrystals from first principles. *Physical Review B*, vol. 87, no. 23, p. 235307, 2013.

[25] H.-S. Lan, S. Chang, and C. Liu. Semiconductor, topological semimetal, indirect semimetal, and topological Dirac semimetal phases of $Ge_{1-x}Sn_x$ alloys. *Physical Review B*, vol. 95, no. 20, p. 201201, 2017.

[26] J. M. Sanchez, F. Ducastelle, and D. Gratias. Generalized cluster description of multicomponent systems. *Physica A. Statistical and Theoretical Physics*, vol. 128, no. 1-2, p. 334, 1984.

[27] H. Lin, R. Chen, W. Lu, Y. Huo, T. I. Kamins, and J. S. Harris. Investigation of the direct band gaps in $Ge_{1-x}Sn_x$ alloys with strain control by photoreflectance spectroscopy. *Applied Physics Letters*, vol. 100, no. 10, p. 102109, 2012.

[28] H. Tran, W. Du, S. A. Ghetmiri, A. Mosleh, G. Sun, R. A. Soref, J. Margetis, J. Tolle, B. Li, H. A. Naseem, and S.-Q. Yu. Systematic study of $Ge_{1-x}Sn_x$ absorption coefficient and refractive index for the device applications of Si-based optoelectronics. *Journal of Applied Physics*, vol. 119, p. 103106, 2016.

[29] C. Xu, P. M. Wallace, D. A. Ringwala, S. L. Y. Chang, C. D. Poweleit, J. Kouvetakis, and J. Menéndez. Mid-infrared (3-8 µm) $Ge_{1-y}Sn_y$ alloys ($0.15 < y < 0.30$): synthesis, structural, and optical properties. *Applied Physics Letters*, vol. 114, no. 21, p. 212104, 2019.

[30] B. L. Booth and A. W. Ewald. Nonparabolicity of the gray-tin $\Gamma_8{}^+$ conduction band. *Physical Review*, vol. 168, p. 796, 1968.

[31] P. M. Pearce, *Novel materials and device architectures for high-efficiency solar cells*. PhD thesis, Department of Physics, Imperial College London, 2021.

[32] B. Cao, S. Chen, X. Jin, J. Liu, and T. Li. Short-range order in GeSn alloy. *ACS Applied Materials & Interfaces*, vol. 12, no. 51, pp. 57245–57253, 2020.

[33] S. Assali, A. Dijkstra, A. Attiaoui, É. Bouthillier, J. Haverkort, and O. Moutanabbir. Midinfrared emission and absorption in strained and relaxed direct-band-gap $Ge_{1-x}Sn_x$ semiconductors. *Phys. Rev. Applied*, vol. 15, p. 024031, 2021.

[34] C. A. Broderick, E. J. O'Halloran, and E. P. O'Reilly, "First principles analysis of electronic structure evolution and the indirect- to direct-gap transition in $Ge_{1-x}Pb_x$ group-IV alloys." Unpublished, 2019.

[35] E. O'Reilly, *Quantum Theory of Solids*. London: Taylor & Francis, 2002.

[36] I. Vurgaftman, J. R. Meyer, and L. R. Ram-Mohan. Band parameters for III–V compound semiconductors and their alloys. *Journal of Applied Physics*, vol. 89, no. 11, p. 5815, 2001.

[37] W. M. Haynes, *CRC Handbook of Chemistry and Physics, 95th Edition*. Boca Raton: CRC Press, 2014.

[38] T. D. Eales, I. P. Marko, S. Schulz, *et al.* $Ge_{1-x}Sn_x$ alloys: Consequences of band mixing effects for the evolution of the band gap γ-character with Sn concentration. *Scientific Reports*, vol. 9, no. 1, p. 1, 2019.

Chapter 6

Conclusion

6.1 Conclusion

In this thesis the miscibility and structural properties of $Ge_{1-x}Sn_x$ alloys have been investigated across the composition range. The evolution of the electronic band structure of $Ge_{1-x}Sn_x$ alloys as a result of alloy stoichiometry and strain has also been explored. Both of these tasks were undertaken with the aim of finding the ideal conditions for the fabrication of semimetallic $Ge_{1-x}Sn_x$ alloys, with a view to use these in confinement modulated devices.

Chapter 3 is concerned with characteristics of the two alloy components, germanium (Ge) and α-tin (α-Sn). Density functional theory (DFT) was employed to predict structural and electronic properties, such as the elastic constants, lattice constants, and electronic band gaps, in order to provide baseline results for alloy calculations in later chapters, as well as for use in models applied to the materials in order to investigate their behaviour under strain. The calculated elastic constants were used to estimate the critical thicknesses of the two materials, showing how even small values of strain drastically reduced the maximum growth thickness. Although electronic band gaps and deformation potentials showed good

agreement with experimental results, the effective masses of α-Sn did not agree with the literature [1], likely due to the complicated nature of the band structure of the material which displays an *inverted* band gap, with the Γ_7^- state lower in energy than the Γ_8^+ states, causing the light electron (LE) band to change direction of curvature [2–4]. As such, in order to calculate which bulk bands correspond to the confined bands in a thin film, the band structure of a single α-Sn thin film was calculated and band character was analyzed. The results showed that the Γ_7^- is pushed above the conduction band when confined, in agreement with a prevous study [5] indicating that this is a key state to observe when calculating alloy band structures. The behaviour of the electronic states was studied under applied strain, within both DFT and deformation potential theory (DPT), which were shown to agree with each other as well as with experimental results. The plane perpendicular to the <100> direction was chosen as the plane to epitaxially strain the alloy in as it is shown to exhibit the greatest capacity for strain relaxation. It was predicted that the amount of strain required to induce a semimetallic transition in germanium was too high to allow for a critical thickness above the minimum confinement thickness. This implies that pure germanium would not be a suitable material for semimetal based devices, even with the addition of tensile strain. In α-Sn, tensile strain is shown to lower the Γ_8^+ state relative to the Γ_7^- states, indicating that strain could be used to gain additional control over the band gap in confined structures. This has been previously demonstrated in Sn nanowires [6].

In chapter 4 the structural properties and miscibility of the alloys were analysed. First the evolution of the structural properties of materials, such as lattice constant, elastic constant, and the bond lengths present within the simulation cells, were analysed. The low lattice constant bowing parameter was shown to agree with the results from previous studies. Though there is some disagreement in the literature as the to bowing parameters of the elastic constants, those calculated

in this work are shown to exhibit non-negligible bowing over the composition range. The bond length data presented in this work is shown to agree with both previous theory and experiment for low Sn content alloys, while also predicting how the bond lengths change across compositions not yet present in the literature. Two miscibility models were compared with results from DFT: the Bragg-Williams (BW) model and the cluster expansion (CE) formalism. Although both models predicted immiscibility of the alloy components at 0 K, the BW model underestimated the formation energy. Through comparison to various differently parametrised CEs, this was brought about by the simplistic method employed in this work to calculate the interactions energies of the BW model. The BW model was shown to be unable to predict asymmetry in the calculated formation energy curve. This effect can be captured by the CE through the inclusion of triplet interactions. The asymmetry points towards Sn rich alloys being easier to attain than Ge rich alloys. When formation energies calculated from DFT are analysed, they indicate that the largest contributing factor to immiscibility is the volume deformation term.

The alloys were then studied under epitaxial strain. The critical thicknesses of the alloy under strain indicated similar results to those of the pure alloy components, presented in chapter 3, with a slight increase in critical thickness for the Sn rich alloys. As well as this, the results of the miscibility models indicated that lattice matching the relaxed alloy to the substrate lattice constant is energetically preferable relative to a relaxed decomposition. While the assumption of coherent segregation showed that a substrate with an intermediate lattice constant would aid miscibility, this would also drastically reduce the critical thickness of such a strained film. As such, it is evident that in order to grow semimetallic films to the required thickness so that confinement does not open a gap, strain should be kept to a minimum in order to ensure a high critical thickness and to maximize miscibility.

In chapter 5 the bulk alloy band gaps are studied and the crossover from semiconducting to semimetallic behaviour was shown to be x≈0.2. These cells were strained to the same lattice parameter as in the previous section and the band gap behaviour was shown to be similar to the pure alloy components: compressive strain had a negligible effect on the energy separation, while tensile strain decreased the Γ_8^+ state relative to the Γ_7^- state. This indicates that germanium offers no benefit as a substrate for growth of semimetallic alloy films, a CdTe substrate increases the magnitude of the *negative* band gap, and a ZnTe substrate offsets the effect of alloying, with a consistent negative band gap value similar to α-Sn. The semiconductor to semimetallic boundary was calculated in DFT as a function of both composition and strain. This would be achievable through a substrate with a variable lattice parameter, such as $In_yGa_{1-y}As$. $In_yGa_{1-y}As$ has a lattice constant of 5.65 Å at y = 0 and 6.06 Å at y = 1 [7], indicating that it would be capable of lattice matching $Ge_{1-x}Sn_x$ up to compositions of x≈ 0.5, and would be able to apply tensile strain on compositions below this. However, the band gap of $In_yGa_{1-y}As$ ranges from 1.44 eV at y = 0 to 0.36 eV at y = 1 [7], and as such the In composition of the $In_yGa_{1-y}As$ should be kept to a minimum in order to maximize the substrate band gap. The band characteristics of $Ge_{1-x}Sn_x$ alloys were studied using deformation potential theory in a similar manner as in chapter 3. Fitting the DPT calculations to DFT results shows a band gap deformation potential consistent with that of a hybrid L and Γ band gap, agreeing with a previous study [8]. Through combination of deformation potential theory and the cluster expansion, a model was developed which accurately reproduced the 64 atom SQS data. This was then used to efficiently estimate which alloy compositions exhibit a favourable Γ_8^+ - Γ_7^- energy difference. Although some of the alloy compositions would be difficult to achieve due to growth limitations as a result of strain and immiscibility.

As an overview, it is evident that unstrained $Ge_{1-x}Sn_x$ alloys exhibit suitable

electronic structures for use in semimetal based devices at compositions of x>0.2. The addition of Ge to lattice matched α-Sn has been previously shown experimentally to increase temperature of the transition to β-Sn [9], and the band gap calculations in this work indicates that this does not impact the semimetallic nature of the band structure, suggesting high Sn content alloys would be suitable for the fabrication of semimetallic $Ge_{1-x}Sn_x$, if the temperature of the transition to β-Sn is increased sufficiently by the addition of Ge. Lattice matching the substrate of these alloys would allow for the greatest miscibility as well as critical thickness.

With regards to the use of strain as a means for creating semimetallic $Ge_{1-x}Sn_x$, compressive strain was shown to provide little benefit to modifying electronic structure while decreasing the critical thickness of both the pure alloy components as well as the $Ge_{1-x}Sn_x$ alloys themselves. Compressive strain was also shown to negatively impact the miscibility of these systems and, as such, should not be considered when creating semimetallic $Ge_{1-x}Sn_x$ structures. Tensile strain however, is shown to lower the Sn content required for the alloy to transition to semimetal, thus assisting with the suppression of Ge and Sn segregation, as compositions farther from the x=0.5 composition have lower formation energies. However, this is at the cost of a decreasing critical thickness, and as such strains should be minimized in order to ensure that alloy thicknesses can be achieved beyond which quantum confinement opens a band gap.

6.2 Outlook and further work

The continuation of this work would be based on nanostructure calculations, such as thin films or nanowires.

The alloy nature of these structures adds a large computational cost to the calcu-

lations, requiring either large quantities of compute power or time. The structures themselves can easily be obtained by cleaving them from larger bulk SQS cells, if randomness is assumed, however an average over a number of structures at each composition would be required to remove any band structure discrepancies created by the effects of randomness on the surface of the film. As an extreme example: if cleaving the film created a structure where the surface lattice sites were fully occupied by germanium, the band structure would not be indicative of a random alloy. However, it is possible that depending on the surface termination used, the structures may energetically prefer one atomic species over the other at the surface. As such three main questions are brought up when studying nanostructures comprised of $Ge_{1-x}Sn_x$ alloys. First there is the question of which terminating species would be suitable. Total energy calculations could be used to predict which surface terminations would be stable on the $Ge_{1-x}Sn_x$ alloy, relative to dissociation. Secondly, there is the question of how the presence of a surface, as well as a surface termination, modifies the thermodynamics of the alloy. Monte Carlo calculations, as described in Cao et al. [10] can be used to measure the effect of these on the alloy correlation functions. This would then reveal any ordering or segregation presenting in the nanostructures. Finally the impact of nanowire orientation should be considered, as this has a large effect on the surface area of the wire. As such, certain orientations would magnify the surface effects on the thermodynamics of the alloy.

As well as taking the structural and thermodynamic details into consideration, the metaGGA/DFT parameters must also be considered. The TB-mBJ exchange-correlation potential applied in our analysis of bulk-like $Ge_{1-x}Sn_x$ supercells is not applicable in thin film calculations, as the potential becomes singular in the presence of vanishing charge density. [11]. As such, a new method for overcoming the underestimation of the band gap would need to be found. One possibility is the GW approximation. However, requiring multiple calculations of alloy supercells

would be highly computationally demanding within the GW approximation.

By varying the surface termination on nanostructures, the band gap of these materials can be further modified in order to create desirable band profiles for use in semimetal based device designs, as was shown to be the case for α-Sn nanowires [12]. This warrants investigation in $Ge_{1-x}Sn_x$ alloys, as it would add yet another variable parameter for the control of their electronic structure. Allowing for control over the band gap through alloy composition, strain, thickness, and finally surface termination.

Once nanostructures with appropriate electronic structures are identified, the next step would involve device calculations, such as transport calculations, giving insight into the performance of a $Ge_{1-x}Sn_x$ alloy based semimetal device.

References

[1] O. Madelung and U. Rössler, *Group IV Elements, IV-IV and III-V Compounds. Part b - Electronic, Transport, Optical and Other Properties.* Heidelberg: Springer, 2002.

[2] H. Warlimont and W. Martienssen, *Springer Handbook of Condensed Matter and Materials Data.* Heidelberg: Spinger, 2005.

[3] D. Sherrington and W. Kohn. Speculations about grey tin. *Reviews of Modern Physics*, vol. 40, p. 767, 1968.

[4] S. Groves, C. Pidgeon, A. Ewald, and R. Wagner. Interband magnetoreflection of α-Sn. *Journal of Physics and Chemistry of Solids*, vol. 31, no. 9, p. 2031, 1970.

[5] S. Küfner, J. Furthmüller, L. Matthes, M. Fitzner, and F. Bechstedt. Structural and electronic properties of α-tin nanocrystals from first principles. *Physical Review B*, vol. 87, no. 23, p. 235307, 2013.

[6] L. Ansari, G. Fagas, and J. C. Greer. Strain induced effects on electronic structure of semi-metallic and semiconducting tin nanowires. *Applied Physics Letters*, vol. 105, p. 123105, 2014.

[7] W. M. Haynes, *CRC Handbook of Chemistry and Physics, 95th Edition.* Boca Raton: CRC Press, 2014.

[8] C. A. Broderick, M. D. Dunne, D. S. Tanner, A. C. Kirwanv, E. J. O'Halloran, S. Schulz, and E. P. O'Reilly, Atomistic analysis of localisation and band mixing effects in $Ge_{1-x}(C, Sn)_x$ group-IV alloys. in *2018 IEEE 18th International Conference on Nanotechnology (IEEE-NANO)*, p. 1, IEEE, 2018.

[9] R. Farrow, D. Robertson, G. Williams, A. Cullis, G. Jones, I. Young, and P. Dennis. The growth of metastable, heteroepitaxial films of α-Sn by metal beam epitaxy. *Journal of Crystal Growth*, vol. 54, no. 3, p. 507, 1981.

[10] B. Cao, S. Chen, X. Jin, J. Liu, and T. Li. Short-range order in GeSn alloy. *ACS Applied Materials & Interfaces*, vol. 12, no. 51, pp. 57245–57253, 2020.

[11] F. Tran and P. Blaha. Accurate band gaps of semiconductors and insulators with a semilocal exchange-correlation potential. *Physical Review Letters*, vol. 102, no. 22, p. 226401, 2009.

[12] A. Sanchez-Soares, C. O'Donnell, and J. C. Greer. Electronic structure tuning via surface modification in semimetallic nanowires. *Physical Review B*, vol. 94, no. 23, p. 235442, 2016.